

Aus dem Institut für Schlaganfall- und Demenzforschung,
Institut der Ludwig-Maximilians-Universität München
Vorstand: Prof. Dr. Martin Dichgans

**ANALYSIS OF THE BRAIN VASCULATURE
IN A NOVEL MOUSE MODEL OF HTRA1-RELATED
CEREBRAL SMALL VESSEL DISEASE**

Dissertation
zum Erwerb des Doktorgrades der Medizin
an der Medizinischen Fakultät der
Ludwig-Maximilians-Universität zu München

vorgelegt von
Ameli Elisabeth Gerhard
aus
München
2022

Mit Genehmigung der Medizinischen Fakultät
der Universität München

Berichterstatter:	Prof. Dr. Martin Dichgans
Mitberichterstatter:	Prof. Dr. Christian Opherk
	Prof. Dr. Roman Haberl
Mitbetreuung durch die promovierte Mitarbeiterin:	Dr. Nathalie Beaufort
Dekan:	Prof. Dr. med. Thomas Gudermann
Tag der mündlichen Prüfung:	29.09.2022

TABLE OF CONTENTS

LIST OF FIGURES	VI
LIST OF TABLES.....	VII
LIST OF ABBREVIATIONS	VIII
ZUSAMMENFASSUNG.....	1
ABSTRACT	3
1 INTRODUCTION	5
1.1 Cerebral small vessel disease (cSVD).....	5
1.2 HTRA1: an emerging player in cSVD	8
1.2.1 Pathogenic <i>HTRA1</i> mutations are causative for familial cSVD	8
1.2.1.1 Identification of <i>HTRA1</i> as a causative gene for familial cSVD	8
1.2.1.2 Clinical features of HTRA1-related familial cSVD.....	9
1.2.1.3 Radiological findings in HTRA1-related familial cSVD.....	11
1.2.1.4 Histopathological findings in HTRA1-related familial cSVD	11
1.2.2 Deregulation of HTRA1 in other cerebrovascular disorders	12
1.3 Molecular mechanisms underlying the pathogenicity of HTRA1 mutations	13
1.3.1 HTRA1 is expressed in the cerebrovasculature	13
1.3.2 Pathogenic HTRA1 mutations disrupt the protease activity of HTRA1.....	13
1.3.3 HTRA1 loss of function leads to an accumulation of secreted and matrisomal HTRA1 substrates	14
1.3.4 A subset of pathogenic mutations impairs the multimeric assembly of HTRA1.....	15
1.3.5 The rational correction of HTRA1 multimeric assembly defects restores HTRA1 protease activity.....	16
1.3.6 Mutations that interfere with the multimeric assembly of HTRA1 might display dominant-negative properties	16
2 AIMS OF THE PROJECT.....	18
3 MATERIALS AND METHODS	19
3.1 Mice.....	19
3.1.1 Mouse strains	19
3.1.1.1 <i>Htra1</i> ^{R274Q} strain.....	19
3.1.1.2 <i>Htra1</i> ^{ko} strain.....	19
3.1.2 Genotyping	20
3.1.2.1 <i>Htra1</i> ^{R274Q} mice	20
3.1.2.2 <i>Htra1</i> ^{ko} mice.....	21
3.1.3 Viral infection	22
3.1.4 Mouse sacrifice, organ and vessel retrieval.....	22
3.1.4.1 Sacrifice and perfusion	22
3.1.4.2 Brain harvest.....	23
3.1.4.3 Dissection of cerebral vessels	23

3.2	Tissue preparation	23
3.2.1	Isolation of cerebral vessels	23
3.2.2	Tissue lysis for protein analysis	24
3.2.2.1	RIPA lysis	24
3.2.2.2	SDT lysis.....	24
3.2.2.3	Protein concentration measurement.....	24
3.2.3	Tissue lysis for mRNA analysis and mRNA isolation.....	25
3.3	Western blot (WB)	25
3.3.1	Sodium dodecyl sulfate polyacrylamide gel electrophoresis (SDS-PAGE)	25
3.3.2	Transfer and Coomassie staining	27
3.3.3	Immunoblot.....	27
3.4	Mass spectrometry (MS) analysis	28
3.5	Reverse transcription quantitative real-time PCR (RT-qPCR)	29
3.5.1	cDNA synthesis	29
3.5.2	Quantitative real-time PCR (qPCR).....	29
3.5.3	Data analysis	30
3.6	Histology and immunohistochemistry	30
3.6.1	Isolated vessels	30
3.6.2	Paraffin sections	31
3.6.2.1	Paraffin embedding and sectioning	31
3.6.2.2	Deparaffinization.....	32
3.6.2.3	Antigen retrieval and IHC stainings	32
3.6.3	Free-floating sections	33
3.7	Microscopy and signal quantification	33
3.7.1	Fluorescence microscopy.....	33
3.7.2	Confocal laser scanning microscopy	33
3.8	Statistics	33
4	RESULTS	34
4.1	Molecular phenotype of <i>Htra1</i>^{R274Q} brain vessels	34
4.1.1	Fibronectin is upregulated in <i>Htra1</i> ^{R274Q} brain vessels	34
4.1.2	<i>Htra1</i> ^{R274Q} brain vessels exhibit reduced HTRA1 protein levels along with an upregulation of ECM proteins	37
4.1.2.1	Validation of a mouse brain vessel isolation procedure.....	37
4.1.2.2	MS analysis of <i>Htra1</i> ^{wt} and <i>Htra1</i> ^{R274Q} brain vessels.....	39
4.1.2.3	Validation of LTBP4 upregulation via IB and IHC analysis	41
4.2	Functional correction of HTRA1-R274Q <i>in vivo</i> using an AAV-based approach	44
4.2.1	Experimental design of the rescue assay	44
4.2.2	AAV-HTRA1 is expressed in mouse brain vessels 5 months post-infection.....	45
4.2.3	Infection with AAV-HTRA1-D174R-S328A does not alleviate FN and LTBP4 accumulation in leptomenigeal arteries of <i>Htra1</i> ^{R274Q} mice.....	46
4.2.4	BR1-AAV2 efficiently infects parenchymal but not leptomenigeal brain vessels.....	47
4.2.5	Infection with AAV-HTRA1-D174R-S328A does not alleviate proteome alterations in <i>Htra1</i> ^{R274Q} brain vessels	47
4.3	Proteome changes in <i>Htra1</i>^{R274Q} vessels are mostly restricted to leptomenigeal brain vessels	50

4.3.1	Development of a protocol for anatomically defined and size-dependent fractionation of the brain vasculature.....	50
4.3.2	LTBP4, FN, FBLN5, and EGFL8 are predominantly expressed in the leptomeningeal vasculature — their site of accumulation in <i>Htra1</i> ^{R274Q} brain vessels.....	51
4.4	Mutation R274Q does not exert obvious dominant-negative effects in the mouse brain vasculature	53
5	DISCUSSION	55
5.1	Cerebrovascular consequences of HTRA1 mutation R274Q	55
5.2	Aberrant ECM in <i>Htra1</i>^{R274Q} mouse brain vessels.....	56
5.3	AAV-mediated expression of a protein-based HTRA1 corrector in the brain vasculature.....	58
5.4	Putative dominant-negative properties of mutation R274Q	60
	COPYRIGHT DECLARATION	XI
	BIBLIOGRAPHY	XII
	DANKSAGUNG/ACKNOWLEDGEMENTS	XVIII
	AFFIDAVIT	XIX
	CONGRUENCY DECLARATION.....	XX
	LIST OF PUBLICATIONS	XXI

LIST OF FIGURES

Figure 1.1	Brain vessel architecture and composition of arteries, arterioles, and capillaries	5
Figure 1.2	Radiological and histopathological features of sporadic cSVD	7
Figure 1.3	Radiological, clinical, and histopathological findings in HTRA1-related cSVD	10
Figure 1.4	Vascular accumulation of HTRA1 in other brain vessel diseases.....	12
Figure 1.5	HTRA1 expression among various cerebrovascular cell types.....	13
Figure 1.6	Mutations identified in HTRA1-related cSVD	14
Figure 1.7	The disease-causing mutation R274Q affects HTRA1 trimer interface	15
Figure 1.8	Functional correction of R274Q by the complementary mutation D174R.....	16
Figure 3.1	Sequence and restriction profile of <i>Htra1^{wt}</i> and <i>Htra1^{R274Q}</i> alleles	21
Figure 3.2	Genomic structure and genotyping of <i>Htra1^{wt}</i> and <i>Htra1^{ko}</i> alleles	22
Figure 4.1	Fibronectin is predominantly expressed in leptomeningeal arteries and arterioles	35
Figure 4.2	Fibronectin is upregulated in leptomeningeal arteries and arterioles of 6-month-old <i>Htra1^{R274Q}</i> mice	36
Figure 4.3	The age-dependent reduction of FN expression is impaired in <i>Htra1^{R274Q}</i> leptomeningeal vessels.....	37
Figure 4.4	Validation of a mouse brain vessel isolation protocol	38
Figure 4.5	Overview of the proteomic analysis of <i>Htra1^{wt}</i> and <i>Htra1^{R274Q}</i> brain vessels	40
Figure 4.6	Mutation R274Q leads to a distinct reduction of HTRA1 protein levels while leaving mRNA levels unchanged.....	40
Figure 4.7	Secreted and ECM proteins accumulate in <i>Htra1^{R274Q}</i> brain vessels	41
Figure 4.8	IB analysis confirms LTBP4 accumulation in <i>Htra1^{R274Q}</i> brain vessels.....	42
Figure 4.9	LTBP4 is upregulated in leptomeningeal arteries and arterioles of <i>Htra1^{R274Q}</i> mice	43
Figure 4.10	Experimental design of the rescue assay	44
Figure 4.11	AAV-HTRA1 is expressed in the brain vasculature of <i>Htra1^{R274Q}</i> animals 5 months post-infection.....	45
Figure 4.12	AAV-HTRA1-D174R-S328A does not alter the enrichment of FN and LTBP4 in leptomeningeal arteries of <i>Htra1^{R274Q}</i> mice	46
Figure 4.13	AAV-eGFP is efficiently expressed in parenchymal but not leptomeningeal vessels.....	47
Figure 4.14	Selection of samples exhibiting high AAV-HTRA1-V5 expression levels	48
Figure 4.15	AAV-HTRA1-D174R-S328A does not alleviate the accumulation of ECM proteins in <i>Htra1^{R274Q}</i> brain vessels	49
Figure 4.16	Anatomically defined and size-dependent fractionation of the brain vasculature.....	51
Figure 4.17	The ECM proteins upregulated in <i>Htra1^{R274Q}</i> vessels are predominantly expressed in leptomeningeal vessels	52

Figure 4.18	Comparison of FN and LTBP4 accumulation in the leptomenigeal vasculature of <i>Htra1</i> ^{R274Q} and <i>Htra1</i> ^{ko} mice does not reveal dominant-negative effects of mutation R274Q.....	54
Figure 5.1	Proteins upregulated in <i>Htra1</i> ^{R274Q} vessels are involved in elastogenesis.....	58
Figure 5.2	Genetic delivery of a protein-based HTRA1 corrector	60

LIST OF TABLES

Table 3.1	PCR mix used for genotyping	20
Table 3.2	Cycling conditions used for genotyping	20
Table 3.3	Lysis buffers used for protein analysis.....	25
Table 3.4	Composition of gel solutions and buffers used for protein analysis	26
Table 3.5	Primary antibodies used for WB	27
Table 3.6	HRP-coupled antibodies used for WB	28
Table 3.7	Sequences of the primers used for qPCR	29
Table 3.8	Cycling conditions used for qPCR	30
Table 3.9	Primary antibodies used for IHC	31
Table 3.10	Secondary antibodies used for IHC	31
Table 3.11	Running cycle used for paraffin embedding.....	32
Table 3.12	Solutions used for deparaffinization.....	32

LIST OF ABBREVIATIONS

Amino acids are abbreviated following the international one or three letter code and are not listed here.

4-BPA	4-Phenyl butyric acid
aa	Amino acids
AAV	Adeno-associated virus
Ab	Antibody
APS	Ammonium persulfate
AQP4	Aquaporin 4
AU	Arbitrary units
BBB	Blood-brain barrier
BCA	Bichinonic acid
bp	Base pairs
BSA	Bovine serum albumin
CAA	Cerebral amyloid angiopathy
CADASIL	Cerebral autosomal dominant arteriopathy with subcortical infarcts and leukoencephalopathy
CARASIL	Cerebral autosomal recessive arteriopathy with subcortical infarcts and leukoencephalopathy
Cas9	CRISPR associated protein 9
cDNA	Complementary DNA
Col IV	Type IV collagen
COL4A1	Type IV collagen, α 1 chain (protein)
COL4A1	Type IV collagen, α 1 chain (gene)
COL4A2	Type IV collagen, α 2 chain (protein)
COL4A2	Type IV collagen, α 2 chain (gene)
CRISPR	Clustered regularly interspaced short palindromic repeats
cSVD	Cerebral small vessel disease
DAPI	4',6-Diamidino-2-phenylindole
DTT	Dithiothreitol
DWI	Diffusion-weighted imaging (MRI sequence)
DZNE	German Center for Neurodegenerative Diseases/ Deutsches Zentrum für Neurodegenerative Erkrankungen
ECM	Extracellular matrix
EGFL8	Epidermal growth factor-like protein 8
FBLN5	Fibulin 5
FDR	False discovery rate
FLAIR	Fluid-attenuated inversion recovery (MRI sequence)

FN	Fibronectin
GOM	Granular osmiophilic material
GWAS	Genome-wide association study
H&E	Haematoxylin and eosin stain
HRP	Horseshoe peroxidase
HTRA1	High-temperature requirement serine peptidase A1 (protein)
<i>Htra1</i>	High-temperature requirement serine peptidase A1 (gene, mouse)
<i>HTRA1</i>	High-temperature requirement serine peptidase A1 (gene, human)
IB	Immunoblot
IHC	Immunohistochemistry
ISD	Institute for Stroke and Dementia Research/ Institut für Schlaganfall- und Demenzforschung
ko	Knockout
Lam	Laminin
LC-MS/MS	Liquid chromatography with tandem mass spectrometry
LFQ	Label-free quantification
LOX	Lysyl oxidase
LTBP1	Latent TGF- β binding protein 1
LTBP4	Latent TGF- β binding protein 4 (protein)
<i>Ltbp4</i>	Latent TGF- β binding protein 4 (gene, mouse)
MAP2	Microtubule-associated protein 2
MEM	Minimal Essential Media
MRI	Magnet resonance imaging
mRNA	Messenger RNA
MS	Mass spectrometry
NOTCH3	Neurogenic locus notch homolog protein 3 (protein)
<i>NOTCH3</i>	Neurogenic locus notch homolog protein 3 (gene)
PBS	Phosphate-buffered saline
PCR	Polymerase chain reaction
PFA	Paraformaldehyde
pi	Post-infection
PVDF	Polyvinylidene fluoride
qPCR	Quantitative real-time PCR
RIPA	Radio-immunoprecipitation assay
RT-qPCR	Reverse transcription qPCR
SDS	Sodium dodecyl sulfate
SDS-PAGE	Sodium dodecyl sulfate polyacrylamide gel electrophoresis
SDT	SDS-DTT-Tris/HCl (lysis buffer)
SMA	α -Smooth muscle actin
SMC	Smooth muscle cell

SNPs	Single nucleotide polymorphisms
TAE	Tris-acetate-EDTA
TEMED	Tetramethylethylenediamine
TGF- β	Transforming growth factor- β
vWF	von Willebrand factor
WB	Western blot
WMHs	White matter hyperintensities
wt	Wildtype

ZUSAMMENFASSUNG

Zerebrale Mikroangiopathien sind eine wesentliche Ursache für Schlaganfälle und vaskuläre Demenz. Die zugrundeliegenden Pathomechanismen sind jedoch noch unvollständig verstanden. Daher haben sich einige monogenetische Formen als Forschungsmodelle etabliert. Hierzu gehören HTRA1-assoziierte familiäre Mikroangiopathien, die durch Funktionsverlustmutationen im *HTRA1*-Gen verursacht werden, welches die ausschließlich als Homotrimer aktive Serinprotease HTRA1 kodiert. Einige pathogene Mutationen, darunter R274Q, beeinträchtigen die multimere Bindung von HTRA1. Die Arbeitsgruppe von Martin Dichgans konnte experimentell HTRA1-D174R als komplementäre Korrektor-Mutante identifizieren, welche *in vitro* sowohl den multimeren Zustand als auch die Proteaseaktivität von HTRA1-R274Q wiederherstellt. In meiner Arbeit verwendete ich eine neuartige, die Mutation HTRA1-R274Q tragende Mauslinie. Meine Ziele waren: (i) Die Charakterisierung des zerebrovaskulären Proteoms der *Htra1^{R274Q}*-Mäuse, (ii) die Erprobung des Rescues von HTRA1-R274Q durch HTRA-D174R *in vivo* mithilfe eines adenoviralen Vektors (AAV) und (iii) die Untersuchung potenzieller dominant-negativer Effekte der Mutation R274Q. Dazu verwendete ich schwerpunktmäßig Massenspektrometrie, Immunhistochemie, Immunoblot oder RT-qPCR an Hirnschnitten oder isolierten Hirngefäßen.

Meine Ergebnisse zeigten reduzierte HTRA1-Proteinlevel in *Htra1^{R274Q}*- im Vergleich zu *Htra1^{Wildtyp (wt)}*-Mäusen. Weiterhin konnte ich in *Htra1^{R274Q}*-Hirngefäßen eine deutliche Anreicherung von Extrazellulärmatrixproteinen, v.a. FN, LTBP4, FBLN5 und EGFL8 nachweisen. Diese Proteine sind bekannte HTRA1-Substrate. Zusätzlich sind FN, LTBP4 und FBLN5 etablierte Faktoren der Elastogenese, was darauf hindeutet, dass HTRA1-Funktionsverlust ebendiese beeinflusst. Darüber hinaus etablierte ich ein Protokoll, das die selektive Analyse unterschiedlicher Hirngefäßfraktionen (große und kleine leptomeningeale vs. parenchymale Gefäße) erlaubt. Anhand dieses Protokolls zeigte ich, dass die in *Htra1^{R274Q}*-Hirngefäßen angereicherten Proteine vor allem in leptomeningealen *Htra1^{wt}*-Gefäßen exprimiert werden und in *Htra1^{R274Q}*-Gefäßen ebendort akkumulieren. Trotz effektiver Transduktion parenchymaler Gefäße führte eine Infektion mit AAV-HTRA1-D174R nicht zu einer Linderung des molekularen Phänotyps der *Htra1^{R274Q}*-Hirngefäße. Dies ist dadurch erklärbar, dass sich die molekularen Veränderungen vor allem in leptomeningealen *Htra1^{R274Q}*-Gefäßen finden, die – wie ich feststellen konnte – nicht durch das verwendete AAV transduziert werden. Zuletzt untersuchte ich anhand der *Htra1^{R274Q}*-Mauslinie potenzielle dominant-negative Effekte der Mutation R274Q. Um zu evaluieren, ob das R274Q-Allel mit dem wt-Allel interferiert, verglich ich die Hirngefäße von *Htra1^{wt/R274Q}*- und haploinsuffizienten *Htra1^{+/-}*-Mäusen. In *Htra1^{wt/R274Q}*-Hirngefäßen konnte ich keine verstärkte FN- und LTBP4-Akkumulation feststellen, was eher gegen dominant-negative Eigenschaften der Mutation R274Q spricht.

Meine Ergebnisse tragen zum Verständnis der Pathophysiologie HTRA1-assoziiertes familiärer Mikroangiopathien bei. Insbesondere konnte ich in leptomeningealen *Htra1*^{R274Q}-Hirngefäßen eine Dysregulation von in die Elastogenese involvierten Extrazellulärmatrixproteinen aufzeigen. Zukünftige Studien könnten darauf aufbauend die multimere Anordnung oder Stabilität von HTRA1 und damit potenzielle Therapieoptionen zum Ziel haben.

ABSTRACT

Cerebral small vessel disease (cSVD) is a significant cause of stroke and vascular dementia, while the underlying pathomechanisms are poorly understood. Several monogenic forms have emerged as instrumental models to examine the pathophysiology of cSVD. Among these, HTRA1-related familial cSVDs are linked to loss-of-function mutations in the *HTRA1* gene encoding the secreted homotrimeric serine protease HTRA1. A subset of pathogenic mutations, including R274Q, impair the multimeric assembly of HTRA1. The laboratory of Martin Dichgans experimentally identified HTRA1-D174R as a complementary corrector mutation able to restore both multimeric state and protease function of HTRA1-R274Q *in vitro*. Using a novel mouse line bearing the HTRA1-R274Q mutation, the aims of my work were to (i) characterize the cerebrovascular proteome of *Htra1^{R274Q}* mice, (ii) explore the rescue of HTRA1-R274Q by HTRA1-D174R *in vivo* using an adeno-viral vector (AAV), and (iii) investigate putative dominant-negative effects of mutation R274Q. For this purpose, I mainly applied mass spectrometry, immunohistochemistry, immunoblot, or RT-qPCR to mouse brain sections or to isolated mouse brain vessels.

First, I detected a marked reduction of HTRA1 protein levels in *Htra1^{R274Q}* compared to *Htra1^{wildtype (wt)}* animals. Second, I highlighted a distinct accumulation of extracellular matrix (ECM) proteins, especially fibronectin (FN), LTBP4, FBLN5, and EGFL8, in *Htra1^{R274Q}* brain vessels. Second, I highlighted a distinct accumulation of extracellular matrix (ECM) proteins, especially fibronectin (FN), LTBP4, FBLN5, and EGFL8, in *Htra1^{R274Q}* brain vessels. These proteins are all documented HTRA1 substrates. Notably, FN, LTBP4, and FBLN5 are well-described elastogenic factors, suggesting that HTRA1 loss-of-function interferes with elastogenesis. Moreover, I established a novel vessel isolation protocol that allows the proteomic analysis of distinct brain vessel fractions (large and small leptomeningeal vessels vs. parenchymal vessels). Using this protocol, I found that the proteins enriched in *Htra1^{R274Q}* vessels are primarily expressed in leptomeningeal *Htra1^{wt}* vessels, and that the leptomeningeal vasculature is their predominant site of accumulation in *Htra1^{R274Q}* vessels. Infection with AAV-HTRA1-D174R did not alleviate the molecular phenotype of *Htra1^{R274Q}* brain vessels despite efficient and long-term transduction of parenchymal capillaries. This can be explained by the fact that the primary site of molecular alterations in *Htra1^{R274Q}* brain vessels are leptomeningeal arteries and arterioles, which I found not to be targeted by the used AAV. Furthermore, I took advantage of the *Htra1^{R274Q}* mouse line to examine putative dominant-negative effects of mutation R274Q. Specifically, I compared brain vessels from *Htra1^{wt/R274Q}* and haploinsufficient *Htra1^{+/-}* mice to evaluate whether the R274Q allele interferes with the function of the wt allele. I found no exacerbation of FN and LTBP4 accumulation in *Htra1^{wt/R274Q}* brain vessels, speaking rather against dominant-negative properties of mutation R274Q.

Collectively, my observations provide new insights into the mechanisms underlying HTRA1-related cSVD. In particular, my results highlight a deregulation of ECM proteins involved in elastogenesis in the leptomenigeal vasculature of *Htra1*^{R274Q} mice. My work further opens perspectives for future intervention targeting HTRA1 multimeric assembly or stability and potential therapeutic applications.

1 INTRODUCTION

1.1 Cerebral small vessel disease (cSVD)

Cerebral small vessel disease (cSVD) is a heterogenic syndrome of clinical, cognitive, neuroimaging, and neuropathologic findings caused by pathologic changes in the cerebral perforating arteries, arterioles, capillaries, and venules (Figure 1.1; Haffner et al., 2016). cSVD is one of the most frequent age-related conditions and is responsible for most hemorrhagic strokes and 20–25% of all ischemic strokes (Wardlaw et al., 2019). Moreover, cSVD is a significant cause of vascular dementia, often occurring together with Alzheimer dementia and therefore contributing to 50% of all dementias (Bos et al., 2018). The causes for sporadic cSVD are multifactorial. Besides age, other important risk factors include hypertension, diabetes mellitus, dyslipidemia, and smoking (Pantoni, 2010, Thompson et al., 2009). In addition, there is growing evidence that genetic components play a role not only in Mendelian but also in sporadic forms of cSVD (Haffner et al., 2016). Non-amyloid cSVD is to be distinguished from cerebral amyloid angiopathy (CAA), caused by β -amyloid deposits in the cerebrovasculature (Greenberg, 2021).

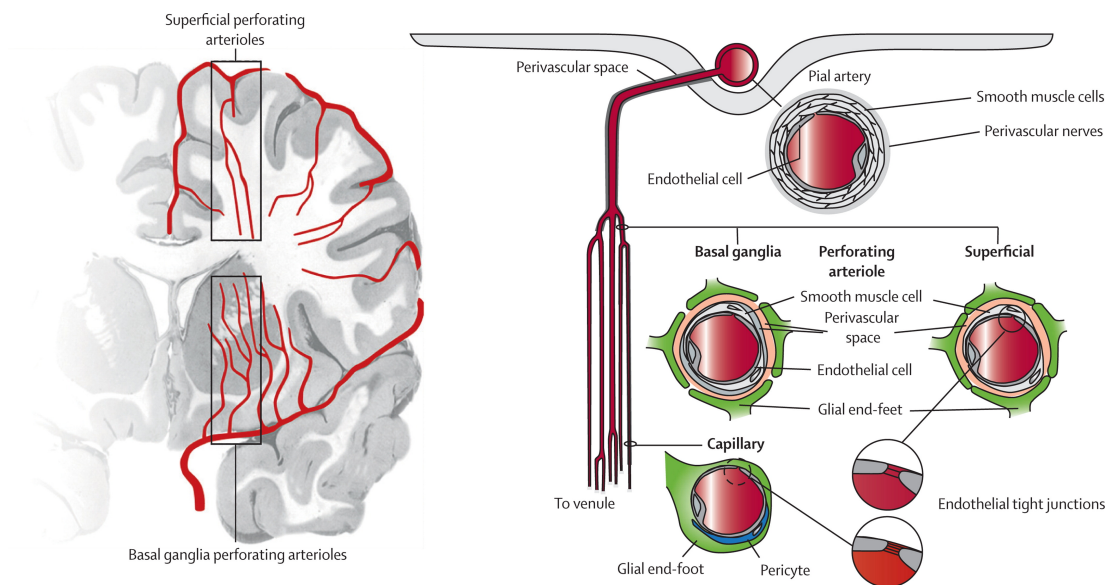


Figure 1.1 Brain vessel architecture and composition of arteries, arterioles, and capillaries

Origin and typical branching pattern of perforating arteries and arterioles (left panel). Composition of the vessel wall of arteries, arterioles, and capillaries (right panel).
Figure from Wardlaw et al., 2013a.

The presentation of cSVD ranges from clinically silent lesions or very subtle neurological symptoms to cognitive decline and dementia, gait and balance dysfunction, mood disorders such as depression, and stroke with its sudden neurological deficits (Pantoni, 2010, Wardlaw

et al., 2013a, Wardlaw et al., 2019). As there is no specific biomarker for cSVD, diagnosis is made through a combination of clinical and neuroradiological criteria (Smith et al., 2021).

Typical neuroimaging features of cSVD are white matter hyperintensities (WMHs) of presumed vascular origin on T2-weighted magnetic resonance imaging (MRI) sequences, lacunes (i.e., old small infarcts in the subcortical brain regions), and recent small subcortical infarcts, microbleeds, perivascular spaces, and brain atrophy (STRIVE criteria: Standards for Reporting Vascular Changes on Neuroimaging; Figure 1.2, A–D; Smith et al., 2021, Wardlaw et al., 2019, Wardlaw et al., 2013b). The relationship between lesions and symptoms is very variable and not fully understood. Single lesions can be clinically silent or cause severe symptoms, depending on the lesion's location, the patient's pre-existing conditions, and other factors. However, the severity of clinical symptoms usually correlates with lesion burden (Wardlaw et al., 2019). Additionally, brain damage is not limited to visible lesions on standard neuroimaging methods, as the most sensitive MRI methods reveal damage even in normal-appearing brain regions (Muñoz Maniega et al., 2017).

Typical histopathological findings in sporadic cSVD include (i) intimal thickening (the intima, which is the innermost part of the vessel, consists of a single layer of endothelial cells), (ii) hyalinization with loss of medial smooth muscle cells (SMCs) and accumulation of extracellular matrix (ECM) components, and (iii) fibrinoid necrosis, microaneurysms, deposition of atheromatous material, and luminal narrowing in advanced stages (Figure 1.2, E–G; Craggs et al., 2014, Pantoni, 2010).

The pathomechanisms underlying sporadic cSVD are still poorly understood, and suitable experimental models to investigate the disease and test candidate therapies are currently missing. Consequently, there is a lack of effective prevention and treatment modalities (Wardlaw et al., 2019).

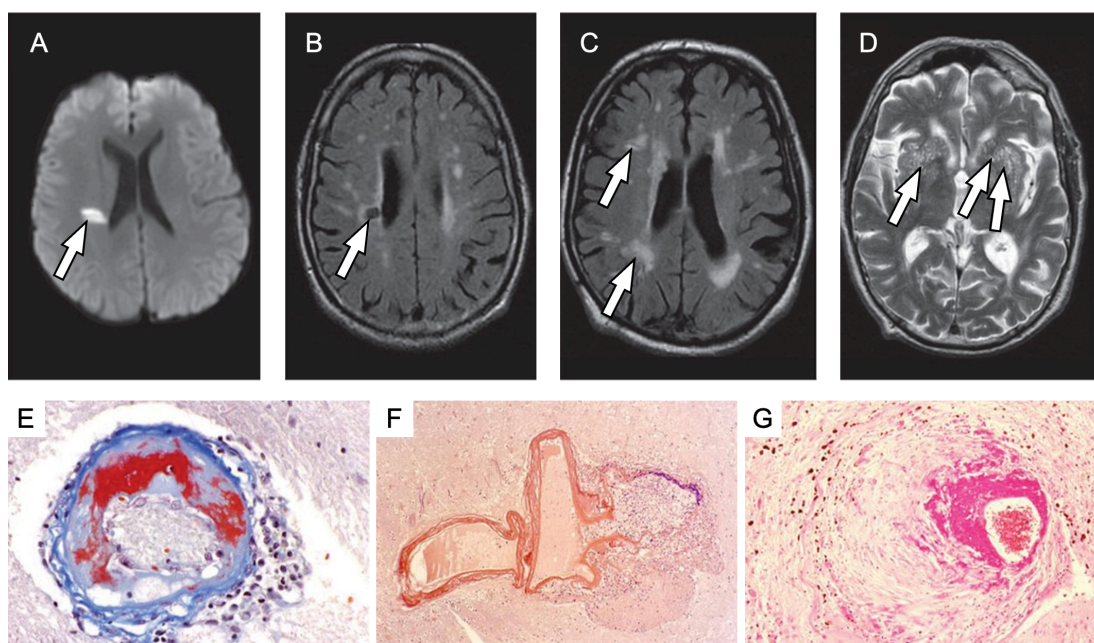


Figure 1.2 Radiological and histopathological features of sporadic cSVD

(A–D) Radiological findings on MRI marked by arrows: (A) Small deep lacunar infarct on diffusion-weighted imaging (DWI); (B) periventricular lacune containing cerebrospinal fluid and (C) WMHs on fluid-attenuated inversion recovery (FLAIR) imaging; (D) perivascular spaces on T2 sequence. (E–G) Histopathological findings: (E) Lipohyalinosis (Masson's trichrome stain, magnification x100); (F) microaneurysm with fibrinoid necrosis of the aneurysmal wall (haematoxylin and eosin (H&E) stain, x25); (G) fibrinoid necrosis (H&E, x20).

(A–D) adapted from Wardlaw et al., 2013a, (E–G) adapted from Pantoni, 2010.

Besides sporadic cSVD, several familial (monogenic) forms have been reported and have emerged as instrumental models to examine the pathophysiology of cSVD. Indeed, familial cSVDs share several clinical and pathological features with sporadic cSVD. As a distinct advantage, they can be transferred into animal models by modifying the known causative gene (Joutel et al., 2016). Monogenic cSVDs include, among others:

Cerebral autosomal dominant arteriopathy with subcortical infarcts and leukoencephalopathy (CADASIL). Cerebral autosomal dominant arteriopathy with subcortical infarcts and leukoencephalopathy (CADASIL, OMIM #1253101) is caused by heterozygous mutations in the *NOTCH3* gene, which encodes the membrane signaling receptor neurogenic locus notch homolog protein 3 (NOTCH3). Pathogenic mutations typically disrupt or introduce cysteine residues and result in an extracellular accumulation of granular osmiophilic material (GOMs) within the vascular wall. GOMs are essentially composed of NOTCH3 aggregates along with other ECM proteins. The pathomechanisms underlying CADASIL are still debated. They are proposed to include, among others, aberrant NOTCH3 signaling and GOM-related cytotoxicity. With an estimated prevalence of 2–5/100 000, CADASIL is the most frequent and most extensively studied familial cSVD (Chabriat et al., 2009, Di Donato et al., 2017a, Joutel et al., 1996).

¹ Online Mendelian Inheritance in Man, OMIM®. Johns Hopkins University, Baltimore, MD. URL: <https://omim.org/>

HTRA1-related familial cSVDs: Cerebral autosomal recessive arteriopathy with subcortical infarcts and leukoencephalopathy (CARASIL) and HTRA1-related late-onset small vessel disease. HTRA1-related familial vasculopathies (OMIM #600142 and #6167791) are linked to loss-of-function mutations in the *HTRA1* gene, which encodes the secreted protease high-temperature requirement serine peptidase A1 (HTRA1). While both mono- and biallelic mutations can be causative, homozygous or compound heterozygous mutation carriers display an earlier onset and a more severe phenotype. A detailed description of these disorders is provided in section 1.2.

COL4A1/A2-related angiopathies. COL4A1/A2-related angiopathies (OMIM #607595 and #6145191) are multisystem disorders with a broad and heterogeneous phenotypic spectrum including typical cSVD symptoms as well as cardiac, renal, and ocular abnormalities. They are caused by heterozygous mutations in the *COL4A1* and *COL4A2* genes, encoding the $\alpha 1$ and $\alpha 2$ chain of type IV collagen, respectively (*COL4A1* and *COL4A2*). These collagens assemble as heterotrimers ($\alpha 1\alpha 1\alpha 2$) and, upon secretion, form a network-like structure which is one of the main components of the basement membrane. Among other pathomechanisms, *COL4A1/2* mutations have been proposed (i) to cause intracellular accumulation of misfolded heterotrimers with cytotoxic consequences or (ii) to impair the extracellular assembly of the collagen IV-network, leading to structural damage of the basement membrane and altered interaction with other ECM components (Gould et al., 2006, Haffner et al., 2016, Kuo et al., 2012).

Although familial cSVDs are rare conditions with independent causative genetic defects, analyses of these disorders have highlighted convergent cSVD pathways. As a remarkable example, it has emerged that perturbations of the so-called cerebrovascular matrisome (i.e., the sum of all proteins constituting the ECM as well as all proteins associated with the ECM) play a central role in the pathogenesis of cSVDs (Joutel et al., 2016).

1.2 HTRA1: an emerging player in cSVD

1.2.1 Pathogenic *HTRA1* mutations are causative for familial cSVD

1.2.1.1 Identification of *HTRA1* as a causative gene for familial cSVD

In the 1970s, Maeda and colleagues reported a novel form of cSVD (Maeda et al., 1976). The disorder affected non-hypertensive young adults from consanguineous families and was fatal within 10 years. Manifestations included dementia, pseudobulbar palsy, pyramidal and extrapyramidal symptoms, along with alopecia and lumbago. Based on its recessive inheritance pattern and its resemblance to CADASIL, the disease was named CARASIL (cerebral autosomal recessive arteriopathy with subcortical infarcts and leukoencephalopathy, OMIM #600142¹) in the mid-nineties (Bowler et al., 1994).

In 2009, Hara and colleagues performed gene linkage and sequencing analysis in 5 CARASIL families. They demonstrated that biallelic mutations within the *HTRA1* gene on chromosome 10q25, encoding the protease HTRA1, are causative for CARASIL (Hara et al., 2009).

Until recently, CARASIL was thought to have a strictly recessive inheritance pattern. However, in 2015, Verdura and colleagues identified heterozygous *HTRA1* mutations in an autosomal-dominant cSVD family. They further established that up to 5% of patients suffering familial cSVD of unknown origin exhibit pathogenic *HTRA1* mutations (Verdura et al., 2015). Since then, the contribution of monoallelic *HTRA1* mutations to late-onset cSVD has been confirmed in independent cSVD cohorts and various single cases (see Figure 1.6; Di Donato et al., 2017b, Nozaki et al., 2016, Uemura et al., 2020). The name of this new form of familial cSVD is a matter of discussion. Due to its dominant inheritance pattern, it was proposed to name the disease CADASIL type 2 (CADASIL 2, OMIM #616779¹). In my thesis, I will use the term "HTRA1-related late-onset cSVD" to refer to symptomatic carriers of monoallelic *HTRA1* mutations, as recently suggested (Uemura et al., 2020).

1.2.1.2 Clinical features of HTRA1-related familial cSVD

CARASIL patients suffer early-onset progressive dementia, gait disturbance, and recurrent ischemic strokes. The mean age at onset of neurological symptoms is 29.5 years (range 20–40 years), after which the disease progresses steadily. In addition to WMHs (Figure 1.3, A), 40–50% of probands experience episodes of ischemic stroke, especially lacunar infarcts in the basal ganglia or brain stem (Figure 1.3, B). A hemorrhagic stroke has been reported in one single case. Other common neurological signs and symptoms include pseudobulbar palsy, hyperreflexia, Babinski sign, urinary incontinence, horizontal nystagmus, mood changes, and seizures. In contrast to CADASIL, migraines are rare in CARASIL patients. While cSVDs frequently also affect retinal and renal vessels, retinal vascular changes have only been reported in one patient, and there are no known cases of renal dysfunction in CARASIL (Fukutake, 2011, Nozaki et al., 2014, Uemura et al., 2020). The mean survival after the onset of neurological symptoms is 10 years, although survival up to 20–30 years has been reported (Fukutake, 2011, Uemura et al., 2020).

CARASIL patients typically display non-neurological symptoms, including acute middle to lower back pain (lumbago; Figure 1.3, C) and premature baldness (alopecia; Figure 1.3, D). Almost all patients experience lumbago due to spondylosis deformans or disk herniation; however, lumbago sometimes develops earlier without radiological correlate. Although it is not present in all patients, hair loss is usually the earliest symptom.

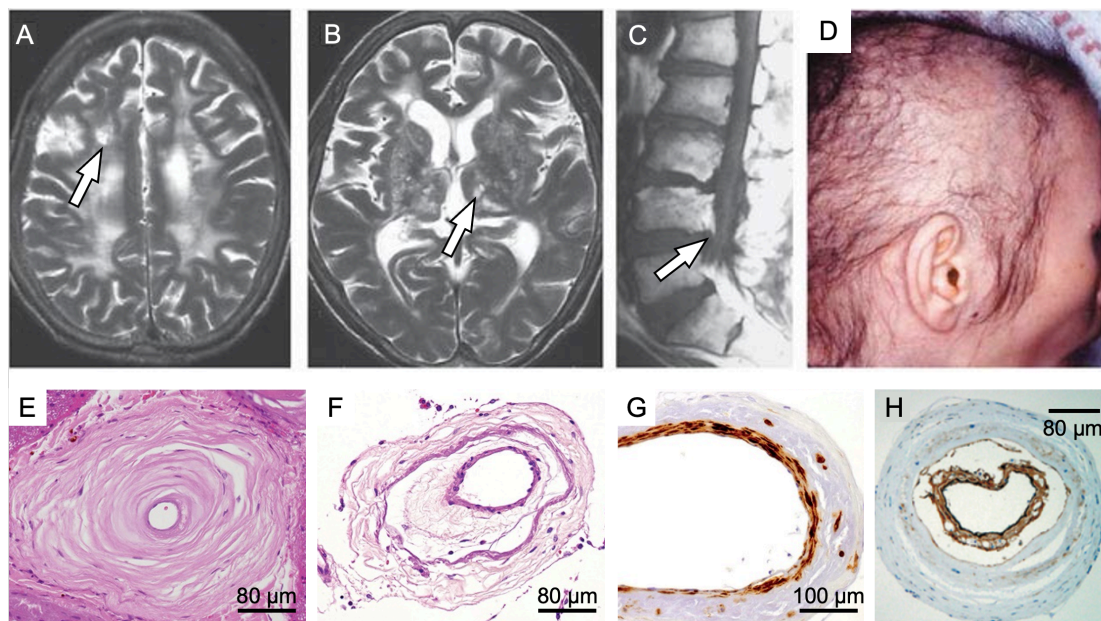


Figure 1.3 Radiological, clinical, and histopathological findings in HTRA1-related cSVD

(A–C) Radiological findings in a CARASIL case marked by arrows: (A) WMHs and (B) ischemic region in the thalamus on T2-weighted brain MRI; (C) spondylotic changes of the lumbar spine on T1-weighted lumbar MRI. (D) Diffuse hair loss in a CARASIL patient. (E–H) Histopathology of CARASIL brain vessels: (E) intimal fibrosis, hyalinosis, and luminal narrowing; (F) splitting of the internal elastic lamina, SMC loss, and fibrosis of the adventitia; (G) loss of the SMC marker α -smooth muscle actin (SMA); (H) increased intimal expression of the extra-domain A region of fibronectin. (E–F) Leptomeningeal arterioles (H&E); (G–H) parenchymal arteries (immunohistochemical stainings).

(A–D and H) adapted from Hara et al., 2009 (reproduced with permission from Hara et al., 2009, Copyright Massachusetts Medical Society), (E–G) adapted from Ito et al., 2018.

There is no clear predominance of the disease's distribution between men and women. Notable is the absence of hypertension, diabetes mellitus, and dyslipidemia (i.e., all major risk factors for sporadic cSVD) in CARASIL patients.

Compared to CARASIL cases, monoallelic mutation carriers display a later age of onset (mean age at onset of neurological symptoms: 54.1 years) and a milder phenotype (Uemura et al., 2020). Spondylosis deformans and alopecia can be present but are much less frequent than in CARASIL probands (Nozaki et al., 2016, Uemura et al., 2020, Verdura et al., 2015). Other differences include a preference for males and a higher prevalence of hypertension (Uemura et al., 2020).

There are no published clinical diagnostic criteria for HTRA1-related familial cSVD. The disease should particularly be suspected in patients presenting with extended WMHs on MRI in combination with some of the above-described symptoms or relevant family history. Laboratory results and skin biopsy are non-conclusive. Upon clinical suspicion, diagnosis relies on genetic testing (i.e., identifying a pathogenic variant in the *HTRA1* gene; Onodera et al., 2010).

Neither a causative therapeutic option nor consensus guidelines are available for HTRA1-related familial cSVD. Management of affected individuals includes treatment of symptoms and offering genetic counseling to relatives (Onodera et al., 2010).

1.2.1.3 Radiological findings in HTRA1-related familial cSVD

T2-weighted brain MRI shows diffuse symmetrical (and later confluent) WMHs, especially periventricular and in the deep white matter. In contrast, U-fibers (i.e., the superficial white matter) remain relatively unaffected (Figure 1.3, A–B). In CARASIL cases, WMHs start to appear at the age of 20 years and precede neurological symptoms (Fukutake, 2011). In monoallelic mutation carriers, WMHs appear later (Ito et al., 2018, Nozaki et al., 2016, Uemura et al., 2020). Lacunar infarcts are found mainly in the brain stem, basal ganglia, thalamus, and deep white matter. Patients progressively develop diffuse brain atrophy and pancerebral microbleeds (Nozaki et al., 2014). Single-photon emission computer tomography in single patients revealed reduced cerebral blood flow in various parts of the brain (Fukutake, 2011, Nozaki et al., 2014). Arteriosclerotic-like findings in cerebral angiography have been reported in some cases (Fukutake et al., 1995). Magnet resonance spectroscopy in one patient suggested ischemia-induced demyelination without neuroaxonal degeneration (Nishimoto et al., 2011b).

1.2.1.4 Histopathological findings in HTRA1-related familial cSVD

Histopathological findings in mono- and biallelic *HTRA1* mutation carriers are essentially similar (Ito et al., 2018, Nozaki et al., 2016, Uemura et al., 2020). Pathological changes of the brain vasculature are classically observed in arteries and arterioles of the cerebral white matter, basal ganglia, and leptomeninges (Arima et al., 2003).

The vessels show concentric narrowing of the lumen with arteriosclerotic changes, including the following features:

- Fibrous intimal proliferation with splitting of the internal elastic lamina (Figure 1.3, E–F) and accumulation of fibronectin (Figure 1.3, H; Hara et al., 2009, Ito et al., 2016, Oide et al., 2008). Endothelial cells remain preserved.
- Thinning of the media (i.e., the central layer of the vessels, mainly composed of SMCs) with hyaline degeneration (Figure 1.3, E). The thinning correlates with an extensive loss of SMCs (comparable to changes observed in sporadic cSVD) with reduction of α -smooth muscle actin (SMA; Figure 1.3, F–G) and accumulation of lysosome-like bodies in the cytoplasm of SMCs (Arima et al., 2003, Yanagawa et al., 2002).
- Thinning of the adventitia (i.e., the most external layer of the vessels, composed of SMCs and fibroblasts; Figure 1.3, F) with decreased immunoreactivity for collagens, possibly resulting from mural ECM loss (Oide et al., 2008).

A diffuse myelin pallor with sparing of U-fibers and multiple foci of perivascular softening is usually found in the cerebral white matter, basal ganglia, and brain stem (Nozaki et al., 2014) and correlates with WMHs.

Of note, depositions of GOMs, which are typically observed in CADASIL, are not detected in CARASIL. Similarly, other specific features of neurodegenerative disorders such as amyloid

deposits, senile plaques, neurofibrillary tangles, or Lewy bodies are absent (Arima et al., 2003, Yanagawa et al., 2002).

Manifestations in other organs and skin are seldom reported and probably correspond to incidental findings (Cai et al., 2015, Ito et al., 2018, Thaler et al., 2018, Wang et al., 2012, Yanagawa et al., 2002).

1.2.2 Deregulation of HTRA1 in other cerebrovascular disorders

Although HTRA1-related familial cSVDs provide an obvious link between the deregulation of HTRA1 and human disease, other observations suggest a more general role of HTRA1 in cSVD.

First, HTRA1 deregulation has recently been reported in other familial and sporadic cSVDs. An analysis of the brain vasculature of CADASIL and sporadic CAA patients via proteomics and immunohistochemistry (IHC) demonstrated a marked accumulation of HTRA1 (Figure 1.4; Hondius et al., 2018, Zellner et al., 2018). This was accompanied by the accumulation of a large set of HTRA1 substrates, strongly suggesting that, as in HTRA1-related familial cSVD, HTRA1 activity is likewise disrupted in these diseases (Zellner et al., 2018).

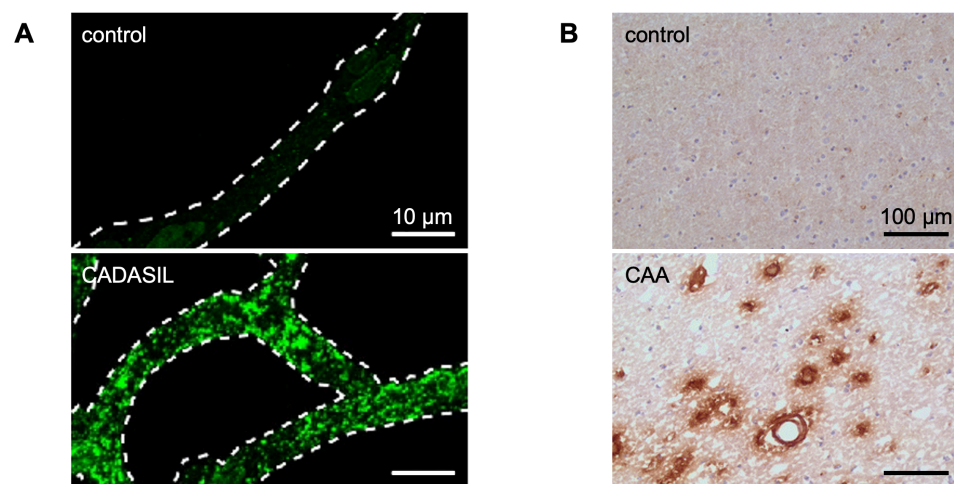


Figure 1.4 Vascular accumulation of HTRA1 in other brain vessel diseases

(A) Immunofluorescent staining of HTRA1 (green) in brain arteries of a CADASIL patient and a control subject (dashed lines: vessel outline). (B) Immunohistochemical staining of HTRA1 (brown) in brain arteries of a CAA case and a control subject.

(A) adapted from Zellner et al., 2018, (B) adapted from Hondius et al., 2018.

Second, genome-wide association studies (GWAS) revealed that common genetic variants (single nucleotide polymorphisms, SNPs) in genes involved in monogenic cSVD confer risk of sporadic cSVD hallmarks like WMHs and stroke. In addition to *NOTCH3* and *COL4A1/2* (the causative genes of CADASIL and COL4-related angiopathies, respectively, see section 1.1), these genes include *HTRA1* (Malik et al., 2018, Rannikmäe et al., 2015, Schmidt et al., 2011).

Collectively, these findings imply that HTRA1 plays a significant role in cSVD and stroke.

1.3 Molecular mechanisms underlying the pathogenicity of HTRA1 mutations

1.3.1 HTRA1 is expressed in the cerebrovasculature

HTRA1 is a highly conserved and ubiquitously expressed serine protease, including in the species human and mouse. In the brain vasculature, HTRA1 is predominantly produced by astrocytes. However, all other major vascular cell types (i.e., endothelial cells, SMCs, pericytes, and fibroblasts) also synthesize the enzyme across the whole arteriovenous axis (i.e., arteries, arterioles, capillaries, and veins; Figure 1.5).

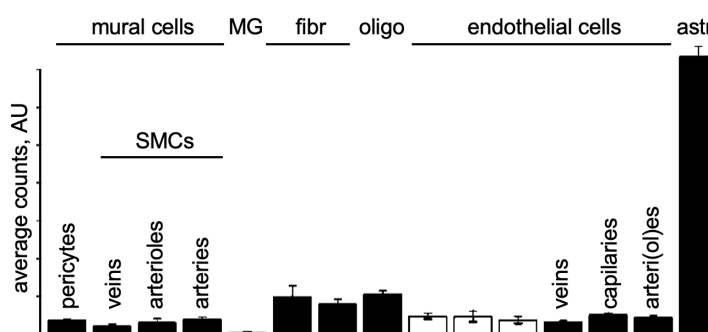


Figure 1.5 HTRA1 expression among various cerebrovascular cell types

Gene expression of HTRA1 in single cells is depicted by average counts per cell (arbitrary units, AU). (MG: microglia, fibr: fibroblasts, oligo: oligodendrocytes, astr: astrocytes)
Data retrieved from the Vascular Single Cells database² (He et al., 2018, Vanlandewijck et al., 2018).

1.3.2 Pathogenic HTRA1 mutations disrupt the protease activity of HTRA1

HTRA1 consists of three distinct functional domains. They comprise a trypsin-like protease domain with a catalytic triad (composed of the residues His220, Asp250, and Ser328 forming the active site) as well as an N-terminal Mac domain (made of an insulin-like growth factor-binding protein (IGFBP) domain and a Kazal-like domain), and a C-terminal PDZ domain (see Figure 1.6; Clausen et al., 2002, Truebestein et al., 2011). The function of these extensions, which are involved in protein-protein interactions, is not well elucidated. *In vitro*, they are fully dispensable for protease activity (Eigenbrot et al., 2012).

To date, more than 70 different HTRA1 mutations have been reported in cSVD cases (Uemura et al., 2020). Most disease-causing mutations are point mutations typically targeting the catalytic domain of HTRA1 (Figure 1.6). Moreover, the protease activity of the resulting mutants was found to be markedly reduced compared to that of wildtype (wt) HTRA1 *in vitro* (Beaufort et al., 2014, Nozaki et al., 2016, Uemura et al., 2019). Thus, the loss of HTRA1 protease function is a key pathomechanism in HTRA1-related cSVD.

² URL: <http://betsholtzlab.org/VascularSingleCells/database.html>

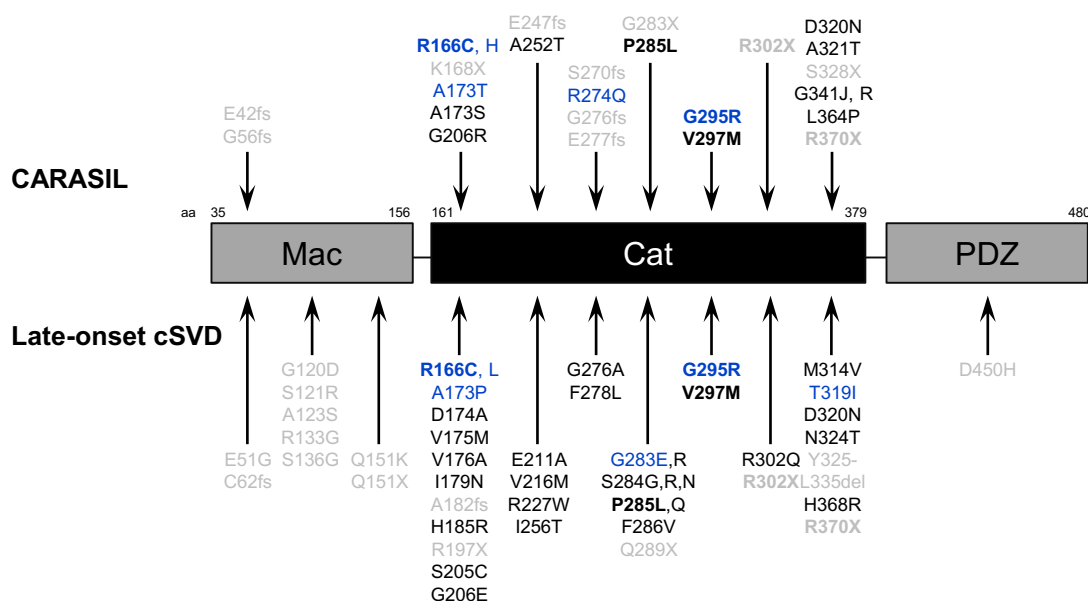


Figure 1.6 Mutations identified in HTRA1-related cSVD

Arrows indicate the location of mutations identified in CARASIL (top) and HTRA1-related late-onset cSVD along the amino acids (aa) in HTRA1 protein. Black font: missense mutations within the catalytic domain; blue: mutations resulting in defective trimerization; grey: all other mutations; bold letters: mutations identified in both CARASIL and HTRA1-related late-onset cSVD. Functional domains are represented by boxes.

(Mac: N-terminal Mac domain, Cat: catalytic domain, PDZ: C-terminal PDZ-domain)

References for mutations (including reviews referring to the original articles): Di Donato et al., 2017b, Hara et al., 2009, Liu et al., 2020, Muthusamy et al., 2021, Nozaki et al., 2014, Oluwole et al., 2020, Pati et al., 2018, Shang et al., 2021, Tan et al., 2019, Uemura et al., 2020, Uemura et al., 2019, Verdura et al., 2015, Yu et al., 2020, Zhuo et al., 2020, Ziaei et al., 2019, unpublished results.

1.3.3 HTRA1 loss of function leads to an accumulation of secreted and matrisomal HTRA1 substrates

HTRA1 is involved in various cellular processes such as protein quality control, signaling, and proliferation (Clausen et al., 2011). It is a secreted protein that can associate with the ECM (Beaufort et al., 2014). Accordingly, the known substrates of HTRA1 include a variety of extracellular and matrisomal proteins, such as, e.g., fibronectin (FN), vitronectin, and fibulin 5 (FBLN5).

HTRA1 has also been shown to target several members of the transforming growth factor β (TGF- β) signaling pathway, such as TGF- β itself, some TGF- β receptors, and its ligand latent TGF- β binding protein 1 (LTBP1) (Beaufort et al., 2014, Graham et al., 2013, Shiga et al., 2011). The TGF- β pathway plays a crucial role in blood vessel homeostasis (ten Dijke et al., 2007). Moreover, TGF- β signaling alterations have been linked to several vascular diseases, including sporadic cSVD (Thompson et al., 2009), hereditary hemorrhagic telangiectasia (Jakobsson et al., 2013, ten Dijke et al., 2007), and CADASIL (Kast et al., 2014). Thus, TGF- β signaling deregulation might be a common denominator in cSVD (Müller et al., 2017). However, conflicting data suggest that HTRA1 either inhibits or facilitates TGF- β signaling (Beaufort et al., 2014, Graham et al., 2013, Shiga et al., 2011), and the status of the TGF- β pathway in HTRA1-related cSVD remains debated.

Since HTRA1 loss of function should impair the processing of its substrates, their accumulation is presumed to play a central role in HTRA1-related cSVD. This hypothesis is supported by recent findings from the laboratory of Martin Dichgans, showing that (i) brain vessels from *Htra1*^{knockout (ko)} mice are enriched in secreted and ECM proteins, and (ii) a variety of proteins upregulated in *Htra1*^{ko} brain vessels represent HTRA1 substrates (Zellner et al., 2018).

1.3.4 A subset of pathogenic mutations impairs the multimeric assembly of HTRA1

HTRA1 is an oligomultimeric protease that exists as an equilibrium between monomers and trimers (Clausen et al., 2011). The conversion of HTRA1 from the resting to the active state involves large conformational rearrangements that require crosstalk between adjacent protomers (Eigenbrot et al., 2012, Truebestein et al., 2011). Therefore, the multimeric assembly of HTRA1 is mandatory for activity.

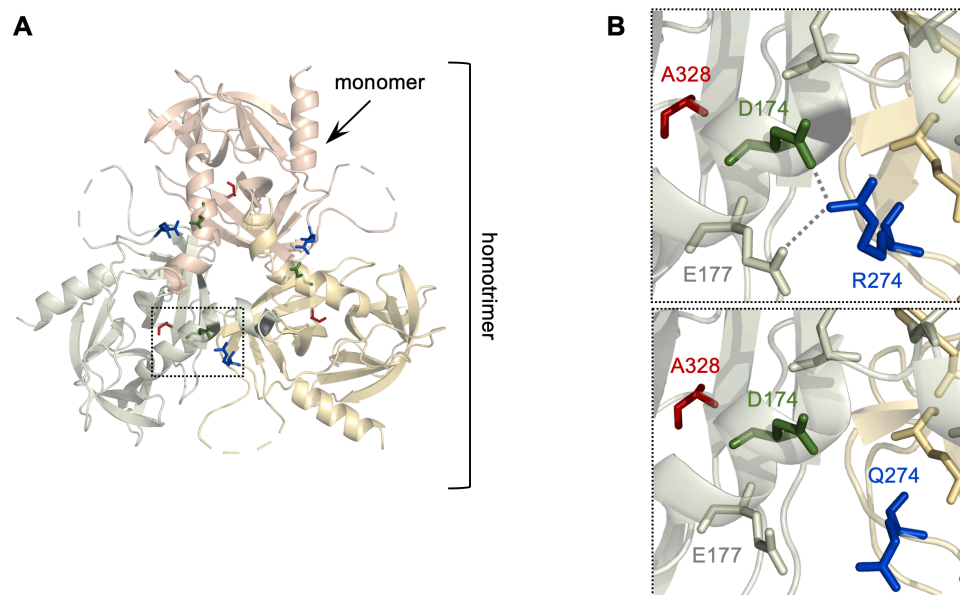


Figure 1.7 The disease-causing mutation R274Q affects HTRA1 trimer interface

(A) HTRA1 assembles as a homotrimer to form a proteolytically active complex. Protomers are depicted in light red, yellow, and green. (B) In wt HTRA1 (upper panel), R274 (blue) forms salt bridges with D174 (green) and E177 (grey) of a neighboring protomer. Both interactions are disrupted by the disease-causing mutation R274Q (lower panel). The active site mutation S328A is depicted in red. Figure adapted with permission of ISD München, unpublished data.

HTRA1 trimer is stabilized by a central hydrophobic cluster of aromatic residues and a network of lateral polar contacts between adjacent protomers. Of importance, several pathogenic HTRA1 mutations disturb the protomer-protomer interface. These mutations include, e.g., R166C/H/L, A173T/P, G295R as well as R274Q, on which my thesis focuses (Institute for Stroke and Dementia Research/Institut für Schlaganfall- und Demenzforschung (ISD) München, unpublished data). As shown in Figure 1.7, in wt HTRA1, R274 forms hydrogen bonds with E174 and E177 on an adjacent protomer. Both interactions are disrupted by mutation R274Q, which should destabilize the HTRA1 trimer. Accordingly, biochemical

analysis indicated that — in contrast to trimeric wt HTRA1 — the corresponding disease-causing mutants along with G283E and T319I (for which computational simulations were not performed) primarily exist as monomers (see Figure 1.6, monomeric mutants are highlighted in blue; Nozaki et al., 2016, Uemura et al., 2019, ISD München, unpublished results).

1.3.5 The rational correction of HTRA1 multimeric assembly defects restores HTRA1 protease activity

In an effort to achieve the functional correction of pathogenic HTRA1, the laboratory of Martin Dichgans selected R274Q as a model mutation and searched for complementary mutations located on an adjacent monomer at the exact opposite position of R274Q. Via a mutational screening strategy and *in vitro* biochemical assays, they identified D174R as a potent corrector of R274Q. Specifically, they designed a rescue variant that displays both the corrector mutation (D174R) and an active site mutation replacing the catalytic Ser328 with an Ala (i.e., S328A). Using purified proteins or transfected cells, they could evidence that the rescue variant — which is devoid of proteolytic activity — restores both the multimeric state and the protease function of HTRA1-R274Q (ISD München, unpublished results).



Figure 1.8 Functional correction of R274Q by the complementary mutation D174R

Addition of a proteolytically inactive HTRA1 variant harboring both the corrector mutation D174R (green) and an active site mutation S328A (red) is sufficient to repair the oligomeric assembly and restore the protease activity of HTRA1-R274Q (blue).

Figure adapted with permission of ISD München, unpublished data.

These observations indicate that in mutant R274Q — and possibly in other monomeric mutants — multimeric assembly defects are the main cause for the loss of protease activity. Most importantly, they pinpoint the use of corrector HTRA1 variants as a promising strategy for intervention that was still missing validation *in vivo*.

1.3.6 Mutations that interfere with the multimeric assembly of HTRA1 might display dominant-negative properties

As stated in section 1.2.1, HTRA1-related cSVD was initially described as a strictly recessive disorder, with only a few parents of CARASIL cases having a family history of stroke or leukoencephalopathy (Hara et al., 2009). Meanwhile, however, it has been well established that disruption of a single *HTRA1* allele is sufficient to cause cSVD (Di Donato et al., 2017b, Nozaki et al., 2016, Uemura et al., 2020, Verdura et al., 2015). Whether this is restricted to a subset of mutations and what could be the underlying pathomechanism is still debated.

On the one hand, dominant-negative properties have been proposed to be linked to distinct mutations, based on patient data analysis and *in vitro* assays showing that the corresponding mutant proteins interfere with the activity of wt HTRA1 (Lee et al., 2018, Nozaki et al., 2016, Uemura et al., 2019). These "dominant" mutations include mutations that impair the multimeric assembly of HTRA1, such as R274Q, as well as mutations involved in its activation cascade (Uemura et al., 2020). However, *in vivo* observations confirming these dominant-negative effects are lacking.

On the other hand, haploinsufficiency might be sufficient to cause a milder and less penetrant disorder. Interestingly, compared to CARASIL patients, symptomatic heterozygous cases include more males and exhibit more vascular risk factors, suggesting that other genetic and environmental factors might be involved in HTRA1-related late-onset cSVD (Uemura et al., 2020).

2 AIMS OF THE PROJECT

The laboratory of Martin Dichgans recently generated a mouse model bearing the HTRA1-R274Q mutation, as identified in two independent CARASIL pedigrees (Badachi et al., 2020, Nishimoto et al., 2011a).

Using this novel mouse line, my first aim was to characterize the molecular composition of the brain vasculature by immunohistochemical, immunoblot (IB), reverse transcription quantitative real-time polymerase chain reaction (RT-qPCR), and quantitative mass spectrometry (MS) analysis.

My second aim was to explore a strategy to correct the oligomeric assembly and protease function of HTRA1-R274Q *in vivo*. For this, mice were infected with an adeno-associated virus (AAV) specifically targeting brain endothelial cells and encoding a protein-based corrector of HTRA1-R274Q recently developed by the laboratory of Martin Dichgans.

Third, heterozygous *HTRA1* mutations are an emerging cause of dominant late-onset cSVD, and several mutations, including R274Q, are speculated to display dominant-negative properties as opposed to, e.g., haploinsufficiency. I was thus in charge of investigating these possibilities *in vivo* by comparing the cerebrovasculature of *Htra1^{wt/R274Q}* and *Htra1^{+/-}* mice.

3 MATERIALS AND METHODS

3.1 Mice

All mouse-based experiments were performed in accordance with the German Animal Welfare Law and in compliance with the applicable regulations of the Government of Upper Bavaria. Animals were kept in the institute facility under standard conditions and had access to food and water *ad libitum*.

3.1.1 Mouse strains

3.1.1.1 *Htra1*^{R274Q} strain

Htra1^{R274Q} mice were generated via CRISPR (clustered regularly interspaced short palindromic repeats)/Cas9 (CRISPR associated protein 9) technology by B. Wefers (German Center for Neurodegenerative Diseases/Deutsches Zentrum für Neurodegenerative Erkrankungen (DZNE), München).

The CRISPR/Cas9 method allows the precise modification of DNA by either deleting (i.e., knockout) or inserting (i.e., knock-in) a fragment of interest. Briefly, the nuclease Cas9 is loaded with a complementary RNA fragment (guide RNA) that binds to the DNA region of interest and executes a targeted double-strand break. The cleaved DNA is then repaired either via non-homologous end joining (for knockout models) or via homology-directed repair and insertion of a DNA template (for knock-in models; Doudna et al., 2014).

To generate the *Htra1*^{R274Q} mouse line, C57BL/6 zygotes were microinjected with Cas9, guide RNA, and DNA templates, then implanted into a pseudopregnant female. Founder mice were identified via genotyping as described below.

The mutation was performed by replacing AGA encoding Arg with CAG encoding Gln. This results in a change in restriction profile, a feature used for genotyping purposes (see chapter 3.1.2.1). The presence of off targets at risk loci was excluded by sequencing.

Mice from the new mouse line were viable, fertile, and displayed no obvious phenotype.

3.1.1.2 *Htra1*^{ko} strain

Htra1^{ko} mice (fully backcrossed in a C57BL/6 background) were generated by gene trapping and have been described in previous reports (see Figure 3.2; Beaufort et al., 2014, Scharrer, 2015).

3.1.2 Genotyping

3.1.2.1 *Htra1*^{R274Q} mice

Extraction of genomic DNA. Genomic DNA was extracted from ear biopsies by incubation with 25 μ L of 50 mM NaOH at 97 °C for 30 min. Samples were neutralized by adding 30 μ L of 1 M Trizma® (TRIS base) hydrochloride, pH 7 (Sigma-Aldrich). After centrifugation, the DNA-containing supernatant was collected and stored at 4 °C.

DNA amplification. Amplification of the region of interest (i.e., around exon 4, encoding Arg274) was performed using primers located in 5' and 3' of exon 4:

- Forward primer: 5'-CACCTTTTCCCATTTTCTTGG-3'
- Reverse primer: 5'-CTACCCACTCACTTCAGAACCC-3'

PCR was performed using the reaction mix and programs described in Table 3.1 and Table 3.2.

3 μ L	10x KCl buffer (Fermentas)
2.4 μ L	25 mM MgCl ₂ (Fermentas)
1 μ L	10 mM dNTPs (GC-Healthcare)
1 μ L	10 μ M Primer mHtrA1 seq F (Metabion)
1 μ L	10 μ M Primer mHtrA1 seq R (Metabion)
20.8 μ L	ddH ₂ O
0.3 μ L	5 U/ μ L Taq-Polymerase (Fermentas)
0.5 μ L	Genomic DNA
Total: 30 μL	

Table 3.1 PCR mix used for genotyping

Step	Temperature	Duration	Cycles
Denaturation	95 °C	5 min	1
Denaturation	95 °C	30 s	35
Annealing	60 °C	30 s	
Elongation	72 °C	60 s	
Elongation	72 °C	10 min	1
Storage	40 °C	Infinite	1

Table 3.2 Cycling conditions used for genotyping

Analysis of PCR amplicons. The presence of the expected 550 base pairs (bp) amplicon was investigated on a 1–1.5% agarose gel prepared in tris-acetate EDTA (TAE) buffer (Roth) and containing 1:100 000 SYBR safe DNA gel stain (Invitrogen). Upon addition of DNA loading buffer (Invitrogen), electrophoresis was performed at 80 V for 60–90 min in Perfect

blue gel system devices (Peqlab) filled with TAE buffer. To evaluate the size of DNA fragments, 5 μ L of PeqGOLD Ladder Mix (Peqlab) was included in each run. DNA was visualized, and images were acquired on a UV table (Vilber-Lourmat).

Restriction analysis. The PCR amplicons were purified with a PCR purification kit (Roche), and DNA quantity was measured on a Nanodrop ND-1000 spectrophotometer (Peqlab). 250–500 ng DNA were treated with 10 units *Bsal*-HF enzyme or 25 units *PstI*-HF enzyme in a final volume of 15 μ L Cutsmart buffer for 4 h at 37 °C (all reagents from New England Biolabs).

The restriction profile was then evaluated on agarose gels as described before. As depicted in Figure 3.1, the *Htra1*^{wt} allele yields two 250–300 bp fragments upon digestion with *Bsal* but remains unaffected (i.e., 550 bp) upon treatment with *PstI*. In contrast, the *Htra1*^{R274Q} allele remains unaffected (i.e., 550 bp) upon treatment with *Bsal* but yields two 250–300 bp fragments upon digestion with *PstI*.



Figure 3.1 Sequence and restriction profile of *Htra1*^{wt} and *Htra1*^{R274Q} alleles

(A) AGA encoding Arg274 was replaced by CAG encoding Gln in *Htra1* exon 4. Arrows indicate restriction sites for the endonucleases *Bsal* and *PstI*. (B) Typical restriction profiles observed upon genotyping of *Htra1*^{wt}, *Htra1*^{wt/R274Q}, and *Htra1*^{R274Q} animals.

3.1.2.2 *Htra1*^{ko} mice

Mice were routinely genotyped as previously described (Beaufort et al., 2014, Scharrer, 2015), using ear biopsies to extract genomic DNA (see above) and the following primers:

- Forward primer wt and ko allele: 5'-AGGGTCTCAAGTATCCAGGTTG-3'
- Reverse primer wt allele: 5'-CCAGAAATAAGACTCGGACTCA-3'
(targeting DNA in 5' and 3' of the insertion site, respectively)
- Reverse primer ko allele: 5'-ATAAACCTCTTGCAGTTGCATC-3'
(targeting the 5' region of the gene-trap vector)

PCR mix and cycling conditions were similar to those depicted in Table 3.1 and Table 3.2. The denaturation time was increased to 2 min, the annealing was performed for 1 min at 65 °C, and the global reaction was restricted to 30 cycles. The resulting samples were analyzed on agarose gels as described above. While the wt allele yields a 434 bp product, the trapped allele yields a 281 bp product (Figure 3.2).

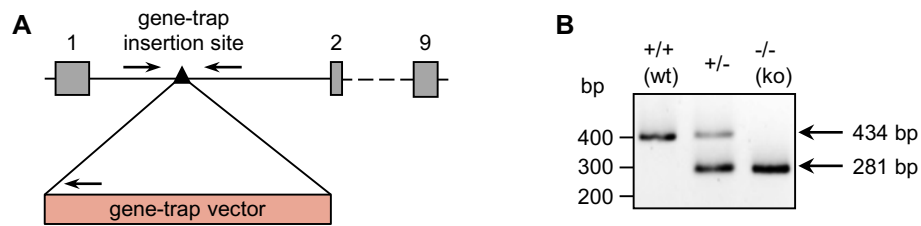


Figure 3.2 Genomic structure and genotyping of *Htra1*^{wt} and *Htra1*^{ko} alleles

(A) *Htra1* gene was interrupted by insertion of a gene-trap vector in the first intron. Grey boxes represent *Htra1* exons, and arrows locate the position of the forward and reverse primers used for genotyping. (B) Typical profiles observed upon genotyping of *Htra1*^{+/+} (wt), *Htra1*^{+/-}, and *Htra1*^{-/-} (ko) animals.

Figure adapted from Beaufort et al., 2014.

3.1.3 Viral infection

I used an AAV2 capsid variant that contains multiple copies of an endothelial cell-binding peptide. The virus was proven to drive the expression of a protein of interest efficiently and selectively in endothelial cells of the cerebral vasculature (Körbelin et al., 2016).

BR1-AAV2-eGFP has already been described (Körbelin et al., 2016). Control and rescue BR1-AAV2-HTRA1 were prepared by J. Körbelin (Institute of Experimental and Clinical Pharmacology and Toxicology, University of Lübeck). Both encode full-length mouse HTRA1 bearing a carboxyterminal V5-His-tag and either the control or the rescue mutation(s) (i.e., S328A and D174R-S328A, respectively) under the control of a CAG promoter.

Four-week-old animals were infected via tail vein injection of BR1-AAV2³ encoding HTRA1 or eGFP. Injection was performed using $7.5\text{--}9 \times 10^{10}$ (AAV-HTRA1) or $1.4\text{--}2.5 \times 10^{11}$ (AAV-eGFP) genomic particles per mouse, diluted in a final volume of 200 μL phosphate-buffered saline (PBS). Mice were kept in quarantine at least 3 days post-infection. No side effects were detected over the course of the experiment (i.e., up to 5 months).

3.1.4 Mouse sacrifice, organ and vessel retrieval

3.1.4.1 Sacrifice and perfusion

Mice were deeply anesthetized via intraperitoneal injection of ketamine (100 mg/kg) and xylazine (10 mg/kg) and transcardially perfused with 20 mL of PBS. Briefly, an abdominal cut was performed, and the thorax was opened to expose the heart. After a liver cut, a needle was placed in the heart's left ventricle, and perfusion was then performed manually using a 20 mL syringe. When required, PBS perfusion was followed by perfusion with 20 mL of 4% (w/v) paraformaldehyde (PFA; for IHC on paraffin or free-floating sections) or with 2 mL of 2% Evans blue (w/v) prepared in PBS (to visualize the vasculature for dissection).

³ License Az. 02-16-211, Government of Upper Bavaria.

3.1.4.2 Brain harvest

After decapitation, the skull was exposed via a neck-to-nose skin incision. Lateral cuts were performed on both sides of the cranium through the foramen magnum with scissors. Subsequently, scissors with closed blades were inserted into the anterior fontanelle with blades parallel to the body axis, twisted by 90 °, then opened to crack the skull open. The complete and intact brain was then extracted carefully.

For vessel isolation, protein and messenger RNA (mRNA) analysis, the brain was immediately frozen on dry ice and stored at -80 °C. For IHC analysis on paraffin or free-floating sections, tissue was post-fixed in 4% (w/v) PFA for 20–24 h at 4 °C. For vessel dissection, the brain was placed on ice in a Petri dish filled with PBS.

3.1.4.3 Dissection of cerebral vessels

Dissection was performed in PBS on ice under an M205 A dissection microscope (Leica), and pictures were taken with an MC170 HD camera (Leica). Upon Evans blue perfusion, the brain vasculature displayed a strong dark blue staining, as seen in Figure 4.16. The brain was first placed on the dorsal face, and, using micro scissors and micro dissecting forceps, the Circle of Willis (mostly comprising large leptomeningeal vessels) was collected and frozen on dry ice. Next, the remaining small leptomeningeal vessels were meticulously peeled off the brain's surface and collected on dry ice. After exclusion of the olfactory bulb and cerebellum, coronal sections were performed with a blade. Internal non-parenchymal vessels (i.e., at the level of the ventricles, see Figure 4.16) were peeled off, and the remaining leptomeningeal vessel-free brain was collected. Tissue was stored at -80 °C.

3.2 Tissue preparation

3.2.1 Isolation of cerebral vessels

All following steps were performed at 4 °C using frozen brain stem- and cerebellum-free brain as starting material to isolate the total brain vasculature. To isolate parenchymal vessels, leptomeningeal vessel-free brain was used. Brain was minced with a scalpel in a 10 cm Petri dish containing 1 mL Minimal Essential Media (MEM, Gibco®, Life Technologies), followed by homogenization with a Dounce tissue grinder (Wheaton) in 11 mL MEM in total. Myelin was separated from the sample by 5 min shaking and 20 min centrifugation at 6 000 xg in 30 mL of Ficoll solution (15% w/v, prepared in MEM). The sample was resuspended in 1.5 mL of 1% bovine serum albumin (BSA; w/v, diluted in PBS; Bio-Rad) and loaded on a 40 μm nylon mesh filter (Falcon). After washing with 240 mL PBS, cerebral vessels were washed out of the inverted filter with PBS. After centrifugation for 10 min at 3 000 xg , vessels were resuspended in 1 mL PBS using a BSA-coated tip, transferred to a

1.5 mL Eppendorf, centrifuged again for 5 min at 1 500 xg , and stored at -80°C until usage. For IHC analysis, 10 μL of vessel suspension were collected before the last centrifugation.

3.2.2 Tissue lysis for protein analysis

3.2.2.1 RIPA lysis

Brain tissue (half of the cerebellum) was homogenized using 500 μl of radio-immunoprecipitation assay (RIPA) lysis buffer (see Table 3.3) and a stainless steel metal bead with a diameter of 5 mm (Qiagen) for 3 min at 50 Hz in a TissueLyser LT bead mill (Qiagen). Samples were incubated for 30 min at 4°C followed by centrifugation at 15 000 xg for 20 min at 4°C to remove debris. The supernatant was collected and stored at -80°C until usage.

3.2.2.2 SDT lysis

Dissected vessels were homogenized in SDS-DTT-Tris/HCl (SDT) buffer (see Table 3.3; large leptomenigeal vessels: 100 μL , small leptomenigeal vessels: 75 μL , parenchymal vessels: 100 μL , cerebellum: 600 μL) with a 5 mm stainless steel metal bead in a Tissue-Lyser LT bead mill (Qiagen) for 3 min at 50 Hz, followed by centrifugation for 1 min at 11 000 xg and a second homogenization for 3 min at 50 Hz. Afterwards, samples were boiled for 10 min at 95°C , and the remaining debris was removed by centrifugation for 10 min at 11 000 xg . The supernatant was collected and stored at -20°C until usage.

Isolated vessels (see section 3.2.1) were lysed in 100 μL SDT buffer and homogenized with a Dounce tissue grinder, followed by centrifugation at 300 xg for 1 min. Homogenization and centrifugation steps were repeated, and the sample was boiled for 3 min at 95°C . Afterwards, samples were sonicated 5 times for 30 s at 4°C using a VialTweeter sonicator (Hielscher), then centrifuged at 16 000 xg for 5 min to remove remaining cell debris and insoluble material. The supernatant was collected and stored at -20°C until usage.

3.2.2.3 Protein concentration measurement

Protein concentration of RIPA-lysed samples was measured using the bichinonic acid (BCA) assay (Pierce BCA assay kit, Thermo Fisher Scientific). 10 μL of samples diluted in RIPA buffer and BSA (Bio-Rad) standards in the range of 0.0125–2 mg/mL were prepared in duplicates in a 96-well plate (Greiner Biotec). After adding 75 μL of BCA solution (ratio 50:1 of buffer A:B), plates were incubated at 37°C for 15 min. Colorimetric analysis was performed at 595 nm in a spectrophotometer (iMark microplate reader, Bio-Rad), and protein concentration of the samples was extrapolated from the BSA standard curve.

For SDT-lysed samples, the Pierce 660 nm Protein Assay kit (Thermo Fisher Scientific) was used. Samples and BSA standards were prepared in SDT buffer as described above. 75 μL of Protein Assay Reagent containing 5% (w/v) Ionic Detergent Compatibility Reagent (Ther-

mo Fisher Scientific) were added, and absorbance was measured immediately at 660 nm. Protein concentration was determined as described above.

RIPA lysis buffer	50 mM Tris/HCl 150 mM NaCl 1% Triton-X-100 1% Sodium deoxycholate 0.5% Sodium dodecyl sulfate (SDS) pH 7.2 (RIPA buffer was added with a cocktail of EDTA-free protease inhibitors (Roche) immediately before use)
SDT buffer	100 mM Tris/HCl 4% SDS (w/v) 0.1 M Dithiothreitol (DTT) pH 7.6

Table 3.3 Lysis buffers used for protein analysis

3.2.3 Tissue lysis for mRNA analysis and mRNA isolation

Brain tissue (half of the cerebellum) was homogenized with 1 mL QIAzol Lysis Reagent and a 5 mm stainless steel bead in a TissueLyser LT bead mill (all Qiagen) for 3 min at 50 Hz, followed by 2 min at 20 Hz and a 5 min incubation at room temperature. 200 μ L of chloroform were added to the lysate, which was then mixed and incubated for 2–3 min at room temperature.

mRNA isolation was performed as follows: Samples were lysed as described above and centrifuged at 12 000 xg for 15 min at 4 °C; the upper, aqueous phase containing RNA was collected. RNA extraction was performed using the RNeasy Lipid Tissue Mini Kit (Qiagen) according to the manufacturer's instructions. Briefly, samples were loaded on a small column containing an RNA binding silica membrane. After centrifugation and washing, DNA was eliminated by incubation with 80 μ L DNase I mix (0.39 U/ μ L, RNase-free DNase Set, Qiagen) for 15 min at room temperature. This step was followed by several centrifugations and washings, and RNA was finally eluted with RNase-free water. RNA concentration was measured in duplicates on a Nanodrop ND-1000 spectrophotometer (PepLab), and the samples were stored at -80 °C until usage.

3.3 Western blot (WB)

3.3.1 Sodium dodecyl sulfate polyacrylamide gel electrophoresis (SDS-PAGE)

The composition of the concentration and migration gel solutions is provided in Table 3.4. Polymerization was induced by adding 0.1% (w/v) ammonium persulfate (APS) and 0.1%

tetramethylethylenediamine (TEMED) before pouring the gels into a casting system (Bio-Rad). Samples (2–50 μg total protein) were added with Lämmli buffer and heated at 95 °C for 5 min for denaturation. Electrophoresis was performed in a Mini-Protean Tetra Cell apparatus (Bio-Rad) filled with electrophoresis buffer at 150 V for 60–90 min. To evaluate the molecular mass of the proteins, 5 μL Precision Plus Protein All Blue Standard (Bio-Rad) was included in each run.

Concentration gel	4% Polyacrylamide (Acrylamide stock: 30% (w/v) acrylamide and 0.8% N,N'-Methylenbisacrylamide (National Diagnostics)) 25 mM Tris-base 0.08% (w/v) SDS pH 6.8
Migration gel	7.5–12% Polyacrylamide (see above) 375 mM Tris-base 0.08% (w/v) SDS pH 8.8
Lämmli buffer (5x)	375 mM Tris-base 30% (v/v) Glycerol 6% (w/v) SDS 500 mM DTT 0.03% (w/v) Bromophenol blue pH 6.8
Protein electrophoresis buffer	25 mM Tris-base 192 mM Glycine 0.1% (w/v) SDS ddH ₂ O pH 8.3
Transfer buffer	25 mM Tris base 192 mM Glycine 20% (v/v) Methanol ddH ₂ O pH 8.3
Colloidal Coomassie solution	0.02% (w/v) Coomassie Brilliant Blue R (Sigma-Aldrich) 5% (w/v) Aluminum sulfate hydrate 2% (v/v) O-phosphoric acid 10% (v/v) Ethanol
TBS-T	10 mM Tris base 150 mM NaCl 0.2% (v/v) Tween 20 ddH ₂ O pH 8.0

Table 3.4 Composition of gel solutions and buffers used for protein analysis

3.3.2 Transfer and Coomassie staining

Proteins were transferred onto a 0.45 µm polyvinylidene fluoride (PVDF) membrane (Merck Millipore) using a Mini-Protean Tetra Cell apparatus (Bio-Rad) filled with transfer buffer at 100 V for 50 min at 4 °C. To visualize the global protein pattern, gels were stained with a colloidal Coomassie solution for 24 h on an orbital shaker and — after washings — scanned using the IrfanView software (IrfanView).

3.3.3 Immunoblot

Membranes were blocked in 4% (w/v) skim milk prepared in TBS-T for 15–30 min to prevent non-specific antibody (Ab) binding and then incubated in primary Ab solution prepared in TBS-T/milk for 1 h at room temperature up to overnight at 4 °C. A list of all primary Abs used for Western blotting, including working dilutions, is provided in Table 3.5. Following three 10 min washes in TBS-T, membranes were incubated with horseradish peroxidase (HRP)-coupled secondary antibody solution, prepared in TBS-T/milk for at least 1 h. A list of all HRP-coupled Abs used for Western blotting is provided in Table 3.6. After washes as described above, membranes were covered with the Western Chemiluminescent HRP Substrate (1:1 ratio of solution A:B; Merck Millipore). Luminescence was detected using the Fusion FX7 camera and analyzed using the Fusion software (both Vilber Lourmat). Signal quantification was performed with the ImageJ software (Fiji) using β -actin⁴ as a normalizer.

Antigen	Host	Company	Working dilution	Predicted molecular mass
α -Smooth muscle actin (SMA)	Mouse	Sigma-Aldrich	1:10 000	< 50 kD
β -Actin ⁴	Rabbit	Sigma-Aldrich	1:2 000	< 50 kD
Aquaporin 4 (AQP4)	Rabbit	Merck-Millipore	1:1 000	> 25 kD
Latent TGF- β binding protein 4 (LTBP4)	Goat	R&D Systems	1:1 000	250 kD
Microtubule-associated protein 2 (MAP2)	Goat	Santa Cruz Biotechnology	1:1 000	250 kD
V5	Mouse	Gibco-Invitrogen	1:1 000	> 50 kD
von Willebrand Factor (vWF)	Rabbit	Dako	1:1 000	250 kD

Table 3.5 Primary antibodies used for WB

⁴ Subsequently referred to as actin.

Antigen	Host	Company	Working dilution
Rabbit immunoglobulins	Goat	Dako	1:10 000
Goat immunoglobulins	Rabbit	Dako	1:10 000
Mouse immunoglobulins	Goat	Dako	1:10 000
Mouse IgG2a	Goat	Acris	1:10 000

Table 3.6 HRP-coupled antibodies used for WB

3.4 Mass spectrometry (MS) analysis

Label-free quantitative MS analysis was performed via liquid chromatography with tandem mass spectrometry (LC-MS/MS) by Andree Schmidt, PhD student in the laboratory of S. Lichtenthaler (DZNE München), according to a recently established protocol (Zellner et al., 2018). Briefly, 20 µg of vessel lysate, prepared as described above, were treated with Benzonase (Sigma-Aldrich) to hydrolyse DNA, then digested with trypsin. After desalting, 1.3 µg of peptides were separated on a nanoLC system (EASY-nLC 1000, Thermo Fisher Scientific) coupled to a Q-Exactive mass spectrometer (Thermo Fisher Scientific).

The data were analyzed with the Maxquant software and searched against a reviewed canonical FASTA database of *Mus musculus* (UniProt⁵) using standard setups: (i) two missed trypsin cleavages were allowed, (ii) oxidation of methionine and N-terminal acetylation were set as variable, carbamidomethylation of cysteine as static modifications, (iii) the false discovery rate (FDR) was set to < 1%, (iv) only unique peptides were used for quantification, (v) label-free quantification (LFQ) of proteins required at least 2 ratio counts of unique peptides.

I contributed analysis of the data as described below.

LFQ intensities were log₂-transformed. Relative quantification and statistical analysis (unpaired, two-sided Student's *t*-test) were performed for all proteins identified in at least 3 samples. A *p*-value < 0.05 and log₂ LFQ ratios > 0.4 and < -0.4 were set as significance thresholds. A permutation-based FDR estimation was performed using the software Perseus to account for multiple hypotheses (*p* = 5%; *s*₀ = 0.1).

For over-representation analysis, proteins were categorized based on the UniProt database⁵. For each protein category, the number of proteins upregulated in *Htra1*^{R274Q} vessels was normalized to the total number of proteins quantified in this category. ECM proteins are a subcategory of secreted proteins. Significance was assessed by Fisher's exact test and a *p*-value < 0.05 was set as significant.

⁵ URL: <https://www.uniprot.org/>

3.5 Reverse transcription quantitative real-time PCR (RT-qPCR)

3.5.1 cDNA synthesis

Complementary DNA (cDNA) was generated via reverse transcription with the Omniscript Reverse Transcription kit (Qiagen) according to the manufacturer's instructions. 0.5–1 µg RNA was added to a mix of 1 µM Oligo-dT Primer (5'-TTTTTTTTTTTTTTT-3', Metabion), 0.5 mM dNTP Mix, and 4 units reverse transcriptase in reaction buffer and RNase free water in a total volume of 20 µL. Samples were then incubated for 1 h at 37 °C. Reverse transcriptase- and mRNA-free samples served as controls. cDNA was stored at -20 °C until usage.

3.5.2 Quantitative real-time PCR (qPCR)

Primers were designed using the Universal Probe Library Probe Finder (Roche) or the CLC Workbench and were produced by Metabion. Primers were selected to span exons to avoid amplification of genomic DNA that might contaminate samples. A primer list is provided in Table 3.7.

Target	Sequence
Actin	Forward primer: 5'-GGATGCAGAAGGAGATTACTGC-3' Reverse primer: 5'-CCACCGATCCACACAGAGTA-3'
AAV-HTRA1 (V5-tagged)	Forward primer: 5'-CGTAGAATCGAGACCGAGGAG-3' Reverse primer: 5'-CCTGAACATGGTTGTCCGCA-3'

Table 3.7 Sequences of the primers used for qPCR

qPCR was conducted in a non-transparent white 384-well plate sealed with adhesive foil. Each well contained 125–250 nM of each forward and reverse primer and 6 µL of Brilliant II SYBR Green MasterMix (Agilent Technologies) in DNA and RNase free water in a final volume of 10 µL. Two µL of cDNA samples diluted 1:10 (v/v) in DNA- and RNase-free water were added. Samples were loaded in triplicates, and reverse transcriptase- and mRNA-free samples were included as negative controls.

Runs were performed on a Roche LightCycler 480 II operated with the corresponding LightCycler 480 software (both Roche Diagnostics) using the following protocol:

Step	Temperature	Duration	Cycles	Analysis mode
Denaturation	95 °C	10 min	1	None
Amplification	95 °C	15–30 s	40	Quantification Acquisition mode: Single at 60 °C
	60 °C	1 min		
Melting curve	95 °C	Continuous (5 acquisitions per °C)	1	Melting curve
Cooling	40 °C	Infinite	1	None

Table 3.8 Cycling conditions used for qPCR

3.5.3 Data analysis

Samples that displayed multi-peak dissociation curves (i.e., corresponding to the amplification of multiple species), high C_p values (i.e., over 35, corresponding to very low abundance), or high C_p value deviation between triplicates ($SD > 0.5$) were excluded from the analysis. Actin was used for normalization, and cDNA was quantified using the following formulas:

$$\Delta C_p = C_p(\text{Species of interest}) - C_p(\text{Normalizer})$$

$$\text{Relative quantity} = 2^{-\Delta C_p}$$

3.6 Histology and immunohistochemistry

3.6.1 Isolated vessels

A small 0.5 x 0.5 cm square was drawn with a PAP pen (Sigma-Aldrich) on a Superfrost slide (Thermo Fisher Scientific). Isolated brain vessels (prepared as described above) were spread on the slide and left for drying at room temperature. Tissue was fixed in 4% (w/v) PFA for 20 min at room temperature followed by permeabilization and blocking in 5% (w/v) BSA (Sigma-Aldrich) prepared in PBS-T (PBS with 0.1% (v/v) Triton X-100) for 1 h at room temperature (75 μ L per section). Samples were incubated with primary Ab solutions (see Table 3.9) diluted in PBS-T/BSA overnight at 4 °C (40 μ L per section). Following three 5 min washes in PBS, vessels were incubated for 1 h at room temperature with the fluorophore-coupled secondary Ab solutions (see Table 3.10) diluted in PBS and containing 1.25 μ g/mL 4',6-diamidino-2-phenylindole (DAPI, Invitrogen) to achieve nuclear staining (40 μ L per section). After another three 5 min washes in PBS, slides were mounted with glass coverslips using Fluoromount Aqueous Mounting Medium (Sigma-Aldrich). After drying for 2 h at room temperature, slides were kept at 4 °C.

Antigen	Host	Company	Working dilution
CD31	Rat	Acris	1:100
Type IV collagen (Col IV)	Goat	Southern Biotech	1:200
Fibronectin (FN)	Rabbit	Abcam	1:200
Laminin (Lam)	Rabbit	Dako	1:200
LTBP4	Goat	R&D Systems	1:100
SMA (Cy3-coupled Ab)	Mouse	Sigma-Aldrich	1:250

Table 3.9 Primary antibodies used for IHC

Antigen	Host	Fluorophore	Company	Working dilution
Rabbit immunoglobulins	Donkey	Cy3 (red)	Jackson	1:200
Goat immunoglobulins	Donkey	Alexa Fluor 488 (green)	Abcam	1:200
Goat immunoglobulins	Donkey	Cy3 (red)	Jackson	1:200

Table 3.10 Secondary antibodies used for IHC

3.6.2 Paraffin sections

3.6.2.1 Paraffin embedding and sectioning

Before embedding, PFA-fixed brains (one hemisphere) were washed for 1 h in flowing water. Paraffin embedding was achieved using the Microm STP 120 embedding machine (Thermo Fisher Scientific) with the following running cycle:

Reagent	Time
70% Ethanol	1 h
80% Ethanol	1 h
90% Ethanol	1 h
96% Ethanol	1 h
96% Ethanol	1 h
100% Ethanol	1 h
100% Ethanol	1 h
Acetone	0.5 h
Acetone	0.5 h
Rothistol (Xylol)	1 h
Paraffin I	2 h
Paraffin II	2 h

Table 3.11 Running cycle used for paraffin embedding

Paraffin blocks were prepared and let solidify on a cooling plate using a HistoStar (Thermo Fisher Scientific). Serial 7 μm sagittal sections were prepared on a Microm HM 340E microtome (Thermo Fisher Scientific) and were placed on SuperFrost slides (Thermo Fisher Scientific) in warm (52 °C) water.

3.6.2.2 Deparaffinization

Deparaffinization was achieved by bathing the sections in the following solutions for the indicated time periods:

Reagent	Time
Rothistol (Xylol) I	5 min
Rothistol (Xylol) II	5 min
100% Ethanol	2 min
96% Ethanol	2 min
70% Ethanol	2 min

Table 3.12 Solutions used for deparaffinization

3.6.2.3 Antigen retrieval and IHC stainings

After a 5 min wash in PBS, single sections were circled with a PAP pen, and antigens were retrieved by incubation with Proteinase K (20 $\mu\text{g}/\text{mL}$ in PBS, 100 μL per section) for 10 min

followed by another 5 min wash in PBS. Ab-based immunofluorescent stainings were performed exactly as described above.

3.6.3 Free-floating sections

After PFA fixation, brains were stored in PBS at 4 °C. One hemisphere was embedded in 2.5% agarose prepared in PBS. Sectioning of 100 µm sagittal sections was performed on a VT1200S Vibratome (Leica) with the following setups: speed 0.8 mm/s, amplitude 0.8 mm.

All blocking, washing, and staining steps were performed in a 24-well plate under constant shaking. Permeabilization/blocking was achieved using PBS-T/BSA for 1–2 h at room temperature (0.5 mL per well). Sections were incubated with Ab solutions (250 µL per well) and mounted as described above. Washings with PBS (0.5 mL per well) included 3 sequential 10 min steps.

3.7 Microscopy and signal quantification

3.7.1 Fluorescence microscopy

For the analysis of thin paraffin sections, signals were observed and acquired on an Axio Observer.Z1 Fluorescence Microscope using the Zen user interface (both Zeiss). For quantitative comparisons, pictures of samples stained in parallel were acquired using identical setups (i.e., magnification, laser intensity, exposure time).

Signal quantification was performed using the software ImageJ (Fiji). Vessel selection was performed manually using a vessel-specific counterstaining (Col IV or laminin). The area of the region of interest was measured, and the mean pixel intensity was determined for each fluorescent signal.

3.7.2 Confocal laser scanning microscopy

For the analysis of thick free-floating sections, confocal laser scanning microscopy was conducted on a Zeiss Observer.Z1 microscope equipped with an LSM 330 Laser and an LSM T-PMT camera using the Zen user interface (all Zeiss).

3.8 Statistics

Statistical analysis was performed using two-sided unpaired *t*-test and Fisher's exact test as appropriate and indicated in the figure legends using Excel (Microsoft) and GraphPad Prism 6 (GraphPad Software Inc). A *p*-value ≤ 0.05 was considered significant. Graphs were prepared in Excel and GraphPad Prism 6.

4 RESULTS

4.1 Molecular phenotype of *Htra1*^{R274Q} brain vessels

While *Htra1*^{ko} mice display remarkable alterations of the cerebrovascular proteome (Zellner et al., 2018), they do not exhibit gross phenotypic abnormalities related to, e.g., fertility, viability, or survival. Specifically, vascular and/or cerebral dysfunction typically associated with cSVD (i.e., blood-brain barrier (BBB) disruption, altered vasoreactivity, astrogliosis, white matter lesions) have not been reported in this animal model (Ikawati et al., 2018, Scharrer, 2015, Zellner et al., 2018, ISD München, unpublished observations). My work, therefore, focused on the molecular characterization of the brain vasculature of *Htra1*^{R274Q} mice.

4.1.1 Fibronectin is upregulated in *Htra1*^{R274Q} brain vessels

As previously stated, a hallmark of the vasculopathy in HTRA1-related familial cSVD is a fibrotic degeneration of the vascular wall with accumulation of FN (see chapter 1.2.1.4; Hara et al., 2009). Moreover, FN is an established substrate of HTRA1 (Grau et al., 2006). Therefore, this protein was chosen for initial analysis.

Sagittal paraffin brain sections from 6-month-old *Htra1*^{wt} mice were immunohistochemically stained to determine the normal expression pattern of FN in the mouse brain vasculature. Col IV, a matrix protein broadly expressed in vascular basement membranes, and SMA, mostly expressed by arterial SMCs, served as control.

As illustrated in Figure 4.1, FN signal was the strongest in leptomeningeal arteries and arterioles (i.e., vessels at the dorsal and ventral surface of the brain). In contrast, it was much fainter or even absent in veins and parenchymal vessels.

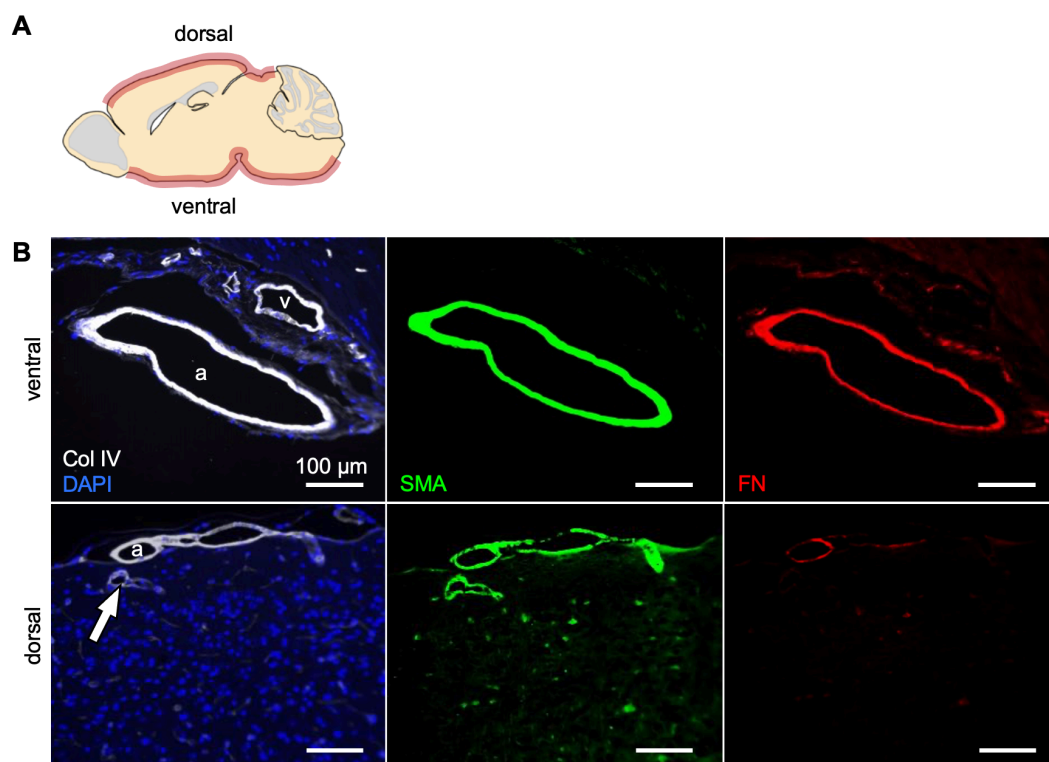


Figure 4.1 Fibronectin is predominantly expressed in leptomeningeal arteries and arterioles

(A) Scheme of a mouse brain sagittal section indicating the location of dorsal and ventral leptomeningeal arteries. (B) Representative immunofluorescent stainings; (a) leptomeningeal artery/arteriole, (v) leptomeningeal venule; the white arrow marks a parenchymal vessel.

To compare FN expression in *Htra1^{wt}* and *Htra1^{R274Q}* leptomeningeal arteries and arterioles, I proceeded as follows: I determined the vessel wall area based on Col IV immunoreactivity and measured both FN and Col IV signal intensity within this area (Figure 4.2, A and B). Over 50 vessels per genotype (Figure 4.2, B, upper panels) were analyzed in sections derived from 4–5 mice per group (Figure 4.2, B, lower panels).

This assessment revealed a distinct enrichment of FN in leptomeningeal vessels from *Htra1^{R274Q}* compared to *Htra1^{wt}* mice. Conversely, Col IV signal was comparable in both groups. Accordingly, the FN/Col IV signal intensity ratio was elevated in *Htra1^{R274Q}* vessels. Of note, as shown in Figure 4.2, C, FN signal intensity was markedly enhanced at the luminal side of the vessels, suggesting subendothelial accumulation.

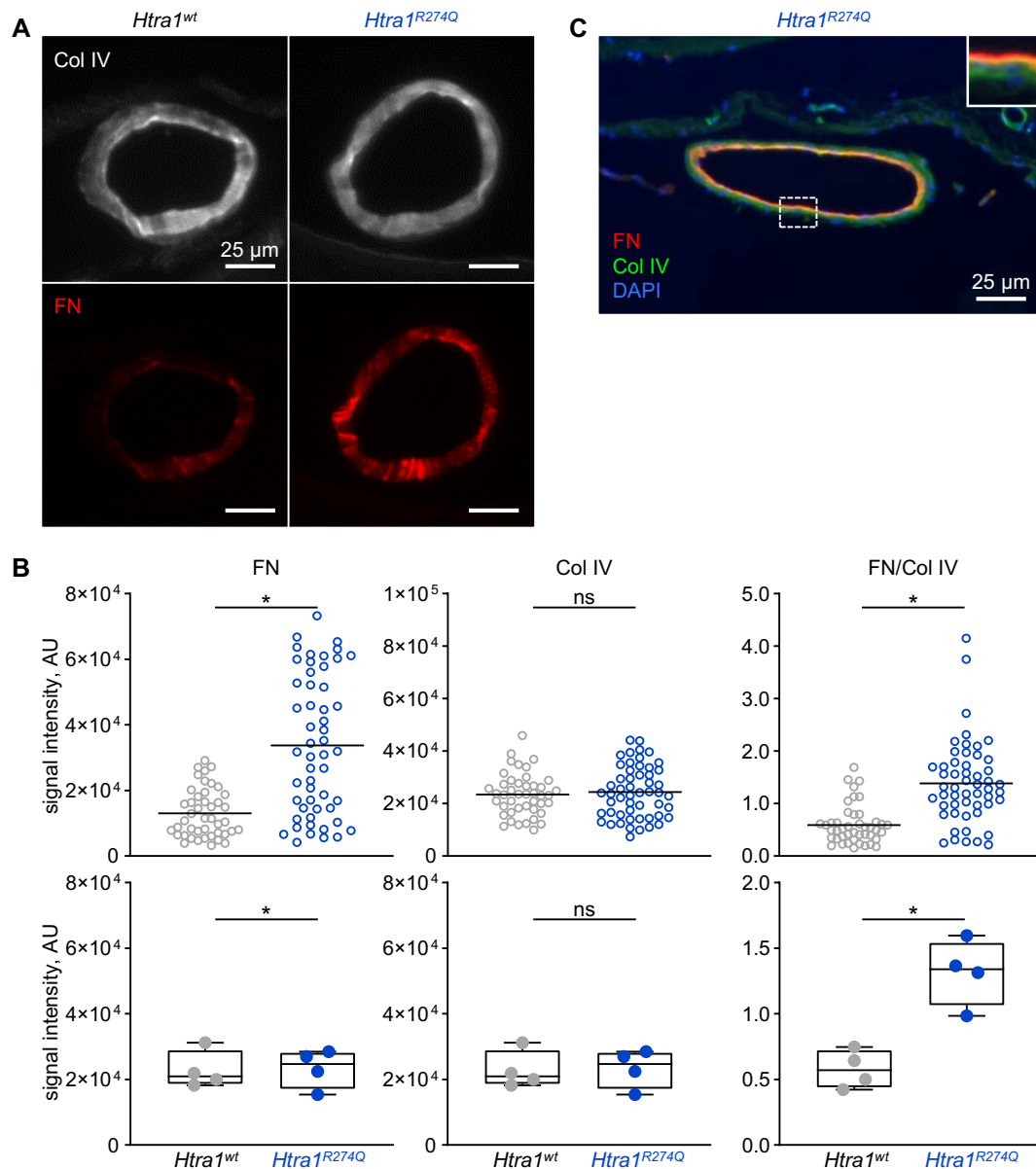


Figure 4.2 Fibronectin is upregulated in leptomeningeal arteries and arterioles of 6-month-old *Htra1^{R274Q}* mice

(A) Representative FN and Col IV stainings of *Htra1^{wt}* and *Htra1^{R274Q}* leptomeningeal arteries. (B) Quantification of fluorescence signal intensity (AU). Upper panels: Scatter plots (black bars: mean) with empty circles. Data points represent individual vessels ($n > 50$ vessels, 4 mice/genotype); significance was tested by two-sided unpaired *t*-test. Lower panels: box-and-whisker plots (median, minimum, maximum) with filled circles. Data points represent individual mice; significance was tested by two-sided unpaired *t*-test. (C) Co-staining of FN and Col IV in a ventral *Htra1^{R274Q}* leptomeningeal artery.

To evaluate the impact of aging on FN expression and accumulation, I further compared brain tissue from 1-, 6-, and 12-month-old animals (Figure 4.3). In *Htra1^{wt}* brain vessels, the expression of both FN and Col IV was progressively reduced over the life span. The age-dependent reduction of FN was impaired in *Htra1^{R274Q}* leptomeningeal vessels, while that of Col IV remained unchanged.

FN upregulation in *Htra1*^{R274Q} compared to *Htra1*^{wt} vessels was detected at 1 month and was enhanced with aging. As 6 months appeared as an early time point to detect marked genotype-dependent changes, it was chosen for further analysis.

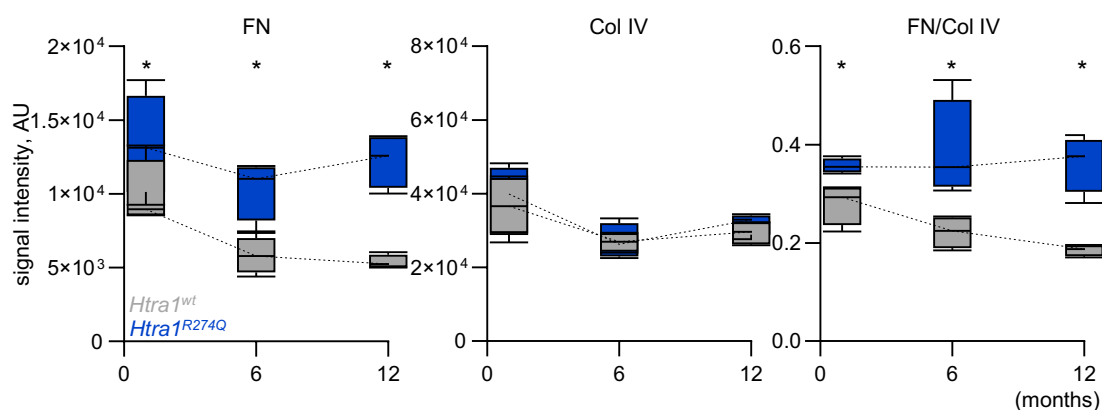


Figure 4.3 The age-dependent reduction of FN expression is impaired in *Htra1*^{R274Q} leptomeningeal vessels

The cerebrovascular expression of FN and Col IV was evaluated in 1-, 6-, and 12-month-old mice by IHC. Signal intensity (AU) was quantified as in Figure 4.2. Four animals/age/genotype were analyzed. Data are depicted as box-and-whisker plots (median, minimum, maximum), and significance was tested by two-sided unpaired *t*-test.

Together, my observations indicate that *Htra1*^{R274Q} mice display molecular abnormalities that — at least in part — reproduce those observed in the vasculature of human *HTRA1* mutation carriers (see chapter 1.2.1.4).

4.1.2 *Htra1*^{R274Q} brain vessels exhibit reduced HTRA1 protein levels along with an upregulation of ECM proteins

To determine the broader consequences of HTRA1-R274Q on the vascular proteome and obtain robust readouts for the rescue assay (section 4.2), I set up to perform quantitative MS analysis of isolated brain vessels, as recently described by Zellner et al., 2018.

4.1.2.1 Validation of a mouse brain vessel isolation procedure

In order to isolate brain vessels, I used the following procedure (Figure 4.4, A): I first minced and homogenized brain tissue, followed by myelin removal via Ficoll gradient centrifugation. I then filtered the resulting sample on a 40 μm mesh to positively select vessels and vessel networks. The mesh was finally inverted and washed to elute the vessels, which were either spread on slides for IHC imaging or collected for MS and IB analysis.

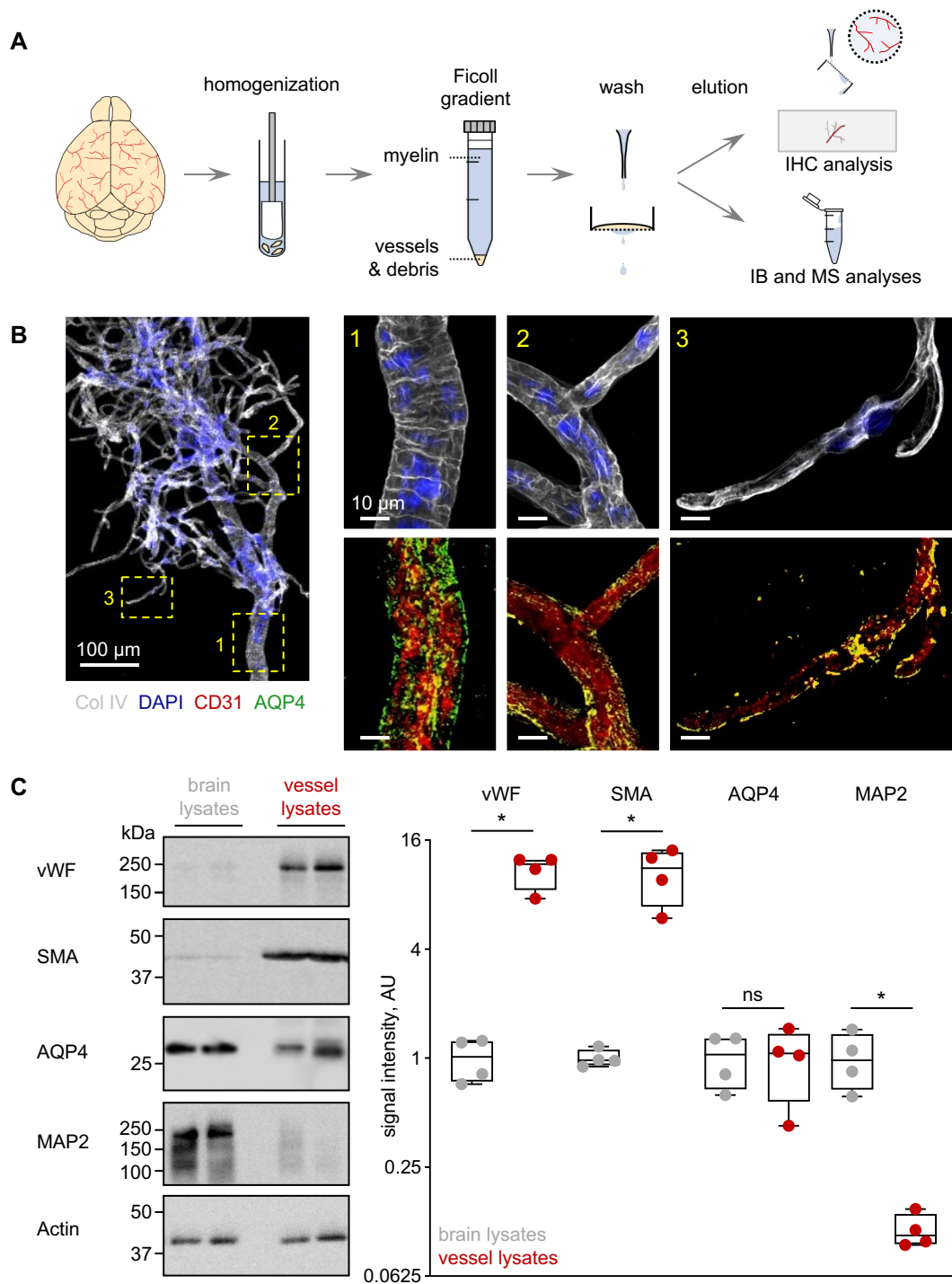


Figure 4.4 Validation of a mouse brain vessel isolation protocol

(A) Scheme of the brain vessel isolation protocol. (B) Representative IHC images of a vascular segment retrieved from the vessel isolation protocol with close-up view of selected vascular branches. (C) Brain tissue or isolated vessels were lysed, followed by IB analysis with the indicated antibodies. Right panel: Signal quantification (AU; \log_2 scale). Actin was used as a normalizer; the mean signal intensity in brain lysates was set to 1. Data are depicted as box-and-whisker plots (median, minimum, maximum) with filled circles. Data points represent individual mice ($n = 4/\text{sample type}$). Significance was tested by two-sided unpaired t -test.

(B, C) Type IV collagen (Col IV) is a vascular basement membrane marker; CD31 and von Willebrand factor (vWF) are endothelial cell markers; α -smooth muscle actin (SMA) is a mural cell marker; aquaporin IV (AQP4) is an astrocyte end-feet marker; microtubule-associated protein 2 (MAP2) is a neuronal marker; DAPI labels nuclei; β -actin, which is ubiquitously expressed, is used as a normalizer.

On IHC examination (Figure 4.4, B), samples typically consisted of branched vascular segments, including vessels from < 10 to > 50 μm diameter, thus corresponding to capillaries and arteries, respectively. Nuclear staining with DAPI showed no cells aside from the vessel segments, highlighting the purity of the samples. Staining for CD31 (a marker for endothelial cells), Col IV (a marker for vascular basement membrane), and SMA (a marker for mural cells, not illustrated) confirmed the presence of all major vascular cell types. Aquaporin 4 (AQP4, a marker for astrocyte end-feet) was also detected but displayed a patchy expression pattern. This suggests that the astrocytes, which form an integral part of the neuro-glio-vascular unit (Iadecola, 2017), were torn off at their end-feet as a “predetermined breaking point” through the isolation protocol.

In an independent assay, brain vessel lysates (typically containing 50–100 μg total protein per sample) were analyzed by IB, using actin for normalization (Figure 4.4, C). In accord with IHC data, analysis of independent vessel and brain preparations revealed a consistent and strong (> 10 -fold) enrichment of both von Willebrand Factor (vWF, a marker for endothelial cells) and SMA in vessel compared to brain lysates, whereas AQP4 was co-purified. In contrast, the neuronal marker microtubule-associated protein 2 (MAP2) was markedly depleted (> 8 -fold) in vessel samples.

Together, my findings validate the reproducible isolation of pure mouse brain vessel preparations.

4.1.2.2 MS analysis of *Htra1*^{wt} and *Htra1*^{R274Q} brain vessels

Label-free quantitative MS was performed on vessel preparations derived from 5 animals per genotype. Following lysis, samples were prepared and analyzed by Andree Schmidt, PhD student in the laboratory of S. Lichtenthaler (DZNE München) as described in section 3.4. I contributed MS data analysis.

In total, $> 5\,000$ proteins were identified by ≥ 2 unique peptides (Figure 4.5, A). 3 474 proteins were detected in ≥ 3 samples per genotype and were quantified. 126 proteins were found to be significantly deregulated in *Htra1*^{R274Q} vs. *Htra1*^{wt} vessels (both p -value < 0.05 and \log_2 LFQ ratio ≤ -0.4 or ≥ 0.4 , corresponding to a fold change of ≤ -0.24 or ≥ 0.31 , respectively). Among the proteins with altered abundance, 92 were down- and 34 upregulated.

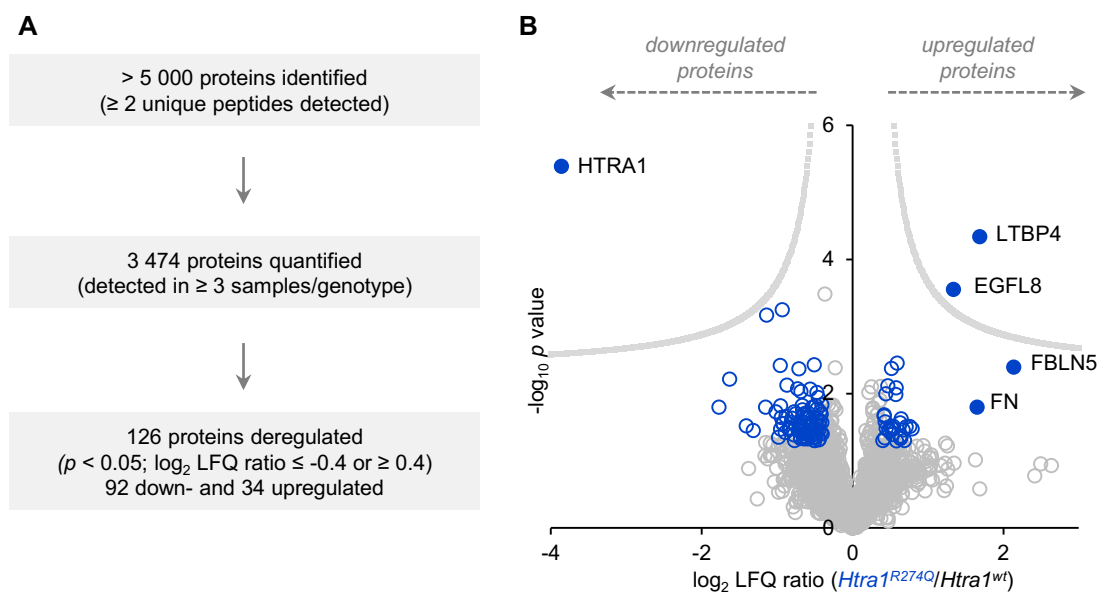


Figure 4.5 Overview of the proteomic analysis of *Htra1*^{wt} and *Htra1*^{R274Q} brain vessels

(A) Summary of the LC-MS/MS and label-free quantification results. (B) Volcano plot of all proteins quantified by MS. Blue circles: deregulated proteins; filled circles: proteins considered as being the most relevant; hyperbolic curve: permutation-based FDR estimation.

The most notable genotype-dependent change was a > 14-fold decrease of HTRA1 protein levels in *Htra1*^{R274Q} brain vessels (Figure 4.5, B and Figure 4.6, A). As mRNA retrieval from isolated brain vessels exhibited very low yield, I measured HTRA1 mRNA levels in brain tissue. Contrasting with the strong reduction of HTRA1 protein levels, HTRA1 mRNA levels were comparable in *Htra1*^{wt} and *Htra1*^{R274Q} brains (Figure 4.6, B).

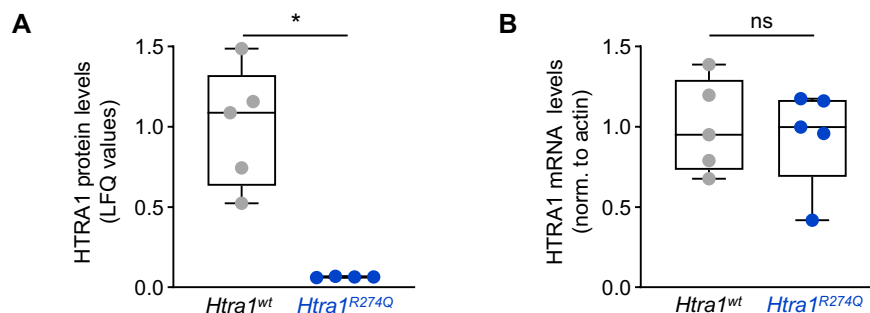


Figure 4.6 Mutation R274Q leads to a distinct reduction of HTRA1 protein levels while leaving mRNA levels unchanged

(A) HTRA1 protein levels in *Htra1*^{wt} and *Htra1*^{R274Q} brain vessels were determined by MS. (B) HTRA1 mRNA levels in *Htra1*^{wt} and *Htra1*^{R274Q} brain tissue were determined by RT-qPCR using actin as a housekeeping gene. Box-and-whisker plots (median, minimum, maximum) with filled circles; The mean signal intensity in *Htra1*^{wt} samples was set to 1; data points represent individual mice ($n = 5$ /genotype). Significance was tested by two-sided unpaired *t*-test.

In accord with IHC analysis (Figure 4.2), FN was among the most enriched proteins in *Htra1*^{R274Q} vessels (Figure 4.5, B; > 3-fold, $p < 5 \times 10^{-2}$). Three other proteins also exhibited a marked (> 3-fold) enrichment: latent TGF- β binding protein 4 (LTBP4), FBLN5 (a known HTRA1 substrate) and epidermal growth factor-like protein 8 (EGFL8). The accumulation of LTBP4 and EGFL8 was still significant after FDR correction (Figure 4.5, B).

To further examine the proteins deregulated in *Htra1*^{R274Q} vs. *Htra1*^{wt} vessels, I analyzed their subcellular location based on the UniProt database⁵. I found that among the proteins upregulated in *Htra1*^{R274Q} vessels, secreted and ECM proteins were markedly overrepresented (Figure 4.7, A; secreted proteins: > 4-fold, $p < 5 \times 10^{-5}$; ECM proteins: > 10-fold, $p < 5 \times 10^{-4}$). This is similar to the enrichment of secreted and ECM proteins recently reported in brain vessels of > 20-month-old *Htra1*^{ko} mice (Zellner et al., 2018). In fact, the cerebrovascular proteome changes in *Htra1*^{R274Q} mice resemble those observed in *Htra1*^{ko} animals (Figure 4.7, B), but fewer proteins accumulate and to a lesser extent in *Htra1*^{R274Q} vessels.

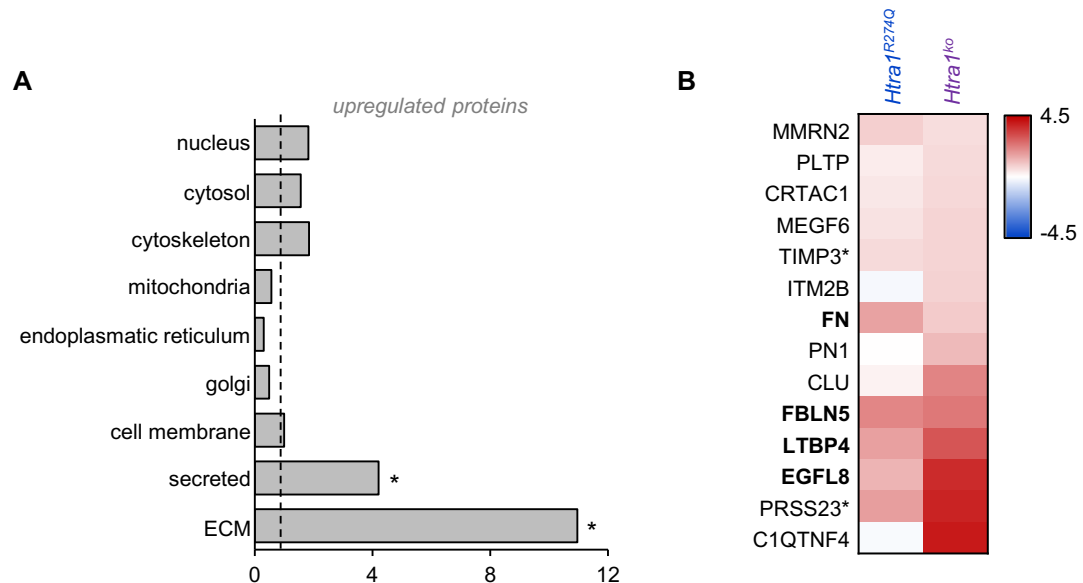


Figure 4.7 Secreted and ECM proteins accumulate in *Htra1*^{R274Q} brain vessels

(A) Subcellular location of the proteins enriched in *Htra1*^{R274Q} compared to *Htra1*^{wt} vessels. Proteins were categorized based on the UniProt database⁵. For each protein category, the number of proteins upregulated in *Htra1*^{R274Q} vessels was normalized to the total number of proteins quantified in this category. ECM proteins are a subcategory of secreted proteins. Significance was tested by Fisher's exact test. (B) Log₂ LFQ ratio-based heatmap of protein deregulation in *Htra1*^{R274Q} and *Htra1*^{ko} brain vessels. Secreted or ECM proteins upregulated in *Htra1*^{ko} vessels (dataset from Zellner et al.) and detected in *Htra1*^{R274Q} (my original data set) are depicted. FN, FBLN5, LTBP4 and EGFL8 are in bold letters.

*TIMP3 and PRSS23 were detected in < 3 samples/genotype in the *Htra1*^{R274Q} vs. *Htra1*^{wt} dataset.

(C1QTNF4: complement C1q tumor necrosis factor-related protein 4, PRSS23: serine protease 23, CLU: clusterin, PN1: protease nexin 1, ITM2B: integral membrane protein 2B, TIMP3: metalloproteinase inhibitor 3, MEGF6: multiple epidermal growth factor-like domains protein 6, CRTAC1: cartilage acidic protein 1, PLTP: phospholipid transfer protein, MMRN2: multimerin 2)

4.1.2.3 Validation of LTBP4 upregulation via IB and IHC analysis

Since LTBP4 was one of the most enriched proteins in *Htra1*^{R274Q} vessels in MS analysis (> 3-fold, $p < 5 \times 10^{-5}$; Figure 4.8, A), I further examined the expression of this remarkable candidate by IB and IHC. For this, I used a selective anti-LTBP4 Ab shown to react with control but not with *Ltbp4*^{ko} mouse tissue (Bultmann-Mellin et al., 2015).

IB analysis of *Htra1*^{wt} brain vessels revealed a smear of > 150 kDa bands (Figure 4.8, B; Bultmann-Mellin et al., 2015). In accord with MS data (Figure 4.8, A), LTBP4 was markedly enhanced (2.9-fold) in the brain vasculature of *Htra1*^{R274Q} mice (Figure 4.8, B).

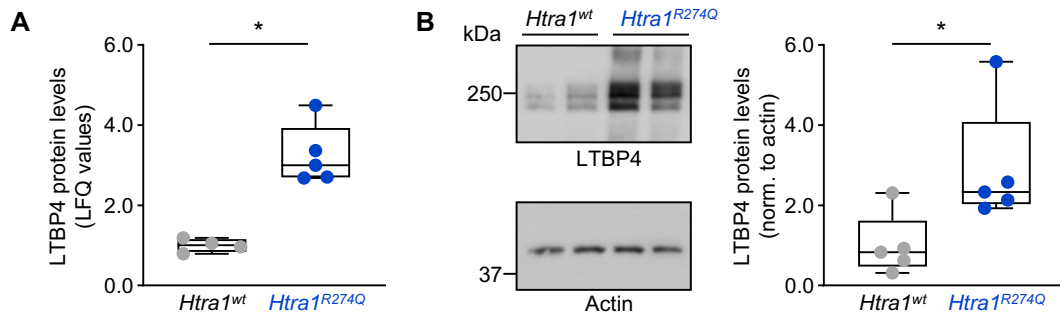


Figure 4.8 IB analysis confirms LTBP4 accumulation in *Htra1^{R274Q}* brain vessels

LTBP4 was detected by MS (A) and IB (B) in mouse brain vessels. (B) Representative IB of *Htra1^{wt}* and *Htra1^{R274Q}* vessel lysates (left) and IB signal quantification (right). Box-and-whisker plots (median, minimum, maximum) with filled circles. The mean signal intensity in *Htra1^{wt}* samples was set to 1; data points represent individual mice ($n = 5$ mice/genotype); significance was tested by two-sided unpaired *t*-test.

IHC analysis of LTBP4 expression was performed as described for FN (chapter 4.1.1), except that laminin (Lam) staining was used instead of Col IV staining to determine the vessel wall area (Figure 4.9, A), as the LTBP4 and Col IV Abs used for my experimental work were both goat-derived.

The expression pattern of LTBP4 in control brain resembled that of FN. LTBP4 was strongly expressed in the vascular wall of leptomeningeal arteries and arterioles (Figure 4.9, A). Parenchymal vessels exhibited a much lower LTBP4 signal intensity (not illustrated), while veins were negative (not illustrated).

Comparison of *Htra1^{wt}* and *Htra1^{R274Q}* leptomeningeal vessels revealed that both LTBP4 signal intensity and LTBP4/laminin ratios were elevated in *Htra1^{R274Q}* vessels, while laminin signal intensity was similar within the two groups (Figure 4.9, A–B).

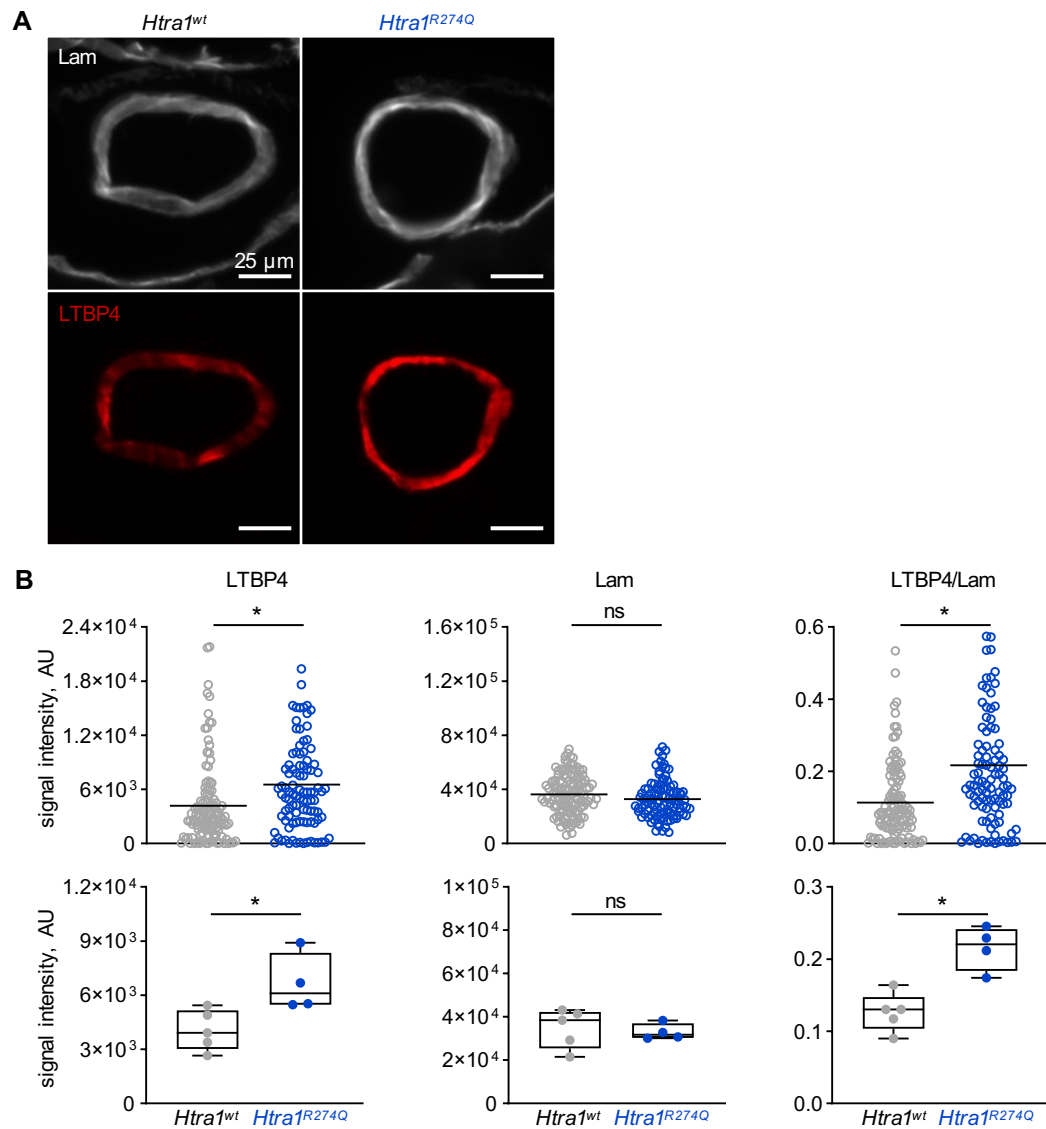


Figure 4.9 LTBP4 is upregulated in leptomeningeal arteries and arterioles of *Htra1*^{R274Q} mice

(A) Representative LTBP4 and laminin stainings of *Htra1*^{wt} and *Htra1*^{R274Q} leptomeningeal arteries. (B) Quantification of fluorescence signal intensity (AU). Upper panels: scatter plots (black bars: mean) with empty circles. Data points represent individual vessels ($n > 50$ vessels, 4–5 mice/genotype); significance was tested by two-sided unpaired *t*-test. Lower panels: box-and-whisker plots (median, minimum, maximum) with filled circles. Data points represent individual mice ($n = 4$ –5 mice/genotype); significance was tested by two-sided unpaired *t*-test.

In conclusion, both IB and IHC confirmed the enrichment of LTBP4 in the brain vasculature of *Htra1*^{R274Q} mice. Together with IHC analysis of FN expression, these two methods thus represent alternatives to MS for, e.g., initial evaluation of the functional correction assay (chapter 4.2) or the analysis of dominant-negative effects (chapter 4.4).

4.2 Functional correction of HTRA1-R274Q *in vivo* using an AAV-based approach

4.2.1 Experimental design of the rescue assay

The laboratory of Martin Dichgans demonstrated that the inactive HTRA1 variant HTRA1-D174R-S328A promotes trimer formation and restores the proteolytic activity of HTRA1-R274Q *in vitro* (see chapter 1.3.5). Thus, I set up to challenge this protein repair strategy *in vivo*.

The laboratory of J. Körbelin (Institute of Experimental and Clinical Pharmacology and Toxicology, University of Lübeck) recently developed an AAV variant (BR1-AAV2) that specifically infects brain endothelial cells with a high and long-term (i.e., up to 22 months) transduction efficiency (Körbelin et al., 2016). Since HTRA1 is a secreted protein, I speculated that following AAV-driven endothelial expression, the corrector HTRA1 variant would distribute within the whole vascular wall. Specifically, it should be expressed in the subendothelial ECM, which I had identified as a specific site for FN accumulation in *Htra1*^{R274Q} leptomeningeal arteries. Hence, the BR1-AAV2-based approach was chosen to deliver the rescue protein to the cerebrovasculature of *Htra1*^{R274Q} mice.

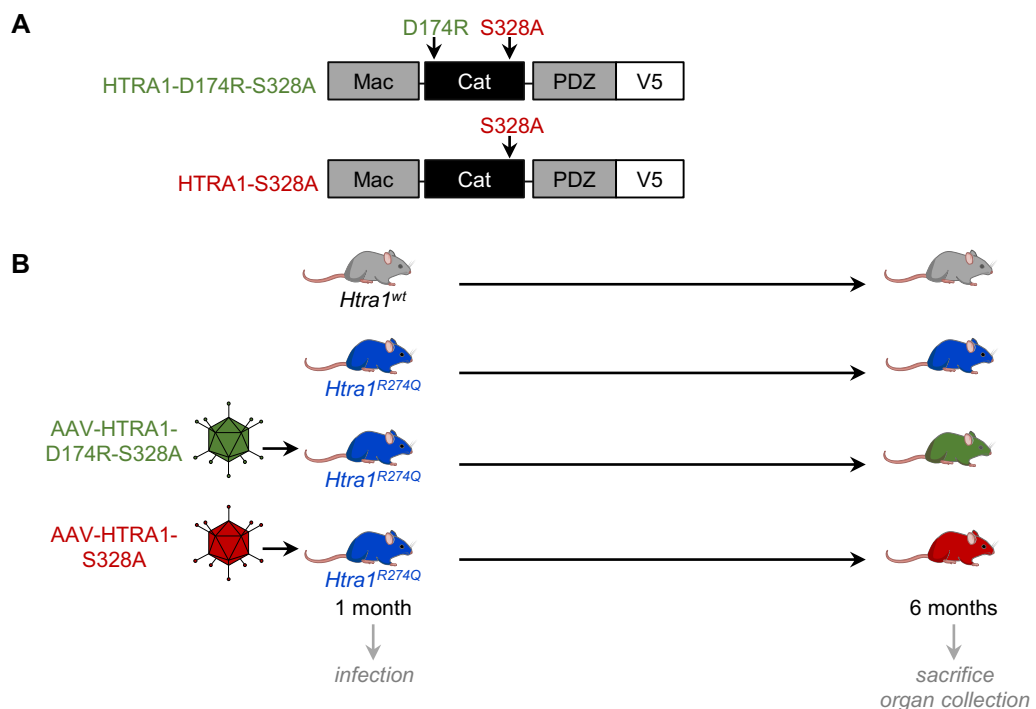


Figure 4.10 Experimental design of the rescue assay

(A) The rescue HTRA1 variant (green) displays a corrector mutation (D174R) and an active site mutation (S328A). The active site mutant (red) served as control. Both proteins are proteolytically inactive and display a carboxyterminal V5 tag. (B) BR1-AAV2s encoding rescue or control HTRA1 were injected into 1-month-old *Htra1*^{R274Q} mice. Animals were sacrificed at 6 months (i.e., 5 months post-infection). Naïve 6-month-old *Htra1*^{wt} and *Htra1*^{R274Q} mice served as controls.

Two viruses were generated. Both encode full-length mouse HTRA1 bearing a V5-His tag, either the rescue mutant (AAV-HTRA1-D174R-S328A) or a control inactive mutant (AAV-HTRA1-S328A) (Figure 4.10, A). Prior to the start of my experimental work, the laboratory of Martin Dichgans observed that HTRA1-D174R-S328A and HTRA1-S328A were both expressed in brain vessels 1 month post-infection (pi, not illustrated).

For the rescue assay, 1-month-old *Htra1*^{R274Q} mice were infected with the rescue or control virus via tail vein injection and were sacrificed 5 months post-infection (Figure 4.10, B). Age-matched naïve *Htra1*^{wt} and *Htra1*^{R274Q} mice served as control.

4.2.2 AAV-HTRA1 is expressed in mouse brain vessels 5 months post-infection

I first investigated the long-term expression of AAV-HTRA1 by V5-selective RT-qPCR and IB analyses of brain lysates. Samples from animals sacrificed 1 month pi were used as a positive control, samples from naïve animals as a negative control (Figure 4.11, A). Both methods revealed a heterogeneous expression of AAV-HTRA1 5 months pi. Half of the animals showed high expression levels of AAV-HTRA1, similar to expression levels observed 1 month pi, while others exhibited low to very low expression levels.

IB analysis of vessel lysates further confirmed the vascular expression of AAV-HTRA1 (Figure 4.11, B). Conversely, IHC analysis of brain sections or isolated vessels failed to detect V5-related signal (not depicted).

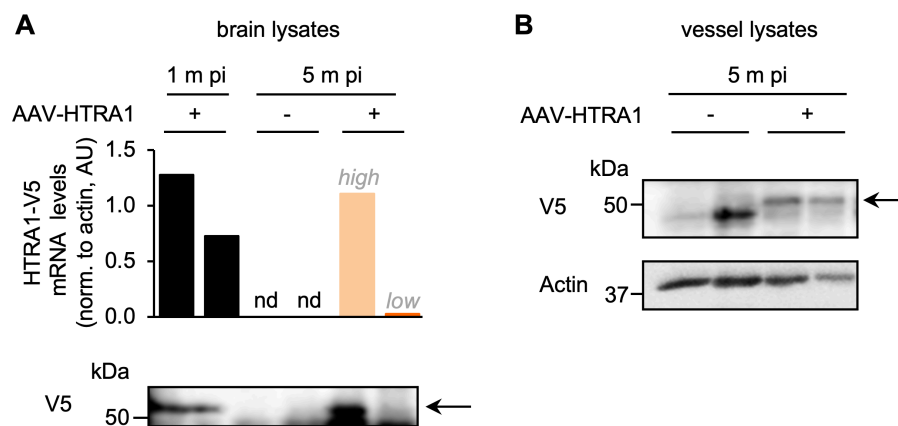


Figure 4.11 AAV-HTRA1 is expressed in the brain vasculature of *Htra1*^{R274Q} animals 5 months post-infection

(A) AAV-HTRA1 mRNA (upper panel) and protein (lower panel) levels were analyzed by V5-selective RT-qPCR and IB in brain lysates of mice 1 or 5 months pi (+). Tissue from naïve mice (-) served as control. Representative samples are depicted. RT-qPCR: The mean mRNA abundance 1 month pi was set to 1. Light orange: AAV-HTRA1 high expressor; bright orange: AAV-HTRA1 low expressor. IB: AAV-HTRA1 is marked by an arrow. (B) AAV-HTRA1 was detected by anti-V5 IB in isolated vessel lysates of mice 5 months pi. Actin was used as a normalizer. AAV-HTRA1 is marked by an arrow.

4.2.3 Infection with AAV-HTRA1-D174R-S328A does not alleviate FN and LTBP4 accumulation in leptomeningeal arteries of *Htra1*^{R274Q} mice

As initial readouts for the rescue assay, I examined the expression of FN and LTBP4 in leptomeningeal arteries by IHC as described in section 4.1.1.

As shown in Figure 4.12 (left), analysis of FN expression indicated that neither the control nor the rescue virus altered the aberrant deposition of FN in leptomeningeal arteries of *Htra1*^{R274Q} mice. In particular, FN levels were comparable in vessels from AAV-HTRA1-S328A- and AAV-HTRA1-D174R-S328A-infected mice.

IHC analysis of LTBP4 expression further revealed that *Htra1*^{R274Q} leptomeningeal vessels from infected mice exhibited LTBP4 levels comparable to those detected in the vasculature of naïve *Htra1*^{R274Q} animals (Figure 4.12, right).

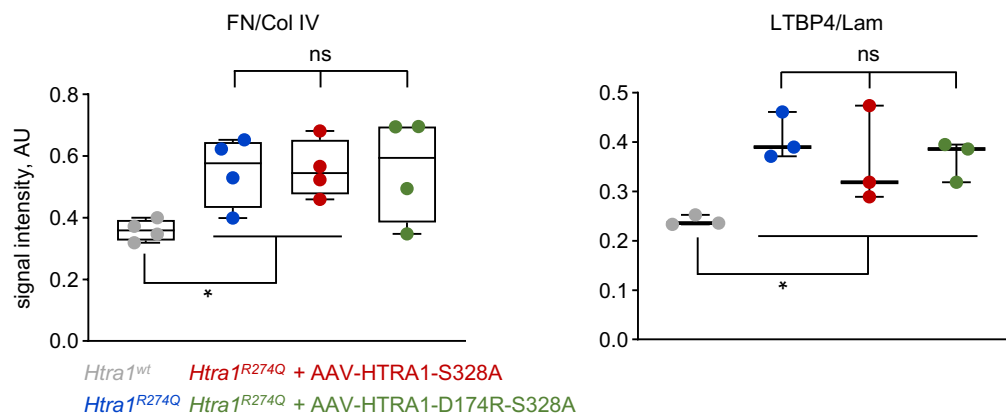


Figure 4.12 AAV-HTRA1-D174R-S328A does not alter the enrichment of FN and LTBP4 in leptomeningeal arteries of *Htra1*^{R274Q} mice

IHC analysis of FN and LTBP4 expression in leptomeningeal vessels of naïve and infected *Htra1*^{R274Q} mice was performed as in Figure 4.2 and Figure 4.9. FN/Col IV and LTBP4/Lam ratios are depicted as box-and-whisker plots (AU, median, minimum, maximum) with filled circles. Data points represent individual mice ($n = 3-4/\text{genotype}$), significance was tested by two-sided unpaired *t*-test.

Together, these observations indicate that AAV-HTRA1-D174R-S328A does not alleviate FN and LTBP4 accumulation in leptomeningeal arteries of *Htra1*^{R274Q} mice. However, (i) since paraformaldehyde fixation precludes mRNA analysis, the expression of AAV-HTRA1 could not be evaluated in the brain tissue used for IHC analysis, (ii) FN and LTBP4 expression in leptomeningeal arteries might not reflect the behavior of these two proteins in the whole brain vasculature, (iii) more generally, FN and LTBP4 expression levels might not reflect the overall alterations of the cerebrovascular proteome and (iv), the tropism of BR1-AAV2 for leptomeningeal compared to parenchymal brain vessels had not been evaluated.

4.2.4 BR1-AAV2 efficiently infects parenchymal but not leptomeningeal brain vessels

As AAV-HTRA1-V5 was not detected by IHC, I used a BR1-AAV2-eGFP virus to evaluate the tropism of the virus for the parenchymal and leptomeningeal brain vasculature.

Four-week-old mice were infected and sacrificed 4 weeks pi. Free-floating brain sections were prepared. Col IV staining (used to visualize brain vessels) and eGFP signal were examined by confocal microscopy.

In accord with previous reports (Körbelin et al., 2016), eGFP was detected in most parenchymal capillaries, indicating efficient transduction (Figure 4.13, left). However, eGFP signal appeared inversely correlated with the vessel size. Positive cells were less frequent in parenchymal arterioles and were even absent from penetrating and leptomeningeal arteries (Figure 4.13, middle and right). Thus, BR1-AAV2 is not an appropriate vector to deliver HTRA1 to the leptomeningeal vasculature.

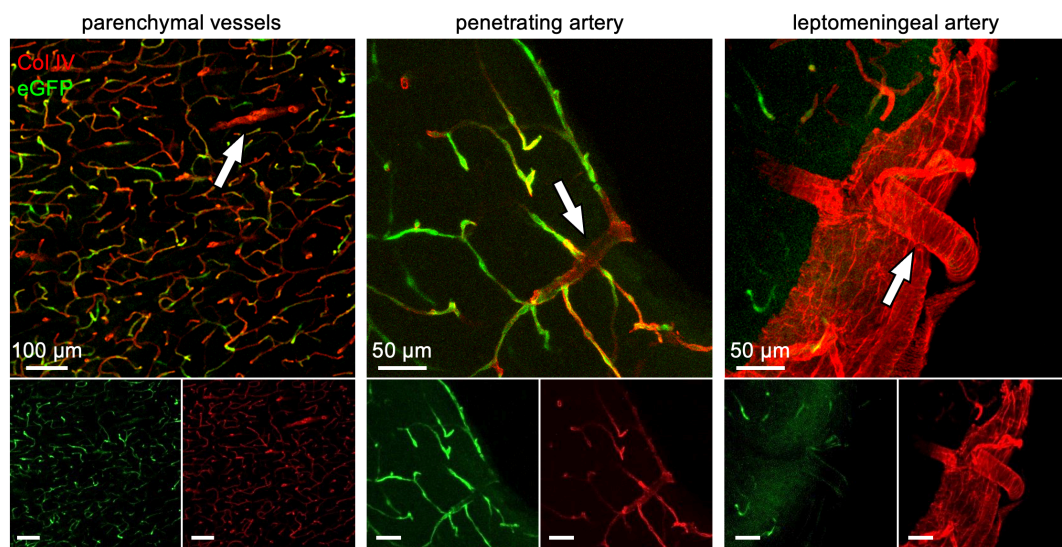


Figure 4.13 AAV-eGFP is efficiently expressed in parenchymal but not leptomeningeal vessels

Brain sections from mice infected with BR1-AAV2-eGFP. eGFP fluorescence was evaluated in brain vessels using Col IV staining as a positive control. Representative images are depicted. Arrows mark arterioles and arteries.

4.2.5 Infection with AAV-HTRA1-D174R-S328A does not alleviate proteome alterations in *Htra1*^{R274Q} brain vessels

Next, I evaluated the consequences of AAV-HTRA1 expression on the proteome of isolated brain vessels. As described in section 4.1.2.1, these consist of vascular segments that include capillaries, arterioles, and arteries (see section 4.1.2.1).

AAV-HTRA1 expression 5 months pi was found to be heterogeneous across infected mice (section 4.2.2). Hence, as an initial step, I analyzed brain tissue of infected mice by V5-selective RT-qPCR and IB to identify high AAV-HTRA1 expressors. A group of mice infected

with the control or the rescue virus displaying comparable AAV-HTRA1 levels (5 animals each) was selected for further analysis (Figure 4.14).

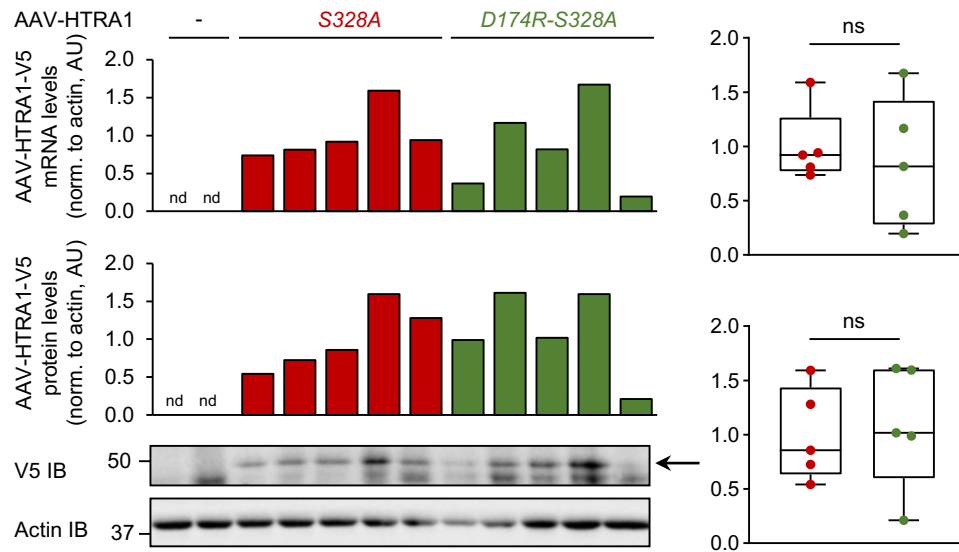


Figure 4.14 Selection of samples exhibiting high AAV-HTRA1-V5 expression levels

AAV-HTRA1-V5 protein and mRNA levels were determined in brain lysates of mice 5 months pi as described in Figure 4.11. Left panels: levels detected in individual samples; the signal detected in AAV-HTRA1-S328A samples was set to 1. IB: AAV-HTRA1 is marked by an arrow. Right panels: box-and-whisker plots (median, minimum, maximum) with filled circles. Data points represent individual mice ($n = 5$ mice/genotype); the signal detected in AAV-HTRA1-S328A samples was set to 1. Significance was tested by two-sided unpaired *t*-test.

I next isolated and lysed brain vessels from the corresponding mice, followed by LTBP4 IB (Figure 4.15, A). I found LTBP4 expression to be elevated in the vasculature of both naïve and infected *Htra1*^{R274Q} mice. Specifically, LTBP4 levels were comparable in vessels expressing the control and the rescue HTRA1 variants.

To investigate the overall consequences of AAV-HTRA1 expression on the cerebrovascular proteome, MS analysis was performed. As shown in Figure 4.15, B and D, the expression levels of the key proteins deregulated in *Htra1*^{R274Q} vessels were not normalized in vessels infected with the rescue virus.

Focusing first on HTRA1, I searched for but did not identify any AAV-HTRA1 specific peptides, i.e., that would contain Gln274, Arg174, Ala328 or match with the V5-sequence (not illustrated). Moreover, HTRA1 levels in infected *Htra1*^{R274Q} vessels were as low as those detected in naïve *Htra1*^{R274Q} vessels (Figure 4.15, C). Keeping in mind that isolated vessels contain astrocytes, which are the main cell type producing HTRA1 in the brain vasculature (see chapter 1.3.1), I propose that when evaluating pan-HTRA1 levels, endothelial-specific expression of AAV-HTRA1 might be covered by the high astrocyte-derived HTRA1 signal.

In accord with IB, LTBP4 was enriched in naïve and infected *Htra1*^{R274Q} samples and exhibited comparable levels in all three experimental conditions (i.e., *Htra1*^{R274Q} vessels, either naïve or infected with the control or rescue virus). Similarly, infection failed to normalize FN, FBLN5, and EGFL8 levels (Figure 4.15, D).

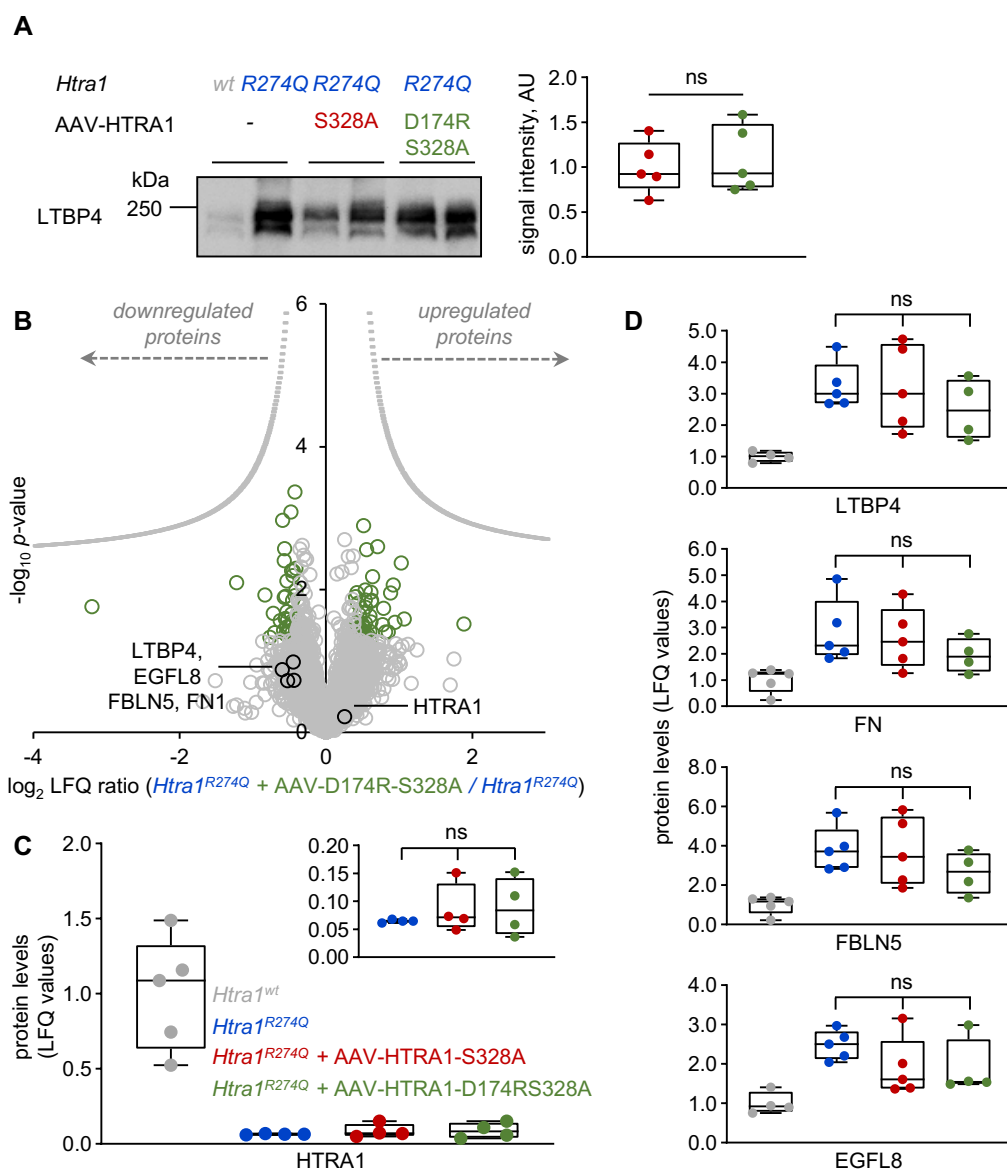


Figure 4.15 AAV-HTRA1-D174R-S328A does not alleviate the accumulation of ECM proteins in *Htra1*^{R274Q} brain vessels

(A) LTBP4 was detected by IB in brain vessels of *Htra1*^{R274Q} + AAV-S328A and *Htra1*^{R274Q} + AAV-D174R-S328A vessel lysates. *Htra1*^{wt} samples served as negative, naïve *Htra1*^{R274Q} samples as positive controls. Left: representative image. Right: Signal quantification. Box-and-whisker plots (median, minimum, maximum) with filled circles. The mean signal intensity in *Htra1*^{R274Q} + AAV-S328A samples was set to 1; data points represent individual mice ($n = 5/\text{genotype}$); significance was tested by two-sided unpaired *t*-test. (B) Volcano plot of proteins quantified in *Htra1*^{R274Q} and *Htra1*^{R274Q} + AAV-D174R-S328A brain vessels. Proteins are labeled by protein name. Green circles: deregulated proteins; black circles: proteins of interest; hyperbolic curve: permutation-based FDR estimation. (C) HTRA1, (D) LTBP4, FN, FBLN5, and EGFL8 abundance was determined by MS in mouse brain vessels. Box-and-whisker plots (median, minimum, maximum) with filled circles. The mean signal intensity in *Htra1*^{wt} samples was set to 1; data points represent individual mice ($n = 4\text{--}5/\text{genotype}$). Significance was tested by two-sided unpaired *t*-test. (C) Inlet: Magnification of the y-axis. (D) Colors are as in panel C.

Collectively, my data demonstrate that AAV-driven endothelial expression of a rescue HTRA1 variant does not normalize the proteome of *Htra1*^{R274Q} brain vessels. Moreover, I could show that while BR1-AAV2 efficiently transduces parenchymal capillaries, it does not target arterioles and arteries — in particular leptomeningeal ones.

4.3 Proteome changes in *Htra1*^{R274Q} vessels are mostly restricted to leptomeningeal brain vessels

The data presented in chapter 4.1 demonstrate that FN and LTBP4 are enriched in leptomeningeal *Htra1*^{R274Q} vessels as well as in the overall cerebrovascular proteome. However, the status of these two proteins in the parenchymal vasculature remained unclear. In addition, the expression pattern of the other proteins deregulated in *Htra1*^{R274Q} vessels across distinct vascular segments had not been examined. Hence, I set up to selectively analyze protein expression levels in parenchymal compared to leptomeningeal brain vessels.

4.3.1 Development of a protocol for anatomically defined and size-dependent fractionation of the brain vasculature

To fractionate the brain vasculature based on the anatomical position and size of the vascular segments, I proceeded as follows (Figure 4.16): First, mice were perfused with Evans blue to visualize the brain vasculature. Next, ventral leptomeningeal vessels (including the Circle of Willis) were dissected and collected, resulting in a fraction enriched in large (> 50 µm) leptomeningeal vessels. Afterwards, the remaining pia and arachnoid mater enriched in small (< 25 µm) leptomeningeal vessels was peeled off and collected from the ventral and dorsal faces of the brain. Upon removal of the olfactory bulb and cerebellum, coronal cuts were performed. The choroid plexus and remaining large non-parenchymal vessels were discarded. The resulting leptomeningeal vessel-free tissue was finally used to isolate parenchymal vessels.

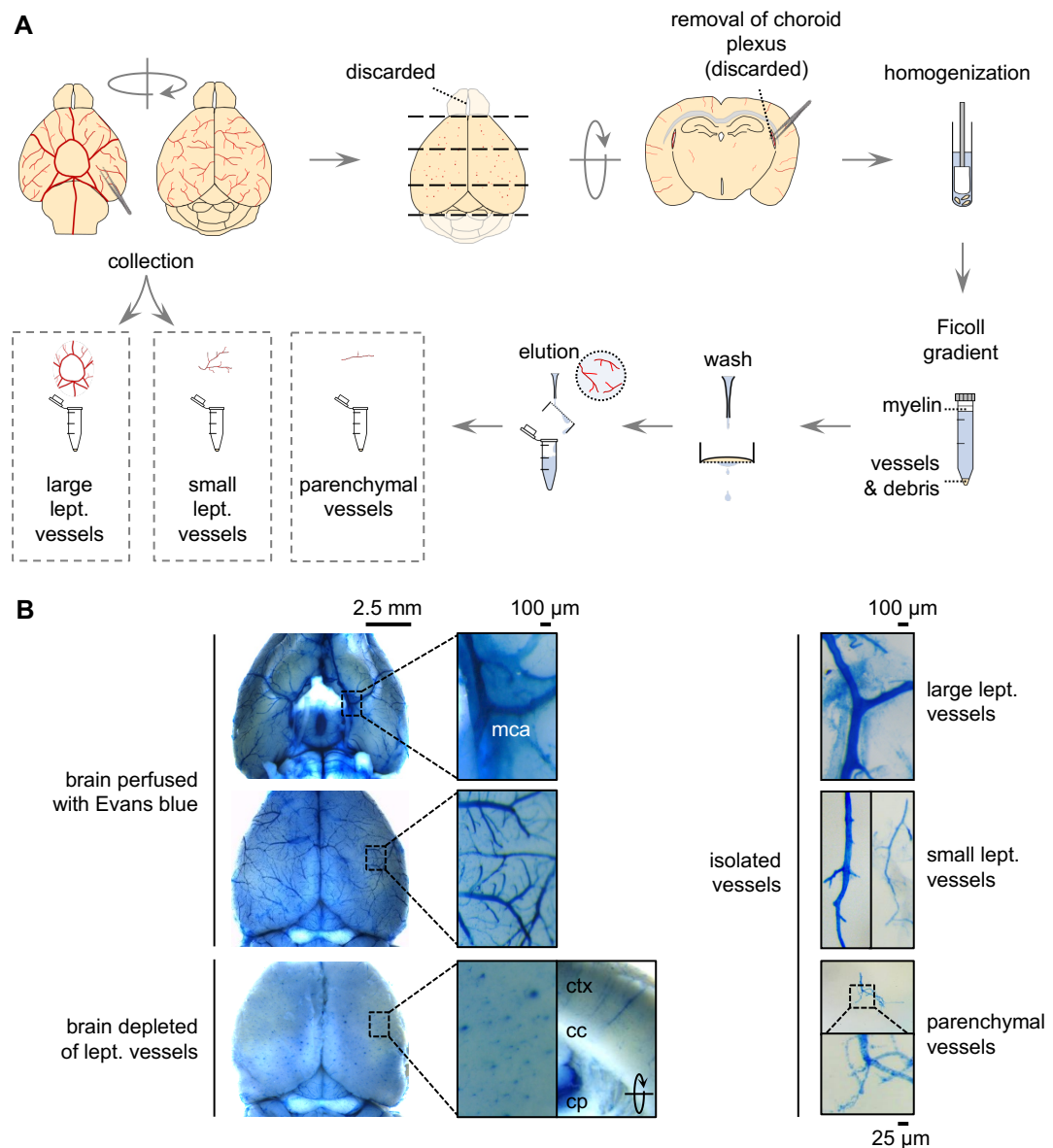


Figure 4.16 Anatomically defined and size-dependent fractionation of the brain vasculature

(A) Scheme of the vessel preparation protocol. (B) Representative images of an Evans blue perfused mouse brain across the different dissection steps (left) and of vascular segments retrieved from the vessel isolation protocol (right).

(lept.: leptomenigeal, mca: middle cerebral artery, ctx: cortex, cc: corpus callosum, cp: choroid plexus)

4.3.2 LTBP4, FN, FBLN5, and EGFL8 are predominantly expressed in the leptomenigeal vasculature — their site of accumulation in *Htra1*^{R274Q} brain vessels

In a pilot experiment, I analyzed parenchymal, small leptomenigeal, and large leptomenigeal vessels, pooling the vasculature from 3 *Htra1*^{wt} or *Htra1*^{R274Q} animals. Total brain vessels served as control.

LTBP4 IB analysis indicated that depletion of the leptomenigeal vasculature drastically reduces LTBP4 levels (Figure 4.17, A, compare total to parenchymal vessels), demonstrat-

ing that, in accord with my IHC data, LTBP4 is predominantly expressed in the leptomeningeal vasculature.

Moreover, a comparison of *Htra1*^{wt} and *Htra1*^{R274Q} vessels confirmed LTBP4 accumulation in both small and large leptomeningeal arteries. Conversely, LTBP4 levels were comparable in *Htra1*^{wt} and *Htra1*^{R274Q} parenchymal vessels, suggesting that the accumulation of LTBP4 in *Htra1*^{R274Q} vessels is mainly restricted to the leptomeningeal vasculature (Figure 4.17, A).

These observations were confirmed by MS analysis of the vascular proteome. Similar to LTBP4, FN, FBLN5, and EGFL8 levels were strongly reduced in parenchymal compared to total brain vessel preparations. Moreover, all four proteins were enriched in small and large *Htra1*^{R274Q} leptomeningeal vessels. Conversely, LTBP4, FN, and FBLN5 abundance were comparable in *Htra1*^{wt} and *Htra1*^{R274Q} parenchymal vessels, while EGFL8 was not detected (Figure 4.17, B).

In sharp contrast with these expression patterns, HTRA1 was detected to similar levels in total, parenchymal, and leptomeningeal *Htra1*^{wt} vessels. Moreover, its expression level was strongly reduced in all *Htra1*^{R274Q} vessel types (Figure 4.17, C).

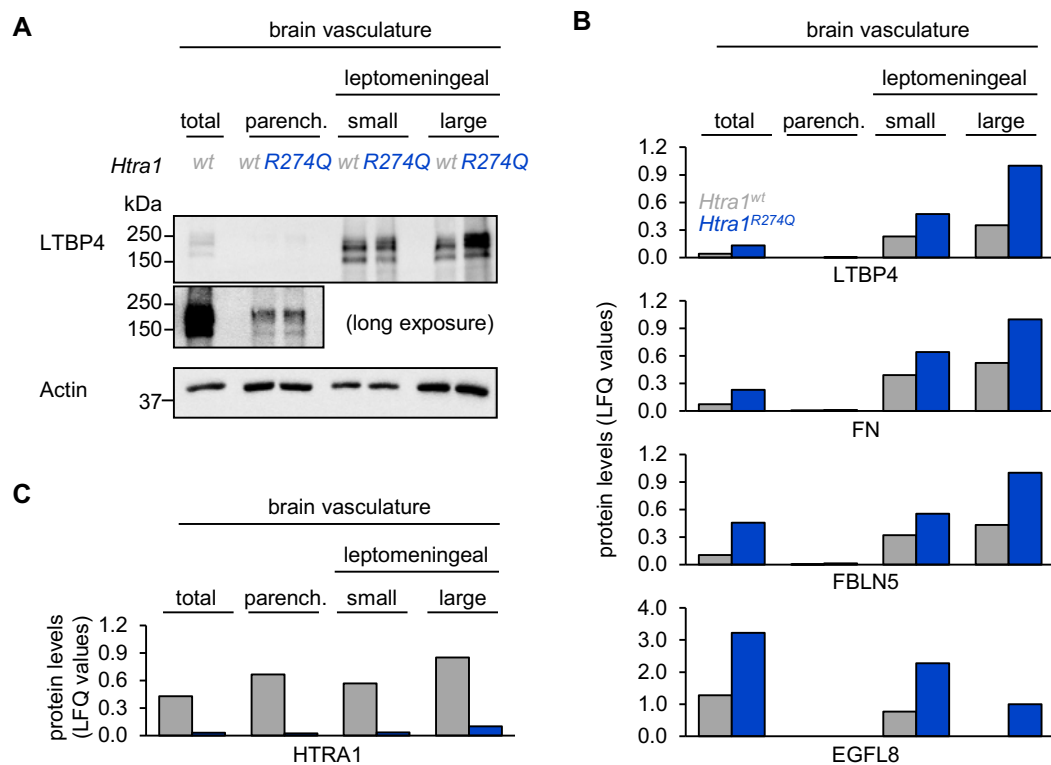


Figure 4.17 The ECM proteins upregulated in *Htra1*^{R274Q} vessels are predominantly expressed in leptomeningeal vessels

IB (A) and MS (B–C) analysis of distinct vessel fractions isolated from the brain of *Htra1*^{wt} or *Htra1*^{R274Q} mice. Total: vessel isolates derived from 1 full brain, all other samples: pooled material derived from 3 animals per genotype. (B–C) LFQ plots of the indicated proteins. (parench.: parenchymal)

In summary, I established a novel vessel isolation procedure that allows the selective isolation and analysis (including MS analysis) of distinct vascular segments. In a preliminary assay, I observed that the proteins enriched in *Htra1*^{R274Q} vessels are mostly expressed in leptomeningeal *Htra1*^{wt} vessels. Moreover, I observed that the leptomeningeal vasculature is also their predominant site of accumulation in *Htra1*^{R274Q} vessels. In contrast, HTRA1 expression pattern is homogenous in the various vascular segments.

4.4 Mutation R274Q does not exert obvious dominant-negative effects in the mouse brain vasculature

In a further approach, I used the *Htra1*^{R274Q} mouse line to examine haploinsufficiency vs. putative dominant-negative effects.

To this end, I compared protein expression in *Htra1*^{wt}, heterozygous *Htra1*^{wt/R274Q}, and homozygous *Htra1*^{R274Q/R274Q} mice to that detected in hemizygous *Htra1*^{+/-} and *Htra1*^{-/-} (i.e., *Htra1*^{ko}) animals (Figure 4.18, A). Here I reasoned that if mutation R274Q exhibits dominant-negative properties, the phenotype of *Htra1*^{wt/R274Q} mice should be more severe than that of haploinsufficient *Htra1*^{+/-} animals.

In a pilot experiment, I investigated FN and LTBP4 expression levels in the leptomeningeal vasculature of 12-month-old mice by IHC, as described above.

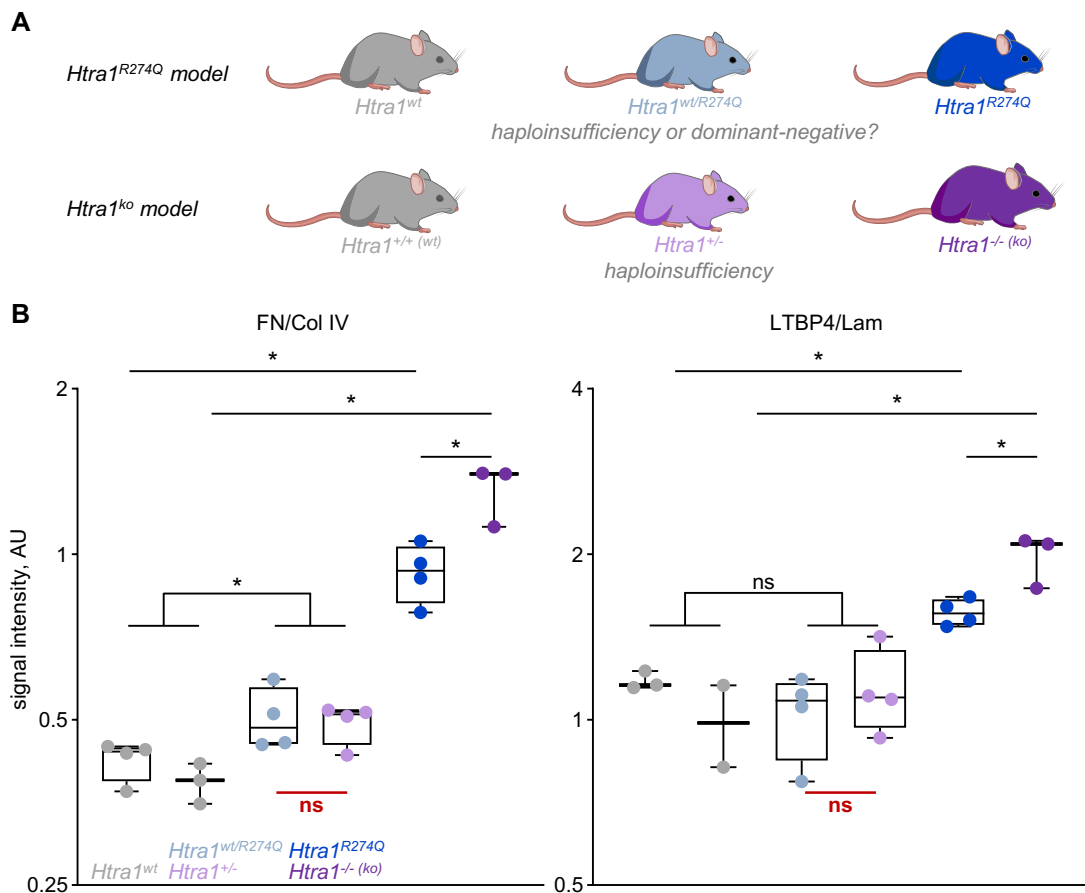


Figure 4.18 Comparison of FN and LTBP4 accumulation in the leptomeningeal vasculature of *Htra1*^{R274Q} and *Htra1*^{ko} mice does not reveal dominant-negative effects of mutation R274Q

(A) Brain sections from 12-month-old *Htra1*^{R274Q} mice were compared with age-matched *Htra1*^{ko} mice. (B) Quantification of fluorescence signal intensity (AU). Box-and-whisker plots (median, minimum, maximum) with filled circles. Data points represent individual mice ($n = 4$ mice/genotype); significance was tested by two-sided unpaired *t*-test.

Some accumulation of FN was detected in *Htra1*^{wt/R274Q} vessels, although it was much fainter than that observed in the vasculature of *Htra1*^{R274Q/R274Q} mice (Figure 4.18, B, left panel). This gene dosage effect is in accord with the milder phenotype reported in monoallelic compared to biallelic mutation carriers (see section 1.2.1.2).

Comparison of the two mouse lines further revealed that, as seen in *Htra1*^{R274Q/R274Q} mice, FN accumulated in *Htra1*^{-/-} brain vessels. In fact, enrichment was even stronger.

As a distinct finding, I found comparable FN levels in *Htra1*^{wt/R274Q} and *Htra1*^{+/-} leptomeningeal vessels, speaking in favor of haploinsufficiency rather than dominant-negative effects.

A very similar pattern was observed for LTBP4, except that accumulation did not reach significance in heterozygous *Htra1*^{wt/R274Q} and *Htra1*^{+/-} mice (Figure 4.18, B, right panel).

Although preliminary and restricted to the analysis of two proteins, my observations rather argue against a dominant-negative effect of R274Q.

5 DISCUSSION

In my thesis, I have combined high-throughput and targeted methods to characterize the proteome of the brain vasculature of *Htra1*^{R274Q} mice. I further tested the efficacy of an AAV encoding a rescue HTRA1 variant to alleviate the phenotype of *Htra1*^{R274Q} brain vessels and evaluated the putative dominant-negative properties of mutation R274Q *in vivo*.

5.1 Cerebrovascular consequences of HTRA1 mutation R274Q

Until now, mouse models to study the effects of HTRA1 loss of function were restricted to HTRA1-deficient mice. The novel HTRA1-mutant line used for my work bears the missense mutation R274Q, as identified in two CARASIL pedigrees (Badachi et al., 2020, Nishimoto et al., 2011a). In addition to genocopying the human condition, *Htra1*^{R274Q} mice represent a useful experimental model to investigate specific aspects that cannot be addressed in *Htra1*^{ko} mice, related to, e.g., gene expression, protein folding and stability, and multimeric assembly. In fact, I detected a marked reduction of HTRA1 protein levels in *Htra1*^{R274Q} compared to *Htra1*^{wt} animals, whereas mRNA levels remained comparable. These observations suggest defects in folding or stability of monomeric HTRA1-R274Q. They are in accord with the fact that multimeric assembly is a common regulator of protein half-life, with monomers being less stable than multimers (Mallik et al., 2018). In addition, my results highlight HTRA1-R274Q protein disruption as the main cause for HTRA1 loss of function in *Htra1*^{R274Q} vessels. Future experiments could thus consider the role of the protein quality control systems in this process.

Previous work of the laboratory of Martin Dichgans already showed that elderly (i.e., 20-month-old) *Htra1*^{ko} mice do not exhibit gross cerebrovascular abnormalities, such as BBB disruption or WM lesions. In contrast, they display marked alterations of the cerebrovascular proteome (Scharrer, 2015, Zellner et al., 2018). Using IHC, IB, and MS on cerebral vessels, I could now detect changes of the cerebrovascular proteome at a much earlier time point (i.e., at 6 months). Apart from the aforementioned reduced HTRA1 protein levels, these changes were mostly restricted to a distinct accumulation of ECM and ECM-associated proteins (this aspect is discussed in a separate paragraph, see section 5.2). In particular, the accumulation of matrisomal proteins was qualitatively comparable to that previously observed in elderly *Htra1*^{ko} mice. However, it was quantitatively attenuated as fewer proteins accumulated and with a lower enrichment factor.

MS analysis highlighted FN, LTBP4, FBLN5, and EGFL8 as the most upregulated proteins in *Htra1*^{R274Q} brain vessels and thus as promising candidates for further mechanistic studies. In addition, they represent early-onset readouts for intervention assays. While FN and FBLN5

are known substrates of HTRA1 (Grau et al., 2006, Vierkotten et al., 2011), recent follow-up *in vitro* analyses by the laboratory of Martin Dichgans demonstrated that LTBP4 and EGFL8 are also cleaved by HTRA1 (Malik et al., 2021, ISD München, unpublished results).

The clear molecular phenotype detected in *Htra1*^{R274Q} brain vessels opens questions on the absence of vessel dysfunction in HTRA1-mutant mice. While mouse models naturally can only partly reproduce the human pathology, the following aspects are of particular importance: First, mice have a short life span compared to humans. Therefore, the aging process might mask disease-related alterations (which are themselves age-dependent). Second, the cerebrovascular phenotype of mice overexpressing a CADASIL-causing mutant NOTCH3 is strongly attenuated in C57BL/6 mice (i.e., the strain in which *Htra1*^{R274Q} mice were generated) compared to FVB/N mice (Lee et al., 2012), indicating that certain mouse strains are more prone to develop brain vasculopathy. Third, HTRA1 loss of function might be compensated by, e.g., HTRA3 or HTRA4.

Nevertheless, *Htra1*^{R274Q} mice can serve as a reliable model to study the initial molecular consequences of HTRA1 loss of function. Alternatively, the addition of a “second hit” like hypertension could exacerbate the phenotype, resulting in brain vessel dysfunction and parenchymal lesions, as observed in humans.

5.2 Aberrant ECM in *Htra1*^{R274Q} mouse brain vessels

Recent genetic and proteomic studies have identified perturbations of the cerebrovascular matrisome as a central driver in cSVD pathogenesis (Dichgans et al., 2019, Joutel et al., 2016, Malik et al., 2021, Zellner et al., 2018). In accord, MS analysis of the full set of proteins affected by mutation R274Q pinpointed an accumulation of ECM and ECM-associated proteins. It is noteworthy that while some intracellular pools of HTRA1 have been described (Chien et al., 2009, Clawson et al., 2008), my data suggest that loss of the extracellular, matrisomal function of HTRA1 is involved in the pathogenesis of cSVD.

Among the matrisomal proteins upregulated in *Htra1*^{R274Q} brain vessels, LTBP4, EGFL8, FBLN5, and FN exhibited the strongest enrichment. Interestingly, according to a single-cell sequencing-based atlas of the brain vasculature (Vanlandewijck et al., 2018), these proteins are all expressed by endothelial cells, and their expression is elevated in arterial compared to capillary endothelial cells. This is in accord (i) with my IHC observations, detecting LTBP4 and FN accumulation in the subendothelial vessel wall of *Htra1*^{R274Q} leptomeningeal arteries, and (ii) with the emerging concept that, besides matrisomal perturbations, endothelial dysfunction might be a key pathomechanism in cSVD (Wardlaw et al., 2019).

Single-cell sequencing of the brain vasculature has revealed that, within the same vascular cell type, the expression repertoire is highly variable across distinct vascular segments (Vanlandewijck et al., 2018). Moreover, some cSVD-related alterations have been shown to exhibit zonation, preferentially affecting, e.g., pericytes or mural cells of the so-called transi-

tional segment (Ghosh et al., 2015, Ratelade et al., 2020). To assess the consequences of R274Q on the overall vascular proteome and in a vessel segment-specific manner, I developed a brain vessel fractionation protocol. The resulting fractions are enriched in large leptomeningeal vessels, small leptomeningeal vessels, or parenchymal vessels and are suitable for, e.g., IB or MS analysis. Notably, compared to the overall vasculature, the parenchymal vessel fraction is depleted from large vessels. In a test run, I could confirm that, in accord with my IHC data, (i) the proteins enriched in *Htra1*^{R274Q} vessels are mainly expressed in leptomeningeal vessels in control brain and that (ii) the leptomeningeal vasculature is also their predominant site of accumulation in *Htra1*^{R274Q} brain. These results highlight the protocol's utility, e.g., to identify the consequences of HTRA1 loss of function by focusing on the parenchymal vasculature or to analyze other experimental models of cSVD. In conclusion, I developed a novel vessel isolation procedure that allows the selective analysis of distinct vascular segments and can be used for further research.

The fact that a “small vessel” disease mostly manifests in leptomeningeal arteries and arterioles is rather counterintuitive. However, in accord with my data, most publications on the histopathology of HTRA1-related cSVD depict mainly large leptomeningeal vessels (Hara et al., 2009, Ito et al., 2018, Ito et al., 2016, Oide et al., 2008). Although these reports do not particularly disclose how the depicted vessels were chosen and whether smaller and/or parenchymal vessels had been investigated, this observation suggests that my findings also hold true in human cases.

Of importance, FBLN5, LTBP4, and FN are well-described regulators of elastogenesis (Figure 5.1). Following secretion, the monomeric elastin precursor (tropoelastin) self-assembles and is crosslinked by lysyl oxidases (LOXs), resulting in the formation of elastin aggregates. These aggregates interact with LTBP4, which, along with FBLN5, mediates their deposition onto a microfibril scaffold made of fibrillins and FN. This is followed by additional LOX-dependent crosslinking steps (Beyens et al., 2021, Noda et al., 2013, Papke et al., 2014, Schmelzer et al., 2020). While the vascular functions of EGFL8 have not been elucidated, the homologous protein EGFL7 has been identified as a LOX inhibitor (Lelièvre et al., 2008). Hence, my data suggest that HTRA1 loss of function interferes with elastogenesis, consistent with the observation that proteome changes are primarily detected in elastin-rich *Htra1*^{R274Q} vessels (i.e., arterioles and arteries). Most importantly, splitting of the internal elastic lamina has been observed and is even a common feature in the brain of cSVD cases, including HTRA1-related cSVD cases (Hara et al., 2009, Ito et al., 2018, Ito et al., 2016, Oide et al., 2008), strongly supporting the pathophysiological relevance of my findings.

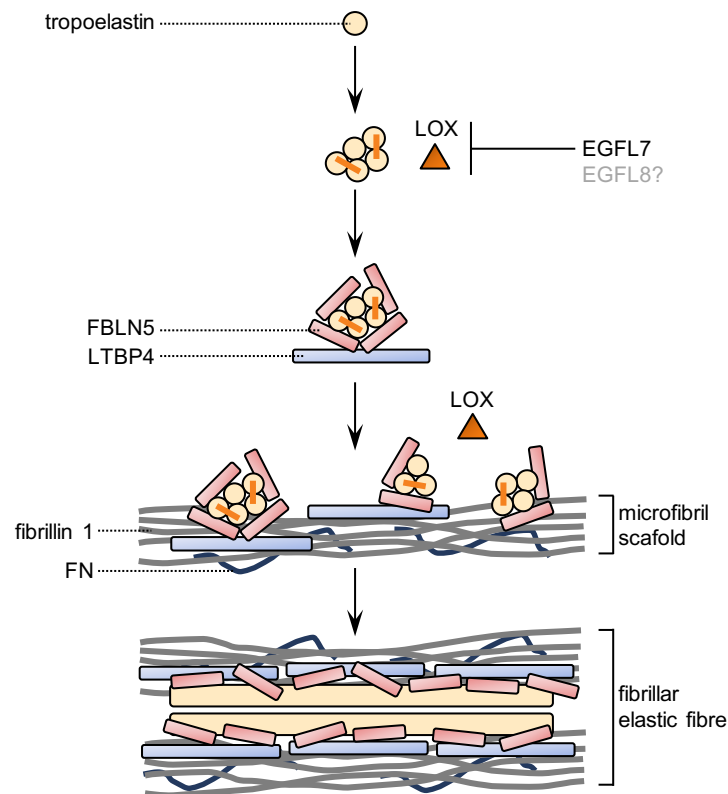


Figure 5.1 Proteins upregulated in *Htra1*^{R274Q} vessels are involved in elastogenesis

LTBP4 and FBLN5 facilitate elastin deposition onto the microfibril scaffold composed of fibrillins and FN. EGFL7 (and possibly EGFL8) inhibit LOXs.

5.3 AAV-mediated expression of a protein-based HTRA1 corrector in the brain vasculature

Delivering drugs or therapeutic gene products to the central nervous system safely, efficiently, and with a high tissue specificity is one of the main challenges in treating CNS diseases, as the BBB constitutes a significant obstacle for many biologics (Pardridge, 2005). In recent years, AAVs have emerged as promising vectors in gene therapy, especially in the treatment of neurological disorders, as they effectively transduce neural cells and display low toxicity and immunogenicity (Chen et al., 2021, Liu et al., 2021, Peters et al., 2021). In fact, gene therapies for the treatment of monogenic neurological diseases such as spinal muscle atrophy and inherited vision loss using AAV-based vectors have already been approved for use in humans (Flomenberg et al., 2021, U.S. Food & Drug Administration, 2017, U.S. Food & Drug Administration, 2019). Hence, the possibility to treat *Htra1*^{R274Q} mice via the AAV-based delivery of a proteolytically inactive HTRA1 variant would open new therapeutic perspectives, as up to now, HTRA1-related cSVD is an incurable, fatal disorder.

In accord with the initial description of BR1-AAV2, I evidenced by RT-qPCR and IB selectively targeting recombinant HTRA1 that infection results in the long-time (i.e., at least 5 months) expression of a protein of interest in the brain vasculature (Körbelin et al., 2016) — at least in

the majority of the infected mice. A second injection of the virus might improve the rate of high expressor animals. Moreover, my data indicate that the HTRA1 corrector variant is well-expressed and well-tolerated *in vivo* and *in situ* in brain vessels. AAV-HTRA1 selective peptides were not detected by MS, and HTRA1 protein levels were not elevated in infected compared to naïve mice. This probably reflects the fact that the endothelial-specific expression of recombinant HTRA1 is masked by the large amounts of protein produced by astrocytes (i.e., the main cell type producing HTRA1 in the brain vasculature; see Figure 1.5; Vanlandewijck et al., 2018).

As expected, using an eGFP-encoding construct, I found that BR1-AAV2 efficiently transduces parenchymal capillaries (Körbelin et al., 2016). However, the virus poorly targets penetrating and leptomeningeal arteries and arterioles. These differences, which had not been reported, could involve, e.g., a vascular bed-dependent expression of the unknown endothelial receptor of BR1-AAV2. Furthermore, hydrodynamics, such as reduced blood flow velocity and pressure in capillaries compared to arteries/arterioles, might facilitate contacts between virus and endothelial cells and thus infection.

My data clearly show that infection with AAV-HTRA1-D174R-S328A does not alleviate the molecular phenotype of *Htra1*^{R274Q} brain vessels. However, the mediocre — if at all — delivery of AAV-HTRA1 to leptomeningeal arteries and arterioles, which are the primary site of molecular alterations in *Htra1*^{R274Q} brain vessels, is sufficient to explain this lack of efficacy. Meanwhile, other AAV vectors targeting the brain vasculature have been described (Ravindra Kumar et al., 2020) and should be tested regarding their capacity to transduce leptomeningeal arteries and arterioles

After the course of my thesis, the laboratory of Martin Dichgans elaborated on an alternative rescue paradigm. To ascertain the long-term expression of the corrector HTRA1 variant in all vascular cell types and all vascular segments, a genetic approach was selected. Specifically, a new mouse line bearing the corrector mutation (D174R) and an active site mutation (S328A) *in cis* was generated via CRISPR/Cas9 technology. These *Htra1*^{D174R-S328A} mice were then crossed with *Htra1*^{R274Q} animals, resulting in heterozygous mice in which the pathogenic (R274Q) and the rescue allele (D174R-S328A) are *in trans* (see Figure 5.2). While *Htra1*^{R274Q/D174R-S328A} mice display no functional *Htra1* allele, correction of the single *Htra1*^{R274Q} allele should alleviate the cerebrovascular phenotype, as seen in *Htra1*^{wt/R274Q} or *Htra1*^{+/-} compared to homozygous mutant mice.

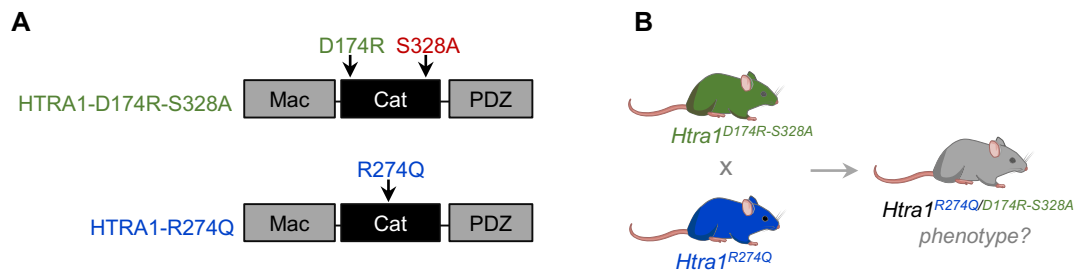


Figure 5.2 Genetic delivery of a protein-based HTRA1 corrector

(A) The rescue variant (green) displays a corrector mutation (D174R) and an active site mutation (S328A). The pathogenic mutation (R274Q) is depicted in blue. (B) *Htra1*^{D174R-S328A} mice were crossed with *Htra1*^{R274Q} mice to generate *Htra1*^{R274Q/D174R-S328A} mice.

Indeed, the molecular phenotype seen in the cerebrovasculature of *Htra1*^{R274Q} mice was attenuated in *Htra1*^{R274Q/D174R-S328A} animals (ISD München, unpublished results). These observations provide proof of principle for functional correction of HTRA1-R274Q *in vivo*.

5.4 Putative dominant-negative properties of mutation R274Q

Since the first report of Verdura and colleagues in 2015, heterozygous *HTRA1* mutations have emerged as a significant cause of familial cSVD. Moreover, recent work of the laboratory of Martin Dichgans linked heterozygous missense mutations targeting the protease domain of HTRA1 and reducing its protease function to white matter hyperintensity burden (a hallmark of cSVD) in the general population (Malik et al., 2021), further raising interest in the underlying pathogenic mechanisms.

A subset of disease-causing mutations — including R274Q along with other mutations that either impair the trimeric assembly of HTRA1 or interfere with the trimer-mediated activation cascade — has been proposed to exert dominant-negative effects. This hypothesis is supported by the fact that heterozygous carriers harboring those mutations display a more severe phenotype than probands carrying other *HTRA1* mutations (Lee et al., 2018, Uemura et al., 2020) and by *in vitro* experiments using overexpressed proteins and protease activity assays against non-physiological substrates (Nozaki et al., 2016, Uemura et al., 2019).

To investigate the putative dominant-negative effects of mutation R274Q *in vivo*, I compared the brain vasculature of heterozygous *Htra1*^{wt/R274Q} mice to that of hemizygous *Htra1*^{+/-} mice. Although my observations are limited to the analysis of FN and LTBP4 abundance in the leptomeningeal vasculature, I found no exacerbation of the cerebrovascular phenotype in *Htra1*^{wt/R274Q} mice. I thus propose that HTRA1 haploinsufficiency rather than dominant-negative effects could cause a milder and less penetrant form of cSVD compared to CARASIL.

Several arguments speak in favor of this possibility: First, HTRA1-related late-onset cSVD has been reported in heterozygous carriers of nonsense or frameshift *HTRA1* mutations (Liu

et al., 2020, Uemura et al., 2020). Second, several “recessive” missense mutations, such as V297M, have been identified in symptomatic heterozygous carriers, whereas some asymptomatic carriers exhibit “dominant” mutations. Third, there is a higher frequency of male probands and vascular risk factors in HTRA1-related late-onset cSVD, suggesting that beyond HTRA1 function, other genetic and environmental factors might be involved in the development of the disease (Uemura et al., 2020).

To complete my observations, follow-up experiments should examine the overall consequences of HTRA1-R274Q compared to HTRA1-KO on the brain vasculature. These assays could include, e.g., a time-resolved analysis of the entire vascular proteome by MS, as well as that of distinct vascular beds based on the vessel fractionation protocol I established. Besides, it would be of great interest to investigate the consequences of a mutation that interferes with the HTRA1 activation cascade, such as P285Q or R302Q (Nozaki et al., 2016, Uemura et al., 2019).

Interestingly, my work revealed that FN and LTBP4 accumulation was markedly enhanced in the leptomeningeal vasculature of *Htra1^{ko}* compared to homozygous *Htra1^{R274Q}* animals, suggesting that despite the low protein levels, HTRA1-R274Q might display residual protease activity. Alternatively, non-proteolytic functions of HTRA1 might be involved in cSVD pathogenesis. My observations thus open new possibilities for the functional correction of HTRA1-R274Q. Residual enzymatic activity could be stimulated by protease activity modulators such as PDZ-dependent activators (Krojer et al., 2010). Alternatively, HTRA1-R274Q could be stabilized by chaperones such as 4-phenyl butyric acid (4-BPA). This approved drug, used to treat urea cycle disorders (Cortez et al., 2014), is known to stabilize mutant proteins and reduce endoplasmic reticulum stress (Hetz et al., 2013).

Collectively, my observations provide new insights into the mechanisms underlying HTRA1-related cSVD. In particular, my work opens new perspectives for mechanistic studies focusing on the role and consequences of elastogenesis defects. My observations also provide a working basis for future intervention assays targeting, e.g., HTRA1 multimeric assembly or stability with potential therapeutic applications.

COPYRIGHT DECLARATION

All figures for which no source information is provided are my own work. Figures that do not need a permission for use in a dissertation per the publisher, or figures that were generated in my host laboratory, i.e., the laboratory of Martin Dichgans (and are reproduced with permission from its authors) have a respective credit line in the figure legend. For the figures listed in the following table, permission for the reproduction has been obtained through the RightsLink Copyright Clearance Center⁶ or via direct permission request through the publisher's website.

Figure	Reference	Publisher	License number
Figure 1.1 Figure 1.2, A-D	Wardlaw et al., 2013a	Elsevier	4954740342137
Figure 1.2, E-G	Pantoni, 2010	Elsevier	4954740619128
Figure 1.3, E-G	Ito et al., 2018	John Wiley and Sons	4947000688584
Figure 1.4, A	Zellner et al., 2018	Springer Nature	4951290522302
Figure 1.4, B	Hondius et al., 2018	Springer Nature	Creative Commons license (Attribution 4.0 International CC BY 4.0) ⁷
Figure 3.2	Beaufort et al., 2014	National Academy of Sciences	Direct request through the publisher's website

⁶ URL: <https://www.copyright.com/>

⁷ URL: <https://creativecommons.org/licenses/by/4.0/>

BIBLIOGRAPHY

- Arima, K., Yanagawa, S., Ito, N., & Ikeda, S. 2003. Cerebral arterial pathology of CADASIL and CARASIL (Maeda syndrome). *Neuropathology*, 23, 327-34.
- Badachi, S., John, S. K., Sekhar, M., & Mathew, T. 2020. CARASIL; The Backache, Baldness, Brain Attack Syndrome: The Indian Scenario. *Ann Indian Acad Neurol*, 23, 559-561.
- Beaufort, N., Scharrer, E., Kremmer, E., Lux, V., Ehrmann, M., Huber, R., . . . Dichgans, M. 2014. Cerebral small vessel disease-related protease HtrA1 processes latent TGF- β binding protein 1 and facilitates TGF- β signaling. *Proc Natl Acad Sci U S A*, 111, 16496-501.
- Beyens, A., Boel, A., Symoens, S., & Callewaert, B. 2021. Cutis laxa: A comprehensive overview of clinical characteristics and pathophysiology. *Clin Genet*, 99, 53-66.
- Bos, D., Wolters, F. J., Darweesh, S. K. L., Vernooij, M. W., de Wolf, F., Ikram, M. A., & Hofman, A. 2018. Cerebral small vessel disease and the risk of dementia: A systematic review and meta-analysis of population-based evidence. *Alzheimers Dement*, 14, 1482-1492.
- Bowler, J. V. & Hachinski, V. 1994. Progress in the genetics of cerebrovascular disease: inherited subcortical arteriopathies. *Stroke*, 25, 1696-8.
- Bultmann-Mellin, I., Conradi, A., Maul, A. C., Dinger, K., Wempe, F., Wohl, A. P., . . . Sterner-Kock, A. 2015. Modeling autosomal recessive cutis laxa type 1C in mice reveals distinct functions for Ltbp-4 isoforms. *Dis Model Mech*, 8, 403-15.
- Cai, B., Zeng, J., Lin, Y., Lin, Y., Lin, W., Lin, W., . . . Wang, N. 2015. A frameshift mutation in HTRA1 expands CARASIL syndrome and peripheral small arterial disease to the Chinese population. *Neurol Sci*, 36, 1387-91.
- Chabriat, H., Joutel, A., Dichgans, M., Tournier-Lasserre, E., & Boussier, M. G. 2009. CADASIL. *Lancet Neurol*, 8, 643-53.
- Chen, W., Yao, S., Wan, J., Tian, Y., Huang, L., Wang, S., . . . Zhang, X. 2021. BBB-crossing adeno-associated virus vector: An excellent gene delivery tool for CNS disease treatment. *J Control Release*, 333, 129-138.
- Chien, J., Ota, T., Aletti, G., Shridhar, R., Boccellino, M., Quagliuolo, L., . . . Shridhar, V. 2009. Serine protease HtrA1 associates with microtubules and inhibits cell migration. *Mol Cell Biol*, 29, 4177-87.
- Clausen, T., Kaiser, M., Huber, R., & Ehrmann, M. 2011. HTRA proteases: regulated proteolysis in protein quality control. *Nat Rev Mol Cell Biol*, 12, 152-62.
- Clausen, T., Southan, C., & Ehrmann, M. 2002. The HtrA family of proteases: implications for protein composition and cell fate. *Mol Cell*, 10, 443-55.
- Clawson, G. A., Bui, V., Xin, P., Wang, N., & Pan, W. 2008. Intracellular localization of the tumor suppressor HtrA1/Prss11 and its association with HPV16 E6 and E7 proteins. *J Cell Biochem*, 105, 81-8.
- Cortez, L. & Sim, V. 2014. The therapeutic potential of chemical chaperones in protein folding diseases. *Prion*, 8, 197-202.
- Craggs, L. J., Yamamoto, Y., Deramecourt, V., & Kalara, R. N. 2014. Microvascular pathology and morphometrics of sporadic and hereditary small vessel diseases of the brain. *Brain Pathol*, 24, 495-509.
- Di Donato, I., Bianchi, S., De Stefano, N., Dichgans, M., Dotti, M. T., Duering, M., . . . Federico, A. 2017a. Cerebral Autosomal Dominant Arteriopathy with Subcortical

- Infarcts and Leukoencephalopathy (CADASIL) as a model of small vessel disease: update on clinical, diagnostic, and management aspects. *BMC Med*, 15, 41.
- Di Donato, I., Bianchi, S., Gallus, G. N., Cerase, A., Taglia, I., Pescini, F., . . . Dotti, M. T. 2017b. Heterozygous mutations of HTRA1 gene in patients with familial cerebral small vessel disease. *CNS Neurosci Ther*, 23, 759-765.
- Dichgans, M., Pulit, S. L., & Rosand, J. 2019. Stroke genetics: discovery, biology, and clinical applications. *Lancet Neurol*, 18, 587-599.
- Doudna, J. A. & Charpentier, E. 2014. Genome editing. The new frontier of genome engineering with CRISPR-Cas9. *Science*, 346, 1258096.
- Eigenbrot, C., Ultsch, M., Lipari, M. T., Moran, P., Lin, S. J., Ganesan, R., . . . Kirchhofer, D. 2012. Structural and functional analysis of Htra1 and its subdomains. *Structure*, 20, 1040-50.
- Flomenberg, P. & Daniel, R. 2021. Overview of gene therapy, gene editing, and gene silencing. In: Post, T. W. (ed.) *UpToDate*. UpToDate, Waltham, MA. [Accessed November 8, 2021].
- Fukutake, T. 2011. Cerebral autosomal recessive arteriopathy with subcortical infarcts and leukoencephalopathy (CARASIL): from discovery to gene identification. *J Stroke Cerebrovasc Dis*, 20, 85-93.
- Fukutake, T. & Hirayama, K. 1995. Familial young-adult-onset arteriosclerotic leukoencephalopathy with alopecia and lumbago without arterial hypertension. *Eur Neurol*, 35, 69-79.
- Ghosh, M., Balbi, M., Hellal, F., Dichgans, M., Lindauer, U., & Plesnila, N. 2015. Pericytes are involved in the pathogenesis of cerebral autosomal dominant arteriopathy with subcortical infarcts and leukoencephalopathy. *Ann Neurol*, 78, 887-900.
- Gould, D. B., Phalan, F. C., van Mil, S. E., Sundberg, J. P., Vahedi, K., Massin, P., . . . John, S. W. 2006. Role of COL4A1 in small-vessel disease and hemorrhagic stroke. *N Engl J Med*, 354, 1489-96.
- Graham, J. R., Chamberland, A., Lin, Q., Li, X. J., Dai, D., Zeng, W., . . . Yang, Z. 2013. Serine protease HTRA1 antagonizes transforming growth factor- β signaling by cleaving its receptors and loss of HTRA1 in vivo enhances bone formation. *PLoS One*, 8, e74094.
- Grau, S., Richards, P. J., Kerr, B., Hughes, C., Caterson, B., Williams, A. S., . . . Ehrmann, M. 2006. The role of human Htra1 in arthritic disease. *J Biol Chem*, 281, 6124-9.
- Greenberg, S. M. 2021. Cerebral amyloid angiopathy. In: Post, T. W. (ed.) *UpToDate*. UpToDate, Waltham, MA. [Accessed November 8, 2021].
- Haffner, C., Malik, R., & Dichgans, M. 2016. Genetic factors in cerebral small vessel disease and their impact on stroke and dementia. *J Cereb Blood Flow Metab*, 36, 158-71.
- Hara, K., Shiga, A., Fukutake, T., Nozaki, H., Miyashita, A., Yokoseki, A., . . . Onodera, O. 2009. Association of HTRA1 mutations and familial ischemic cerebral small-vessel disease. *N Engl J Med*, 360, 1729-39.
- He, L., Vanlandewijck, M., Mäe, M. A., Andrae, J., Ando, K., Del Gaudio, F., . . . Betsholtz, C. 2018. Single-cell RNA sequencing of mouse brain and lung vascular and vessel-associated cell types. *Sci Data*, 5, 180160.
- Hetz, C., Chevet, E., & Harding, H. P. 2013. Targeting the unfolded protein response in disease. *Nat Rev Drug Discov*, 12, 703-19.
- Hondius, D. C., Eigenhuis, K. N., Morrema, T. H. J., van der Schors, R. C., van Nierop, P., Bugiani, M., . . . Rozemuller, A. J. M. 2018. Proteomics analysis identifies new markers associated with capillary cerebral amyloid angiopathy in Alzheimer's disease. *Acta Neuropathol Commun*, 6, 46.
- Iadecola, C. 2017. The Neurovascular Unit Coming of Age: A Journey through Neurovascular Coupling in Health and Disease. *Neuron*, 96, 17-42.

- Ikawati, M., Kawaichi, M., & Oka, C. 2018. Loss of HtrA1 serine protease induces synthetic modulation of aortic vascular smooth muscle cells. *PLoS One*, 13, e0196628.
- Ito, J., Nozaki, H., Toyoshima, Y., Abe, T., Sato, A., Hashidate, H., . . . Kakita, A. 2018. Histopathologic features of an autopsied patient with cerebral small vessel disease and a heterozygous HTRA1 mutation. *Neuropathology*, 38, 428-432.
- Ito, S., Takao, M., Fukutake, T., Hatsuta, H., Funabe, S., Ito, N., . . . Murayama, S. 2016. Histopathologic Analysis of Cerebral Autosomal Recessive Arteriopathy with Subcortical Infarcts and Leukoencephalopathy (CARASIL): A Report of a New Genetically Confirmed Case and Comparison to 2 Previous Cases. *J Neuropathol Exp Neurol*, 75, 1020-1030.
- Jakobsson, L. & van Meeteren, L. A. 2013. Transforming growth factor β family members in regulation of vascular function: in the light of vascular conditional knockouts. *Exp Cell Res*, 319, 1264-70.
- Joutel, A., Corpechot, C., Ducros, A., Vahedi, K., Chabriat, H., Mouton, P., . . . Tournier-Lasserre, E. 1996. Notch3 mutations in CADASIL, a hereditary adult-onset condition causing stroke and dementia. *Nature*, 383, 707-10.
- Joutel, A., Haddad, I., Ratelade, J., & Nelson, M. T. 2016. Perturbations of the cerebrovascular matrisome: A convergent mechanism in small vessel disease of the brain? *J Cereb Blood Flow Metab*, 36, 143-57.
- Kast, J., Hanecker, P., Beaufort, N., Giese, A., Joutel, A., Dichgans, M., . . . Haffner, C. 2014. Sequestration of latent TGF- β binding protein 1 into CADASIL-related Notch3-ECD deposits. *Acta Neuropathol Commun*, 2, 96.
- Körbelin, J., Dogbevia, G., Michelfelder, S., Ridder, D. A., Hunger, A., Wenzel, J., . . . Trepel, M. 2016. A brain microvasculature endothelial cell-specific viral vector with the potential to treat neurovascular and neurological diseases. *EMBO Mol Med*, 8, 609-25.
- Krojer, T., Sawa, J., Huber, R., & Clausen, T. 2010. HtrA proteases have a conserved activation mechanism that can be triggered by distinct molecular cues. *Nat Struct Mol Biol*, 17, 844-52.
- Kuo, D. S., Labelle-Dumais, C., & Gould, D. B. 2012. COL4A1 and COL4A2 mutations and disease: insights into pathogenic mechanisms and potential therapeutic targets. *Hum Mol Genet*, 21, R97-110.
- Lee, J. H., Bacskai, B. J., & Ayata, C. 2012. Genetic animal models of cerebral vasculopathies. *Prog Mol Biol Transl Sci*, 105, 25-55.
- Lee, Y. C., Chung, C. P., Chao, N. C., Fuh, J. L., Chang, F. C., Soong, B. W., & Liao, Y. C. 2018. Characterization of Heterozygous HTRA1 Mutations in Taiwanese Patients With Cerebral Small Vessel Disease. *Stroke*, 49, 1593-1601.
- Lelièvre, E., Hinek, A., Lupu, F., Buquet, C., Soncin, F., & Mattot, V. 2008. VE-statin/egfl7 regulates vascular elastogenesis by interacting with lysyl oxidases. *Embo j*, 27, 1658-70.
- Liu, D., Zhu, M., Zhang, Y., & Diao, Y. 2021. Crossing the blood-brain barrier with AAV vectors. *Metab Brain Dis*, 36, 45-52.
- Liu, J. Y., Zhu, Y. C., Zhou, L. X., Wei, Y. P., Mao, C. H., Cui, L. Y., . . . Yao, M. 2020. HTRA1-related autosomal dominant cerebral small vessel disease. *Chin Med J (Engl)*, 134, 178-184.
- Maeda, S., Nakayama, H., Isaka, K., Aihara, Y., & Nemoto, S. 1976. Familial unusual encephalopathy of Binswanger's type without hypertension. *Folia Psychiatr Neurol Jpn*, 30, 165-77.
- Malik, R., Beaufort, N., Frerich, S., Gesierich, B., Georgakis, M. K., Rannikmäe, K., . . . Dichgans, M. 2021. Whole-exome sequencing reveals a role of HTRA1 and EGFL8 in brain white matter hyperintensities. *Brain*, 144, 2670-2682.

- Malik, R. & Chauhan, G. & Traylor, M. & Sargurupremraj, M. & Okada, Y. & Mishra, A., . . . Dichgans, M. 2018. Multiancestry genome-wide association study of 520,000 subjects identifies 32 loci associated with stroke and stroke subtypes. *Nat Genet*, 50, 524-537.
- Mallik, S. & Kundu, S. 2018. Topology and Oligomerization of Mono- and Oligomeric Proteins Regulate Their Half-Lives in the Cell. *Structure*, 26, 869-878.e3.
- Müller, K., Courtois, G., Ursini, M. V., & Schwaninger, M. 2017. New Insight Into the Pathogenesis of Cerebral Small-Vessel Diseases. *Stroke*, 48, 520-527.
- Muñoz Maniega, S., Chappell, F. M., Valdés Hernández, M. C., Armitage, P. A., Makin, S. D., Heye, A. K., . . . Wardlaw, J. M. 2017. Integrity of normal-appearing white matter: Influence of age, visible lesion burden and hypertension in patients with small-vessel disease. *J Cereb Blood Flow Metab*, 37, 644-656.
- Muthusamy, K., Ferrer, A., Klee, E. W., Wierenga, K. J., & Gavrilova, R. H. 2021. Clinicoradiographic and genetic features of cerebral small vessel disease indicate variability in mode of inheritance for monoallelic HTRA1 variants. *Mol Genet Genomic Med*, e1799.
- Nishimoto, Y., Shibata, M., Nihonmatsu, M., Nozaki, H., Shiga, A., Shirata, A., . . . Suzuki, N. 2011a. A novel mutation in the HTRA1 gene causes CARASIL without alopecia. *Neurology*, 76, 1353-5.
- Nishimoto, Y., Shibata, M., Onodera, O., & Suzuki, N. 2011b. Neurological picture. Neuroaxonal integrity evaluated by MR spectroscopy in a case of CARASIL. *J Neurol Neurosurg Psychiatry*, 82, 860-1.
- Noda, K., Dabovic, B., Takagi, K., Inoue, T., Horiguchi, M., Hirai, M., . . . Nakamura, T. 2013. Latent TGF- β binding protein 4 promotes elastic fiber assembly by interacting with fibulin-5. *Proc Natl Acad Sci U S A*, 110, 2852-7.
- Nozaki, H., Kato, T., Nihonmatsu, M., Saito, Y., Mizuta, I., Noda, T., . . . Onodera, O. 2016. Distinct molecular mechanisms of HTRA1 mutants in manifesting heterozygotes with CARASIL. *Neurology*, 86, 1964-74.
- Nozaki, H., Nishizawa, M., & Onodera, O. 2014. Features of cerebral autosomal recessive arteriopathy with subcortical infarcts and leukoencephalopathy. *Stroke*, 45, 3447-53.
- Oide, T., Nakayama, H., Yanagawa, S., Ito, N., Ikeda, S., & Arima, K. 2008. Extensive loss of arterial medial smooth muscle cells and mural extracellular matrix in cerebral autosomal recessive arteriopathy with subcortical infarcts and leukoencephalopathy (CARASIL). *Neuropathology*, 28, 132-42.
- Oluwole, O. J., Ibrahim, H., Garozzo, D., Ben Hamouda, K., Ismail Mostafa Hassan, S., Hegazy, A. M., & Msaddi, A. K. 2020. Cerebral small vessel disease due to a unique heterozygous HTRA1 mutation in an African man. *Neurol Genet*, 6, e382.
- Onodera, O., Nozaki, H., & Fukutake, T. 2010. (Updated November 7, 2019). HTRA1 Disorder. In: Adam, M. P., Ardinger, H. H., Pagon, R. A., Wallace, S. E., Bean, L. J. H., Stephens, K., & Amemiya, A. (eds.) *GeneReviews*®. University of Washington, Seattle, WA. [Accessed November 8, 2021].
- Pantoni, L. 2010. Cerebral small vessel disease: from pathogenesis and clinical characteristics to therapeutic challenges. *Lancet Neurol*, 9, 689-701.
- Papke, C. L. & Yanagisawa, H. 2014. Fibulin-4 and fibulin-5 in elastogenesis and beyond: Insights from mouse and human studies. *Matrix Biol*, 37, 142-9.
- Pardridge, W. M. 2005. The blood-brain barrier and neurotherapeutics. *NeuroRx*, 2, 1-2.
- Pati, A. R., Battisti, C., Taglia, I., Galluzzi, P., Bianchi, M., & Federico, A. 2018. A new case of autosomal dominant small vessel disease carrying a novel heterozygous mutation in HTRA1 gene: 2-year follow-up. *Neurol Sci*, 39, 1479-1481.
- Peters, C. W., Maguire, C. A., & Hanlon, K. S. 2021. Delivering AAV to the Central Nervous and Sensory Systems. *Trends Pharmacol Sci*, 42, 461-474.

- Rannikmäe, K., Davies, G., Thomson, P. A., Bevan, S., Devan, W. J., Falcone, G. J., . . . Sudlow, C. L. 2015. Common variation in COL4A1/COL4A2 is associated with sporadic cerebral small vessel disease. *Neurology*, 84, 918-26.
- Ratelade, J., Klug, N. R., Lombardi, D., Angelim, M., Dabertrand, F., Domenga-Denier, V., . . . Joutel, A. 2020. Reducing Hypermuscularization of the Transitional Segment Between Arterioles and Capillaries Protects Against Spontaneous Intracerebral Hemorrhage. *Circulation*, 141, 2078-2094.
- Ravindra Kumar, S., Miles, T. F., Chen, X., Brown, D., Dobрева, T., Huang, Q., . . . Gradinaru, V. 2020. Multiplexed Cre-dependent selection yields systemic AAVs for targeting distinct brain cell types. *Nat Methods*, 17, 541-550.
- Scharrer, E. 2015. *Consequences of Htra1 deficiency on TGF-Beta signaling*. Ludwig-Maximilians-Universität München.
- Schmelzer, C. E. H., Hedtke, T., & Heinz, A. 2020. Unique molecular networks: Formation and role of elastin cross-links. *IUBMB Life*, 72, 842-854.
- Schmidt, H., Zeginigg, M., Wiltgen, M., Freudenberger, P., Petrovic, K., Cavalieri, M., . . . Schmidt, R. 2011. Genetic variants of the NOTCH3 gene in the elderly and magnetic resonance imaging correlates of age-related cerebral small vessel disease. *Brain*, 134, 3384-97.
- Shang, T., Pinho, M., Ray, D., & Khera, A. 2021. Two Unique Mutations in HTRA1-Related Cerebral Small Vessel Disease in North America and Africa and Literature Review. *J Stroke Cerebrovasc Dis*, 30, 106029.
- Shiga, A., Nozaki, H., Yokoseki, A., Nihonmatsu, M., Kawata, H., Kato, T., . . . Onodera, O. 2011. Cerebral small-vessel disease protein HTRA1 controls the amount of TGF- β 1 via cleavage of proTGF- β 1. *Hum Mol Genet*, 20, 1800-10.
- Smith, E. & Wright, C. B. 2021. Etiology, clinical manifestations, and diagnosis of vascular dementia. In: Post, T. W. (ed.) *UpToDate*. UpToDate, Waltham, MA. [Accessed November 8, 2021].
- Tan, R. Y. Y., Traylor, M., Megy, K., Duarte, D., Deevi, S. V. V., Shamardina, O., . . . Markus, H. S. 2019. How common are single gene mutations as a cause for lacunar stroke? A targeted gene panel study. *Neurology*, 93, e2007-e2020.
- ten Dijke, P. & Arthur, H. M. 2007. Extracellular control of TGFbeta signalling in vascular development and disease. *Nat Rev Mol Cell Biol*, 8, 857-69.
- Thaler, F. S., Catak, C., Einhäupl, M., Müller, S., Seelos, K., Wollenweber, F. A., & Kümpfel, T. 2018. Cerebral small vessel disease caused by a novel heterozygous mutation in HTRA1. *J Neurol Sci*, 388, 19-21.
- Thompson, C. S. & Hakim, A. M. 2009. Living beyond our physiological means: small vessel disease of the brain is an expression of a systemic failure in arteriolar function: a unifying hypothesis. *Stroke*, 40, e322-30.
- Truebestein, L., Tennstaedt, A., Mönig, T., Krojer, T., Canellas, F., Kaiser, M., . . . Ehrmann, M. 2011. Substrate-induced remodeling of the active site regulates human HTRA1 activity. *Nat Struct Mol Biol*, 18, 386-8.
- U.S. Food & Drug Administration. 2017. *FDA approves novel gene therapy to treat patients with a rare form of inherited vision loss* [Online]. Available: https://www.fda.gov/news-events/press-announcements/fda-approves-novel-gene-therapy-treat-patients-rare-form-inherited-vision-loss?utm_campaign=12192017_PR_FDA%20approves%20first%20gene%20therapy%20treatment&utm_medium=email&utm_source=Eloqua [Accessed April 22, 2021].
- U.S. Food & Drug Administration. 2019. *FDA approves innovative gene therapy to treat pediatric patients with spinal muscular atrophy, a rare disease and leading genetic cause of infant mortality* [Online]. Available: <https://www.fda.gov/news-events/press-announcements/fda-approves-innovative-gene-therapy-treat-pediatric-patients-spinal-muscular-atrophy-rare-disease> [Accessed April 22, 2021].

- Uemura, M., Nozaki, H., Kato, T., Koyama, A., Sakai, N., Ando, S., . . . Onodera, O. 2020. HTRA1-Related Cerebral Small Vessel Disease: A Review of the Literature. *Front Neurol*, 11, 545.
- Uemura, M., Nozaki, H., Koyama, A., Sakai, N., Ando, S., Kanazawa, M., . . . Onodera, O. 2019. HTRA1 Mutations Identified in Symptomatic Carriers Have the Property of Interfering the Trimer-Dependent Activation Cascade. *Front Neurol*, 10, 693.
- Vanlandewijck, M., He, L., Mäe, M. A., Andrae, J., Ando, K., Del Gaudio, F., . . . Betsholtz, C. 2018. A molecular atlas of cell types and zonation in the brain vasculature. *Nature*, 554, 475-480.
- Verdura, E., Hervé, D., Scharrer, E., Amador Mdel, M., Guyant-Maréchal, L., Philippi, A., . . . Tournier-Lasserre, E. 2015. Heterozygous HTRA1 mutations are associated with autosomal dominant cerebral small vessel disease. *Brain*, 138, 2347-58.
- Vierkotten, S., Muether, P. S., & Fauser, S. 2011. Overexpression of HTRA1 leads to ultrastructural changes in the elastic layer of Bruch's membrane via cleavage of extracellular matrix components. *PLoS One*, 6, e22959.
- Wang, X. L., Li, C. F., Guo, H. W., & Cao, B. Z. 2012. A novel mutation in the HTRA1 gene identified in Chinese CARASIL pedigree. *CNS Neurosci Ther*, 18, 867-9.
- Wardlaw, J. M., Smith, C., & Dichgans, M. 2013a. Mechanisms of sporadic cerebral small vessel disease: insights from neuroimaging. *Lancet Neurol*, 12, 483-97.
- Wardlaw, J. M., Smith, C., & Dichgans, M. 2019. Small vessel disease: mechanisms and clinical implications. *Lancet Neurol*, 18, 684-696.
- Wardlaw, J. M., Smith, E. E., Biessels, G. J., Cordonnier, C., Fazekas, F., Frayne, R., . . . Dichgans, M. 2013b. Neuroimaging standards for research into small vessel disease and its contribution to ageing and neurodegeneration. *Lancet Neurol*, 12, 822-38.
- Yanagawa, S., Ito, N., Arima, K., & Ikeda, S. 2002. Cerebral autosomal recessive arteriopathy with subcortical infarcts and leukoencephalopathy. *Neurology*, 58, 817-20.
- Yu, Z., Cao, S., Wu, A., Yue, H., Zhang, C., Wang, J., . . . Wu, J. 2020. Genetically Confirmed CARASIL: Case Report with Novel HTRA1 Mutation and Literature Review. *World Neurosurg*, 143, 121-128.
- Zellner, A., Scharrer, E., Arzberger, T., Oka, C., Domenga-Denier, V., Joutel, A., . . . Haffner, C. 2018. CADASIL brain vessels show a HTRA1 loss-of-function profile. *Acta Neuropathol*, 136, 111-125.
- Zhuo, Z. L., Cong, L., Zhang, J., & Zhao, X. T. 2020. A novel heterozygous HTRA1 mutation is associated with autosomal dominant hereditary cerebral small vessel disease. *Mol Genet Genomic Med*, 8, e1111.
- Ziaei, A., Xu, X., Dehghani, L., Bonnard, C., Zellner, A., Jin Ng, A. Y., . . . Pouladi, M. A. 2019. Novel mutation in HTRA1 in a family with diffuse white matter lesions and inflammatory features. *Neurol Genet*, 5, e345.

DANKSAGUNG/ACKNOWLEDGEMENTS

An dieser Stelle möchte ich mich bei allen Menschen bedanken, die zum Gelingen dieser Arbeit beigetragen haben:

Zunächst bei meinem Doktorvater, Herrn Prof. Dr. Martin Dichgans für die Möglichkeit, an diesem spannenden Projekt zu arbeiten und die exzellente Betreuung. Zudem für die Bereitstellung eines großartigen Arbeits- und Forschungsumfelds am Institut für Schlaganfall- und Demenzforschung München, wo ich neurowissenschaftliche Forschung auf höchstem Niveau kennenlernen durfte. Herzlichen Dank außerdem für das Mentoring und die Unterstützung bei meinem Berufseinstieg.

Then, of course, my supervisor Dr. Nathalie Beaufort, who I cannot thank enough for her endless support and help not only in the lab but also during the writing process. Thank you for teaching me various experimental techniques and methods as well as scientific thinking and accuracy. Your passion for science and research, and your scientific knowledge have been truly inspiring. Merci beaucoup!

Next, the whole DichgansLab, especially the SVD group, Dr. Katalin Todorov-Völgyi, Dr. Christof Haffner, and Dr. Andy Zellner, who I had the chance to discuss my results with and who always provided very valuable scientific input and advice. A special thanks to Dr. Yaw Asare for helping with the virus injections.

Thank you, Dr. Farida Hellal, for the excellent introduction to confocal microscopy and image acquisition.

Vielen Dank an Melanie Schneider, Natalie Ziesch und Barbara Lindner für die technische und organisatorische Unterstützung während meiner Zeit am ISD, für die Einweisung in einige Methoden und nicht zuletzt für die angenehme Arbeitsatmosphäre.

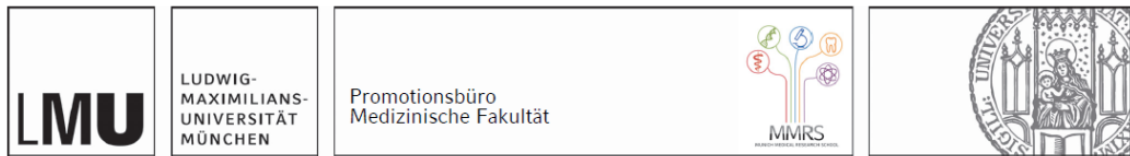
Specially, I want to thank Kyra Thomas, Rebecca Sadler, and Tom Campbell-James who had been great lab (and coffee break) partners.

Dank gilt meinem Onkel Alex Gerhard für das Korrekturlesen der Arbeit und wertvollen Input.

Danke Arne für deine Liebe und deinen Rückhalt.

Zuletzt möchte ich mich bei meinen Eltern für die bedingungslose Unterstützung während meines gesamten Medizinstudiums und vor allem während meiner Promotionsphase bedanken. Ohne euch hätte ich das nicht geschafft.

AFFIDAVIT



Eidesstattliche Versicherung

Gerhard, Ameli

Name, Vorname

Ich erkläre hiermit an Eides statt, dass ich die vorliegende Dissertation mit dem Titel:

ANALYSIS OF THE BRAIN VASCULATURE IN A NOVEL MOUSE MODEL OF HTRA1-RELATED CEREBRAL SMALL VESSEL DISEASE

selbständig verfasst, mich außer der angegebenen keiner weiteren Hilfsmittel bedient und alle Erkenntnisse, die aus dem Schrifttum ganz oder annähernd übernommen sind, als solche kenntlich gemacht und nach ihrer Herkunft unter Bezeichnung der Fundstelle einzeln nachgewiesen habe.

Ich erkläre des Weiteren, dass die hier vorgelegte Dissertation nicht in gleicher oder in ähnlicher Form bei einer anderen Stelle zur Erlangung eines akademischen Grades eingereicht wurde.

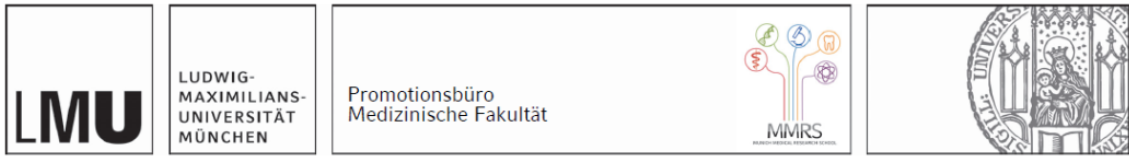
Berlin, 10.10.2022

Ort, Datum

Ameli Gerhard

Unterschrift Doktorandin bzw. Doktorand

CONGRUENCY DECLARATION



Erklärung zur Übereinstimmung der gebundenen Ausgabe der Dissertation mit der elektronischen Fassung

Gerhard, Ameli

Name, Vorname

Straße, Hausnummer

PLZ, Ort

Hiermit erkläre ich, dass die elektronische Version der eingereichten Dissertation mit dem Titel

ANALYSIS OF THE BRAIN VASCULATURE IN A NOVEL MOUSE MODEL OF HTRA1-RELATED CEREBRAL SMALL VESSEL DISEASE

in Inhalt und Formatierung mit den gedruckten und gebundenen Exemplaren übereinstimmt.

Berlin, 10.10.2022

Ort, Datum

Ameli Gerhard

Unterschrift Doktorandin bzw. Doktorand

LIST OF PUBLICATIONS

- Rohr, S. O., **Gerhard, A.**, Schmidt, F., Eder, J., Salvermoser, L., Dimitriadis, K., & Fischer, M. R. 2021. Thinking outside the box: students positive about visionary elective curricula in medical school. *GMS J Med Educ*, 38, Doc119.
- Gerhard, A.**, Prüß, H., & Franke, C. 2022. [Manifestations of the central nervous system after COVID-19]. *Nervenarzt*, 93, 769-778.